Magnetic Domain Walls for On-Chip Transport and Detection of Superparamagnetic Beads

ARCHIVES
MASSACHUSETTS INSTITUTE OF TECHNOLOGY
JUN 10 2014
LIBRARIES

by

Elizabeth Ashera Rapoport

B.A., Cornell University (2008)

Submitted to the Department of Materials Science and Engineering
in partial fulfillment of the requirements for the degree of

Doctor of Philosophy in Materials Science and Engineering

at the

MASSACHUSETTS INSTITUTE OF TECHNOLOGY

June 2014

© Massachusetts Institute of Technology 2014. All rights reserved.

Signature redacted

Author.....
Department of Materials Science and Engineering
May 2, 2014

Signature redacted

Certified by.....
Geoffrey S. D. Beach
Class of '58 Associate Professor of Materials Science and Engineering
Thesis Supervisor

Signature redacted

Accepted by.....
Gerbrand Ceder
Chairman, Departmental Committee on Graduate Students

Magnetic Domain Walls for On-Chip Transport and Detection of Superparamagnetic Beads

by

Elizabeth Rapoport

Submitted to the Department of Materials Science and Engineering
on May 2, 2014, in partial fulfillment of the
requirements for the degree of
Doctor of Philosophy in Materials Science and Engineering

Abstract

Surface-functionalized superparamagnetic (SPM) microbeads are of great interest in biomedical research and diagnostic device engineering for tagging, manipulating, and detecting chemical and biological species in a fluid environment. At the same time, lab-on-chip technologies have grown popular due to their many advantages, including small sample volume requirements, sensitivity, portability, and speed. As such, there has been a steady progression in the advancement of magnetic technologies for bead manipulation in chip-based devices. Given the non-volatility and fast speeds of magnetic domain walls (DWs), their study has been largely driven by their application to information technology. In this work, the use of magnetic DWs for superparamagnetic bead capture and manipulation was investigated and extended. The interaction and dynamics between SPM beads and DWs is described and thoroughly characterized, and it is demonstrated that, owing to their highly localized stray fields, DWs in magnetic tracks can be used to shuttle individual SPM microbeads and magnetically tagged entities across the surface of a chip. Indeed, fast transport around prototype ring structures and long distance translation along curvilinear backbones is demonstrated. Moreover, it is shown that the bead-DW interaction can be further exploited to achieve programmable manipulation of a bead at a junction in a branched curvilinear structure, enabling bead sorting and the design of complex bead routing networks. A method for DW-based SPM bead detection in these same structures is proposed and discrimination amongst commercial bead populations based on magneto-mechanical resonance is demonstrated. Thus, a DW-based technique is demonstrated that achieves a complete set of essential SPM bead handling capabilities, including capture, transport, identification, and release, required for an integrated magnetic lab-on-chip platform.

Thesis supervisor: Geoffrey S. D. Beach
Title: Class of '58 Associate Professor of Materials Science and Engineering

Acknowledgements

Of all parts of this thesis, I was most excited to write this section, in which I have the opportunity to formally thank all the people who have been there for me throughout my graduate school journey. For it is indeed a journey, and one I will forever cherish. But as anyone who has gone through a Ph.D. program can probably attest to, it is not for the faint of heart. Intellectually, of course it is a challenge. Classes are demanding, and the path towards novel scientific and engineering discovery is long and winding. Because of, and beyond the academic challenges, the graduate experience is a test of emotional strength. From both the extrinsic and intrinsic pressures to succeed (especially in a place like MIT), to the need to balance work and life, to the management of relationships, the graduate experience can certainly be emotionally charged. It is for all these reasons that I wholeheartedly thank the following people, without whom I could not have succeeded. The list is long, but there are few times in life when one gets the opportunity to immortalize their gratitude in text.

Firstly, I'd like to thank my advisor, Professor Geoffrey Beach. To anyone who asks about the graduate school experience, or who comes to our lab looking to join our group, I always say the same thing. Every topic is going to sound exciting, but at the heart of it, research is research. What will make or break your experience are your advisor and group. Choose someone you think you can work with for the next 5 years. I am thankful that I followed my own advice. Geoff, you are an advisor in every sense. You guide without force. You inspire without pretense. You listen without condescension. You ask a lot but also give a lot. Your biggest fault as an advisor is that you are too excited about what you do. So, thank you Geoff, for supporting me, pushing me, working with me, listening to me, and teaching me. I only hope that I have contributed to your first years at MIT as much as you did to mine.

I'd also like to thank the other members of my thesis committee, Professor Caroline Ross and Professor Alfredo Alexander-Katz. From my first year to my last, I have had the privilege to learn from you both in and out of the classroom. Your classes have been some of my favorites, and your availability and guidance beyond the lecture hall have been greatly appreciated. Thank you so much for your time, energy, insights, suggestions, and visible enthusiasm for what you do. To Professor Alexander-Katz in particular, thank you for allowing me to use your computers for simulations, an integral part of this thesis.

To my whole family, thank you. No one has been as invested, if not more, in my experience as you. You are the reason for any of my successes. For every woe or challenge I face, you take it on yourself and experience it at least ten times over. You are my foundation. I could never properly thank you for all the energy and emotion you have given and continue to give me, but I hope you know it is overwhelmingly appreciated. You push me, and I don't resent it. You support me, and I don't feel coddled. You poke fun at me, and I laugh. You tell me the truth, and I accept it. To my parents especially, I know living close by has been both a blessing and a curse. Thank you for all the late night visits to help me or calm me down when I was stressed. To Mash, thank you for your unwavering confidence in me and patience when I am difficult. I am so lucky to be part of the crazy that is my family.

For the following people I have only the utmost respect and gratitude. Their technical knowledge and willingness to assist is unparalleled. Moreover, they're just fantastic people to be around. For all their help with the macroscopic parts of my experiments, I'd like to acknowledge David Bono, Mike Tarkanian, Chris Di Perna, Ike Feitler, Franklin Hobbs, and

Matt Humbert. To David, thank you for your generous contribution, both material and intellectual, to my experimental set ups. Your talent is truly enormous, and if I ever know half as much as you, I will consider it a success. Thank you for your company and time, your energy and patience, your good humor and unique perspective. This thesis would be a shadow of what it is without you. To Mike, thank you for teaching me how to machine. Thank you for helping me build my magnet, the workhorse of all my experiments. Thank you for all your counsel and good advice when I was considering next steps after MIT. But most importantly, thank you for your friendship, MADMEC, and your nurturing my joy to create and work with my hands. Chris and Franklin, although our overlap at MIT has been relatively short, it feels like we have been friends forever. Thank you for being so approachable. Thank you for being so willing to help. And thank you for being so wicked awesome to be around. Ike, thank you for all the time spent helping me with the laser cutter and water jet. I know handling the demand on those tools can be stressful, and I appreciate your time and patience. Matt (Steve), thank you for your help during MADMEC and other times. And thank you for always being a good time.

In terms of all the small parts, my experiments wouldn't be anything without the use of MIT's NanoStructures Lab and Electron Beam Lithography facility, headed by Prof. Karl Berggren and Prof. Hank Smith, and run by Jim Daley and Mark Mondol, respectively. Jim, thank you for all your assistance in the cleanroom, whether it be with the SEM or a fabrication process, or the evaporation of films. And thank you also for being the single person who seems to pass no judgment, ever. In a place that feels like constant competition, it can be daunting to ask a question, but you have always made it feel ok. That has been worth more than you can imagine. Mark, thank you for all your patience and advice during my many hours in the Raith room over the years. I can't imagine it's easy to be on constant call, and yet you were always willing to help or answer a question.

For all the administrative work they do, I'd like to thank Angelita Mireles, Elissa Haverty, Rachel Kemper, and Nathaniel Berndt. You have all helped me throughout my time MIT, and whether it was with booking a room, setting up an event, or by reminding me of a deadline, it always was done with a smile. Your work makes the department run, and I want to thank you for all you do.

Thank you to my funding sources, the MIT Deshpande Center and the MIT Center for Materials Science and Engineering. My research literally would not have been possible without your contribution.

I don't think I have ever spent more time in one place than in the basement of building 4 at MIT. Although having the one desk next to the one window helped, it was all the members of the Beach group, past and present, who made my time at MIT so enjoyable. Satoru, thank you for being an amazing co-founding Beach group member. From assembling the sputtering system those early days, to watching terrible movies, to eating meat masterpieces, we have been through a lot together. And throughout, your determination, intelligence, and endurance have been constant source of inspiration, in and out of the lab. Uwe, thank you for being one of my best friends. I have always given you a hard time, saying you wouldn't be able to survive in the lab without me, but we both know it goes both ways. No one has gone through as much with me here as you. At times it was painful and at all times it was loud, but all in all it was a sincere pleasure. Thank you for help in the lab, company on walks home, insistence on things like soda stream and outside eating, and out of lab jello and steel related pursuits. It truly wouldn't have been the same without you. Shwoo, you are one of the best people I know. Your presence brings a calm to the lab that was sorely needed. Thank you for all the times you listened to me, with sincerity and

without judgment. Thank you for your kindness. And thank you for being just so damn cool. Parnika and Minae, thank you for being awesome female lab mates. Being the only girl grad student in the lab for many years, I was nervous how your addition would play out. But you guys, or should I say gals, are great. I have loved bonding with both of you over things from lab to clothing. Minae, I couldn't imagine a better person to hand off my setup to. And Parnika, learning about your culture and having you in our office has been a treat. Lucas, though you haven't been in the lab long, we have already become fast friends. Thank you for your sincere words, advice about work matters, and good times. You really added to my last year at MIT, so thank you. Max, thank you for being more than my 2-D image of you. Your brain works in wacky and mysterious ways, and it's a delight to observe. To steal your expression for something else and use it on you--it's like you're simultaneously wearing a dinner suit, business jacket, and pair of pajamas. AJ, thank you for being so positive and good-natured. Thank you for having a hilarious appetite. And yeah yeah yeah yeah, no no no no no. Helia, thank you for being brutally honest and sassy. You don't sugar coat anything and you tell it like it is, and I love it. Thank you so much for your friendship over the years. Dan Montana, from a technical perspective, thank you for helping me collect all those resonance measurements. I know it was tedious work, and I appreciate the assistance. From a personal perspective, thank you for assuring me that you-know-who wasn't mean and for adding so much to my first years in the lab. Nicholas! Somehow, even though our British and American sensibilities are completely opposite, we get along so well. I am so happy you came to our lab and I got the chance to get to know you. Thank you for coffee breaks, your British ways and bright colored socks, and for hosting me in England. Elie, I don't know anyone else who looks at the world so positively, and it's infectious. Thank you so much for sailing, bike rides, and your bright spirit. Also, c'est un caffouage! Tristan, you strike an amazing balance of nonchalance and industriousness. Thank you for being a great example of someone who worked hard and played hard. Jonathan, thank you for actually embodying so many German stereotypes in such a great way. My favorite memory of you will always be your response to my question of how you could leave work so early: "I just work more efficiently than you." Thank you for all the good times and inviting me into your home in Germany. Greg, thank you for being so, well, Greg.

Although sometimes it didn't seem so, I also had life outside of the lab. I'd like to thank some of the MIT people who were part of that. Ahmed, in my mind you're essentially one of the Beach group. You are one of the most selfless and well-meaning people I know. You are also one of the most ridiculous. Thank you for being all those things. I cherish our friendship and all times—stressful and light-hearted, MADMEC and otherwise—spent together. Charles, thank you for helping me translate my code into C and getting me set up on your group's cluster. Thank you also for all the afternoon office visits. They were a welcome break from the stresses of the day. Heather and Sophie, thank you so much for all the tea times, the baked goods, and the outdoor picnicking. These were honestly a delight. Heather, I am so glad we came into MIT together. You are a true friend. Not the end. Sophie, thank you for continued teas after graduation and your caring nature. John, thank you for forcing us to become friends. I have loved having a yoga buddy. Alexis, I can talk like zis or I can talk like zis. Although we don't see each other as often as I'd like, I have always felt a warm familiarity with you, from the moment we met, as if we had known each other for ages. Thank you for that and for having my back. Helmut, thank you for being such a good friend. Not many people would send birthday presents across the globe every year. Not many people would go to the lengths you did to host two American tourists. But you did, and I really treasure that. Reid, thank you for helping me with your group's cluster

once Charles had gone. I know you were busy, and I really appreciate the time you took to help me with my work. Nicolas, thank you for all the good times at conferences and MIT and for being both smart and modest. Lara, Jean Anne, and Saima, thank you for being fantastic hotel roommates. Jordan, thank you for all the smorgasbord of parties with their smorgasbord of food. Meg, thank you for all the crafting. Forrest, thank you for showing me your lab and morning bump-ins at flour. To the students I had the privilege to TA, thank you for making my teaching experience so enjoyable. To the Demkowicz group, thank you for enduring the noise level over the years.

Finally, I'd like to thank friends outside of MIT, some of whom I have known forever and are essentially family. Rimma, thank you for everything. You are an amazing best friend. Your excitement and support for others is with your whole self. You don't half-ass anything. Thank you for your intensity, your joy, your utter ridiculousness, your friendship. Thank you for skype and letters, birthdays and coffee shops. Even though you weren't actually here, MIT would not have been nearly as fun without you. Victor, you are one of my best friends. Whether we talk everyday or once in a month, I know you are always there for me. You are clever and quick-witted and I always laugh with you. Thank you for being part of my life for so long. Mike, thank you for just getting me. Thank you for all our time spent together, and for your understanding and kindness. Your ability to make change for yourself is amazing. Thank you for goats, Gordon Ramsay, and apple store visits. Masha, I am in awe of your ability to be so awkward yet simultaneously so good with people. You make things happen and it's truly impressive. And I always have the best time with you. I am so happy our friendship has stood the test of time. Maya, I have known you the longest out of anyone, and I love that we are still friends, despite our geographic separation. I immensely respect your intelligence, ability to so calmly tackle anything, and see the humor in most things. Tanya, thank you for how much you care and your dedication to your friends. It is unparalleled. Leo, thank you for being utterly hilarious. I have so much respect for what you're doing. Bruno, thank you for your caustic humor and sincere friendship. Molly, thank you for being my favorite vegan friend, and not only because you're the only one. UPenn would have been sad without you. Misha Pivovarov, thank you for being so helpful, both with advice and connections, with regards to jobs after graduation. Vera, thank you for always, always being there for me. Mrs. Rifkin, thank you for all the math, the camp, and the friendships I made because of them.

To everyone, thank you.

Contents

Abstract **3**

Acknowledgements **5**

List of Figures **13**

List of Frequently Used Abbreviations **15**

List of Frequently Used Symbols **17**

Chapter 1 Introduction **19**

1.1 Motivation 19

1.2 Thesis outline 22

Chapter 2 Background **23**

2.1 Magnetic energy terms 23

2.2 Magnetic domain walls 24

2.2.1 Structure of domain walls in magnetic thin films 25

2.2.2 Field-induced domain wall motion 28

2.2.3 Domain wall logic 29

2.3 Superparamagnetic beads 30

2.3.1 Superparamagnetism 31

2.3.2 Magnetic force on bead in a magnetic field 33

2.3.3 Drag force on beads in viscous medium 34

2.3.4 Other forces 35

2.4 Magnetoresistance 35

Chapter 3 Simulation and experimental methods **39**

3.1 Simulation of bead-domain wall interaction 39

3.2 Sample fabrication 42

3.2.1 Shadow mask lithography 43

3.2.2 Electron beam and optical lithography 43

3.2.3 Sputter and evaporative deposition 45

3.2.4 Liftoff 45
3.3 Sample characterization and data acquisition 45
3.3.1 Scanning electron beam microscope 46
3.3.2 Superparamagnetic beads 46
3.3.3 Sample preparation 46
3.3.4 Custom vector electromagnet 47
3.3.5 Contact plate and switchbox for electrical characterization 52
3.3.6 Magneto-optic Kerr effect system 53
3.3.7 Optical detection with LabVIEW 56
Chapter 4 Numerical Studies of Interactions in the Bead-domain wall system ... 57
4.1 Magnetostatic bead-domain-wall interaction 58
4.2 Variables for bead transport 62
Chapter 5 Domain-wall-driven bead transport dynamics 65
5.1 Continuous bead transport by field-driven DWs 67
5.2 Slow bead motion by domain wall knocking 70
5.3 Maximum bead velocity via continuous transport 77
5.4 Discussion 83
Chapter 6 Programmable bead motion along a magnetic circuit 85
6.1 Bead motion along a curvilinear backbone 85
6.2 Junction geometries 86
6.3 Domain wall motion through a curvilinear junction 88
6.4 Bead motion through a curvilinear junction 90
6.4.1 Asymmetric bead interaction with domain walls of opposite configuration under vertical field 90
6.4.2 Sorting a two-bead population 96
6.5 Discussion 99
Chapter 7 Magneto-mechanical resonance detection 101
7.1 Magneto-mechanical resonance theory 101

7.2 Optical characterization of resonant dynamics 105
7.3 Electrical integration for magnetoresistive sensing 109
7.4 Discussion 115
Chapter 8 Summary and outlook 117
8.1 Summary 117
8.2 Future work 118
8.2.1 Integration and biological testing 118
8.2.2 Organization of matter 119
8.2.3 Tagless transport of nonmagnetic species 120
Bibliography 121

List of Figures

FIG. 2-1 Magnetostatics and the formation of magnetic domains 25
FIG. 2-2 Bloch and Néel walls 26
FIG. 2-3 Spin structure across a domain wall 26
FIG. 2-4 Transverse and vortex walls 27
FIG. 2-5 Domain wall velocity under applied feld 28
FIG. 2-6 Domain wall motion in non-linear elements 30
FIG. 2-7 Superparamagnetic microbead 31
FIG. 2-8 Superparamagnetism 33
FIG. 2-9 Magnetoresistance and magnetoresistive devices 37
FIG. 2-10 Magetorsisiance versus domain wall position 38
FIG. 3-1 Domain wall initialization for micromagnetic calculations 41
FIG. 3-2 Example magnetostatic potential energy well 42
FIG. 3-3 Sample preparation with suspension of magnetic beads 47
FIG. 3-4 Vector electromagnet schematics 47
FIG. 3-5 Vector electromagnet field vector 48
FIG. 3-6 Vector electromagnet assembly 49
FIG. 3-7 Vector electromagnet field amplitude homogeneity 50
FIG. 3-8 Vector electromagnet field angle homogeneity 51
FIG. 3-9 Contact plate for electrical measurements 53
FIG. 3-10 Magneto-optic Kerr effect (MOKE) 55
FIG. 3-11 Optical detection with LabVIEW 56
FIG. 4-1 Bead-DW system 58
FIG. 4-2 DW topography and bead-DW energetics 60
FIG. 4-3 Binding forces and maximum velocities 63
FIG. 4-4 Bead-DW energy and binding in vertical field 64
FIG. 5-1 Characteristic bead velocity versus DW velocity (VV) curve 66
FIG. 5-2 Observation of synchronous bead-DW motion 68
FIG. 5-3 Observation of bead motion in the knocking regime 70
FIG. 5-4 Model for bead-DW interaction in high DW velocity regime 72
FIG. 5-5 Simulated and experimental bead trajectories in the high DW velocity regime 74

FIG. 5-6 Video analysis of bead trajectory 75
FIG. 5-7 Bead displacement per DW in the high DW velocity regime 76
FIG. 5-8 Bead velocity versus DW velocity as function of bead size 78
FIG. 5-9 Bead velocity versus DW velocity as function of vertical field 79
FIG. 5-10 Bead velocity versus DW velocity as function of track material 80
FIG. 5-11 Maximum velocity statistics as function of track material 81
FIG. 5-12 Maximum bead velocity versus drive field amplitude 82
FIG. 6-1 Bead transport along curvilinear track 86
FIG. 6-2 Junction geometries 87
FIG. 6-3 Domain wall initialization in a junction for micromagnetic calculations 88
FIG. 6-4 DW motion through a field-controlled junction 89
FIG. 6-5 Asymmetric interaction under vertical field 91
FIG. 6-6 Junction energy landscape under rotating in-plane field and dc vertical field 92
FIG. 6-7 Programmed bead motion through a junction 94
FIG. 6-8 Probability curves for bead motion at a junction 95
FIG. 6-9 Junction energy landscapes as a function of bead 96
FIG. 6-10 Threshold vertical switch-field as function of bead 97
FIG. 6-11 Sorting a two bead population 98
FIG. 7-1 Cross sections of magnetostatic potential energy surfaces 102
FIG. 7-2 Model of resonance dynamics for the bead- DW system 103
FIG. 7-3 Optical characterization of magneto-mechanical resonance 106
FIG. 7-4 Resonance curves and statistics for two different sized beads 108
FIG. 7-5 Test pseudo-spin-valve structure 110
FIG. 7-6 Pseudo-spin-valve track for magnetoresistive sensing 112
FIG. 7-7 Electrical measurement of DW magneto-mechanical resonance 113
FIG. 7-8 Resonance curve from magnetoresistance measurement 114
FIG. 8-1 Sandwich assay schemes for antigen capture and tagging 119

List of Frequently Used Abbreviations

CCW	Counterclockwise
CoFe	Cobalt iron ($Co_{50}Fe_{50}$)
COMPEL	COMPEL COOH modified (UMC3N/11086) bead (5.8 μm diameter)
CW	Clockwise
DW	Domain wall
FM	Ferromagnetic
fps	Frames per second
H-H	Head-to-head
M-270	Dynabeads M-270 Carboxylic Acid bead (2.8 μm diameter)
MOKE	Magneto-optic Kerr effect
MyOne	Dynabeads MyOne Carboxylic Acid bead (1.0 μm diameter)
NiFe	Permalloy ($Ni_{80}Fe_{20}$)
NM	Nonmagnetic
OOMMF	Object-oriented micromagnetic framework
PDMS	Polydimethylsiloxane
PMMA	Poly(methyl methacralate)
ROI	Region of interest
rpm	Rotations per minute
SPM	Superparamagnetic
T-T	Tail-to-tail
VV	Bead velocity versus domain wall velocity

List of Frequently Used Symbols

α	Damping coefficient
A	Exchange stiffness
B	Magnetic induction
D	Bead diameter
f_0	Resonance frequency
f_{bead}	Bead frequency
f_{drive}	Drive field frequency
f_{max}	Maximum bead frequency
F_{bind}	Binding force
F_{drag}	Drag force
γ	Gyromagnetic ratio
η	Viscosity
H	Magnetic field
H_z	Vertical magnetic field
K_u	Uniaxial anisotropy constant
μ_0	Permeability of free space
m	Magnetic moment
M	Magnetization
M_r	Remnant magnetization
M_s	Saturation magnetization
ξ	Near surface correction factor
R	Bead radius
R_{track}	Track diameter
U	Potential energy
v_{bead}	Bead velocity
v_{DW}	Domain wall velocity
v_{max}	Maximum bead velocity
χ	Magnetic susceptibility

Chapter 1

Introduction

In this chapter, we motivate the importance of exploring magnetic domain walls for on-chip manipulation of superparamagnetic beads. We then briefly outline the trajectory of this thesis.

1.1 Motivation

There has been considerable interest in the past couple of years to develop faster, cheaper, higher throughput, more sensitive, and smaller devices for medical diagnostics and biomedical research. The so called "point-of-care" or "lab-on-chip" technologies are touted for their possibility of bringing diagnostics closer to the patient, reducing sample volume requirements, and scaling down the size of devices while simultaneously increasing their functionality.

The facile, remote, and controlled transport of biological species across the surface of a chip is critical for the development of lab-on-chip technologies. Owing to the wealth of bead options, from surface chemistry to size to mode of actuation, surface-functionalized micro- or nanometer-sized beads have become a popular means of controlling, transporting, and manipulating biological species in a liquid environment. Bead-based devices represent the future of biomedical research and patient care, and as such there have been many approaches to achieving bead control. Example systems include those that exploit acoustic[1-5], electrokinetic[6-10], optical[1,3-5,11-78], hydrodynamic[6,30], and magnetic forces[3,11-65,67-79].

Magnetic systems are attractive for a variety of reasons. Such systems require neither channels, nor in many cases, electrical connections, which introduce unnecessary complexity[30]. Magnetic beads can be manipulated by magnetic fields, representing an extra degree of freedom over nonmagnetic beads[12-14,18,79] and allowing "action at a distance"[13]. Unlike fluorescence, the basis for optical systems such as fluorescence activated cell sorting (FACS)[80], magnetization cannot be quenched. Magnetic field gradients, and thus forces, can be localized, even to the level of single beads[26,31-40,42,44,45,68,69,75,81-83]. Biological samples have little to no magnetic susceptibility, allowing for high selectivity due to the difference in

susceptibility between magnetic beads and nonmagnetic samples[13]. In addition, magnetic fields do not interfere with biological processes, whereas electric fields can interfere with normal cellular functioning and even produce detrimental heating[75]. And unlike FACS, which is serial in nature[74], magnetic sorting can be run as a parallel process, offering the potential for very high throughput.

Over the past several years, there has been a steady progression in the advancement of magnetic technologies for superparamagnetic (SPM) bead manipulation. Microscale electromagnets[19-24] and arrays of soft magnetic microstructures[25-35] have previously been used to transport microbead ensembles[19,22,27,28,39,84] and even individual beads[26,35,40,43-45,68,69] across the surface of a chip. Yellen et al.[84,85] demonstrated the configurable arrangement of magnetic and nonmagnetic matter by programming magnetization patterns in discrete magnetic elements. Gunnarsson et al.[26] used magnetic elements arranged as magnetic tracks to move individual magnetic particles. However, these methods have limitations. Although permanent magnets can generate rather large fields, individual elements are not easily reconfigured. Fields generated by micro-current-carrying wires can be easily individually controlled, but they tend to be weaker than those generated by permanent magnets.

On the detection side, magnetoresistive sensors[86-92], which exhibit a perturbed response to applied excitation fields due to the presence of beads at the sensor surface[46-50,52-63,67,93,94], form the basis for most SPM bead sensing platforms. On-chip bead-based sensing of biomolecules in such devices, as e.g. the bead array counter (BARC)[48], usually relies on chemical functionalization of the sensor surface for preferential capture and immobilization of magnetic marker beads in the presence of a chemical target in the host fluid. This mode of sensing precludes subsequent transport of immobilized beads, and requires chemical decoration of the sensors, increasing fabrication complexity and limiting device versatility and generality. An alternate approach moves the active area from the chip surface to that of the SPM bead. Brownian relaxation biodetection[65-67,95-98] uses the beads themselves as the capture agent and thus does not require chemical immobilization of beads on the sensor surface. The Brownian relaxation frequency is directly related to the hydrodynamic radius of the beads, such that changes in the radius due to e.g. target binding at the bead surface manifest as a shift in the relaxation frequency. Dalslet et al.[67] and Donolato et al.[66] have recently demonstrated on-chip detection of beads suspended in a fluid above a

magnetoresistive sensor based on their Brownian relaxation. However, sensitivity at the level of individual microbeads has not yet been demonstrated using such a mechanism.

Magnetic domain walls (DWs) in patterned ferromagnetic tracks have become an increasingly promising option for overcoming the limitations of previous magnetic approaches. Recently it has been shown that the strong, localized stray field[41,99] from domain walls in submicrometer ferromagnetic tracks can trap individual SPM beads with forces up to hundreds of pN[36,38,42-45,69,81,100]. As DWs can be readily driven along a track by a magnetic field[101-107] or spin-polarized electric current, they can serve as mobile magnetic traps for single bead transport along a predefined path. Vieira et al.[36,42,108] demonstrated that DWs in zig-zag magnetic nanotracks can be used to capture and release SPM microbeads and magnetically tagged entities and shuttle them across the surface of a substrate. Donolato et al.[38,40] extended this work to show that not only could beads follow a travelling DW potential, but that they could precisely track it in a curved structure. It has also been shown that DWs can be used to sense the presence of individual beads[62-64,68,69]. Llandro et al.[62] demonstrated the detection of individual beads by measuring the effect of their stray field on DW-mediated magnetization switching in pseudo-spin-valves. Vavassori et al.[63] exploited the magnetic focusing action of DWs to position a bead near a DW trapped at a nanotrack corner, and then detect the bead's presence based on a small change in the DW depinning field.

In this thesis, for the first time, the dynamics of bead transport by field-driven DWs is carefully investigated and characterized. Whereas previous work has focused more on the sole realization of bead motion by patterned magnetic elements or DWs, we explore the dynamics of bead-DW interaction, gaining a deeper understanding of the fundamental forces at play. Equipped with this knowledge, we specially design magnetic tracks with which we are able to not only enhance the transport capabilities of DWs, but also show that the same mechanism that drives transport can be used for bead identification. Thus, through a deep understanding of the bead-DW system, we not only further demonstrate the power of magnetic DWs for on-chip bead manipulation, but also present an architecture by which the integrated transport and detection of beads becomes viable.

1.2 Thesis outline

Given the advantages of magnetic lab-on-chip technologies, it is our aim to develop a high throughput and integrated magnetic architecture capable of achieving all the tasks e.g. capture, transport, identification, sorting, and release, required for a true lab-on-chip platform. As such, in the chapters that follow, we show that the bead-DW system is a viable candidate for such an architecture, and present proof-of-concept results justifying this assertion. In Chapter 2, we lay the groundwork and begin with a discussion of the physical phenomenon later demonstrated to support an integrated magnetic lab-on-chip device. Chapter 3 then presents an overview of the simulation and experimental methods utilized in this thesis. With Chapter 4, we introduce the system of interest, i.e. that of the bead and DW, and investigate, via a combination of micromagnetic modeling and numerical methods, the viability of using this system to achieve bead transport by field-driven domain walls. Chapter 5 follows with experimental results that both corroborate the numerical predictions of the previous chapter, and explore the dynamics of bead transport beyond what was initially predicted. In Chapter 6 and Chapter 7, the capability of the bead-DW system to perform additional critical functions required for a lab-on-chip technology is investigated. In Chapter 6 we follow with an investigation of the programmability of beads along more complicated magnetic circuits, with applications for sorting and different subpopulation bead handling. Finally, in Chapter 7 the ability of the bead-DW system to detect and identify beads via their magneto-mechanical resonance is studied. We conclude in Chapter 8 with a summary of the demonstrated abilities, and an outlook for the future.

Chapter 2

Background

In this chapter we describe the physical phenomena relevant to developing an integrated magnetic lab-on-chip technology. First, the details of the foundational components, domain walls and superparamagnetic beads, are presented. We then follow with a discussion of magnetoresistance, which will become important as we begin building device elements in later chapters.

2.1 Magnetic energy terms

There are several magnetic energy terms, the minimization of the total of which dictates observed magnetic phenomena. These energies include exchange, magnetostatic, anisotropy, and Zeeman. Here we discuss the form and implications of each of these relevant terms.

Exchange energy is that energy that tends to keep adjacent magnetic moments aligned in parallel. Defined[109] as

$$E_{ex} = A(\frac{\partial\theta}{\partial x})^2, \tag{1}$$

it increases with increased angular divergence $\frac{\partial\theta}{\partial x}$ between neighbor spins with a proportionality dictated by the exchange stiffness A, and is responsible for the observation of ferromagnetism i.e. that a material retains its magnetization after removal of a magnetic field.

Magnetostatic energy results from the interaction between spins and dipolar demagnetizing fields, and arises mainly from having a discontinuity in the normal component of magnetization across an interface. It is an anisotropic energy that depends strongly on sample shape. It is defined[109] as:

$$E_{ms} = -\mu_0 M_s H_i \cos\theta \tag{2}$$

where M_s is the saturation magnetization of the material, and the internal field $H_i = H_{appl} + H_d$ is a function of both the externally applied field H_{appl} and the dipolar demagnatazing field H_d. As the angle θ between the magnetization and internal field

increases, the magnetostatic energy increases. Thus, the demagnetizing field contribution to the internal field, which acts to oppose the magnetization, increases magnetostatic energy.

It should be noted that the exchange and magnetostatic energies work in opposition, with the former favoring parallel spin alignment, and the latter favoring antiparallel alignment. The extent l over which one or the other energy dominates is characterized by the exchange length[110]

$$l_{ex} = \sqrt{\frac{2A}{\mu_0 M_S^2}}, \tag{3}$$

with $l < l_{ex}$ dominated by exchange interactions, and $l > l_{ex}$ dominated by magnetostatic interactions.

Anisotropy energy describes the preference for spins to lie along a certain crystallographic direction. In the simplest uniaxial case, this is given as

$$E_k = K_u \sin^2 \theta, \tag{4}$$

where θ is the angle between the spin and the preferred direction, and K_u is the uniaxial anisotropy constant.

Finally, the Zeeman energy

$$E_Z = -MB \cos \theta \tag{5}$$

describes the tendency of magnetization to align with a field, with this energy decreasing as the angle θ between the magnetization M and field B decreases.

With these energy terms in mind, we are now prepared to delve into the Section 2.2 discussion of DWs in magnetic materials.

2.2 Magnetic domain walls

In ferromagnetic samples of sufficient size, the material magnetization is not homogenous, but rather divided into various magnetic domains. The occurrence of magnetic domains, even in net magnetized samples, can be understood from an energetic perspective. Consider FIG. 2-1(a) below. The free magnetic pole density at the surface is relatively high, resulting in large magnetostatic energy. This energy can be reduced by the introduction of magnetic domains [FIG. 2-1(b)] i.e. regions of uniform magnetization in which the magnetization points in different directions, separated by magnetic domain walls. Although

these domain walls themselves have an associated energy cost, their presence is energetically favored in many magnetic systems. Furthermore, they produce large localized gradient stray fields[41,99] (Section 2.2.1), and can be propagated by application of a field[101,103-107,111] or current[112,113] (Section 2.2.2), making them promising candidates for bead manipulation. In the following sections, we describe the structure of domain walls and their field-induced motion, with attention to domain wall logic.

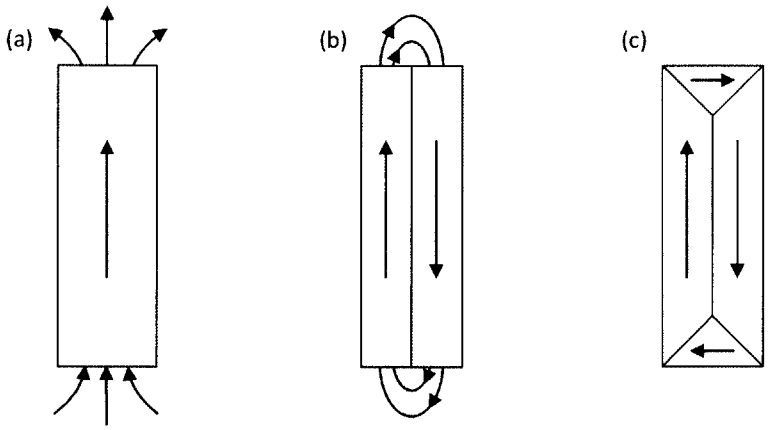

FIG. 2-1 Magnetostatics and the formation of magnetic domains

(a) The high magnetostatic energy of a single domain in a saturated magnetic material drives the formation of (b) multiple domains separated by a domain wall, raising the wall energy but lowering the magnetostatic energy. (c) Closure domains eliminate magnetostatic energy, but at the cost of higher wall, anisotropy, and strain energy. The final domain configuration is dictated by total energy minimization. (a-c) Adapted from O'Handley, R. C. *Modern magnetic materials: principles and applications.* (John Wiley & Sons, Inc., 2000).

2.2.1 Structure of domain walls in magnetic thin films

The introduction of a domain wall to magnetic material has a certain energy cost. If we consider the magnetic element in FIG. 2-2 and zoom in on the spins at the interface between the two regions of opposite magnetization, we might initially guess that the spins take on the configuration in the left oval. In this case, the spins lie along the preferred crystallographic direction and the anisotropy energy is minimized. However, we must also consider the exchange energy, which, owing to the two antiparallel spins at the interface, is very high. The total energy can be lowered if the spins instead take on a configuration as in the right oval. Here, although the anisotropy energy increases, the exchange energy decreases as the spins reverse direction over an extended distance. This second configuration of

gradual rotation lowers the total wall energy and is indeed what is observed in real materials. The wall thickness δ_{DW}, or the extent over which this transition takes place, is consequently that which minimizes the sum of exchange and anisotropy energies. For the $180°$ wall, δ_{DW} is defined[109] as

$$\delta_{DW} = \pi\sqrt{\frac{A}{K_u}}. \tag{6}$$

Over this distance, the spins rotate to about 27% of either the domain magnetization direction.

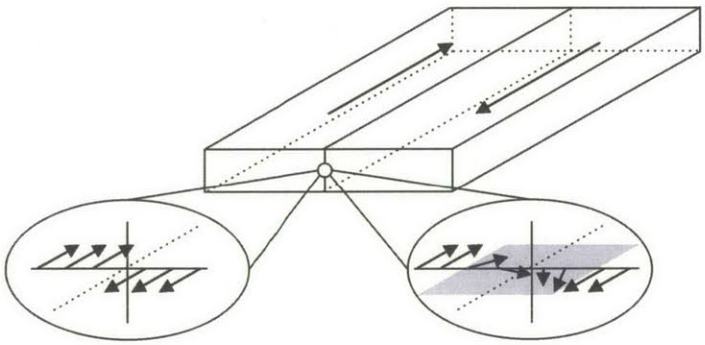

FIG. 2-2 Spin structure across a domain wall

Schematic of a magnetic material containing a domain wall and two possible spin configurations across the wall. (left) In the absence of exchange energy, this would be the preferred spin configuration, with anisotropy energy at its minimum. (right) Due to the presence of exchange energy, this represents the more realistic spin configuration across a domain wall, in which gradual magnetization rotation occurs across the span of several spins. Adapted from O'Handley, R. C. *Modern magnetic materials: principles and applications.* (John Wiley & Sons, Inc., 2000).

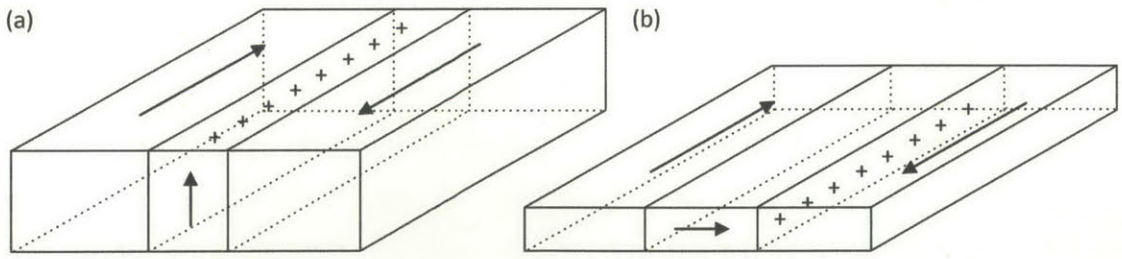

FIG. 2-3 Bloch and Néel walls

(a) Bloch wall with magnetization rotation out-of-plane and external charged surface and (b) Néel wall with magnetization rotation in-plane and internal charged surface. (a-b) Adapted from O'Handley, R. C. *Modern magnetic materials: principles and applications.* (John Wiley & Sons, Inc., 2000

Looking at FIG. 2-2 once more, we note that the direction of spin rotation through the wall could have instead rotated in the plane of the film. What we have not yet considered is the magnetostatic energy of the system. The DW of FIG. 2-2, known as a Bloch wall, is shown again in FIG. 2-3(a), with the net magnetization and surface charges indicated. There is a magnetostatic energy penalty to having these surface charges, and as the thickness of the film is decreased, the magnetostatic energy increases and favors rotation of magnetization in the plane, as in FIG. 2-3(b). This 180° rotation of spins in the plane constitutes a Néel wall, and is the favored configuration of domain walls in thin films.

As material dimensions are restricted further, now in width, the Néel wall is observed in one of two main configurations. In thin and narrow magnetic tracks where the shape anisotropy constrains the magnetization to lie in-plane along the long-axis of the track[101,106], the magnetization of neighbor domains is aligned either head-to-head (H-H) or tail-to-tail (T-T). The H-H or T-T Néel wall at the interface of these domains can be of either a transverse [FIG. 2-4(a)] or vortex [FIG. 2-4(b)] configuration, depending on the track geometry[113-115] [FIG. 2-4(c)]. From the representative schematics of the net magnetization across the wall and the micromagnetically generated (Section 3.1) wall simulations in FIG. 2-4(a-b), we note that the transverse wall is characterized by complete in-plane rotation of

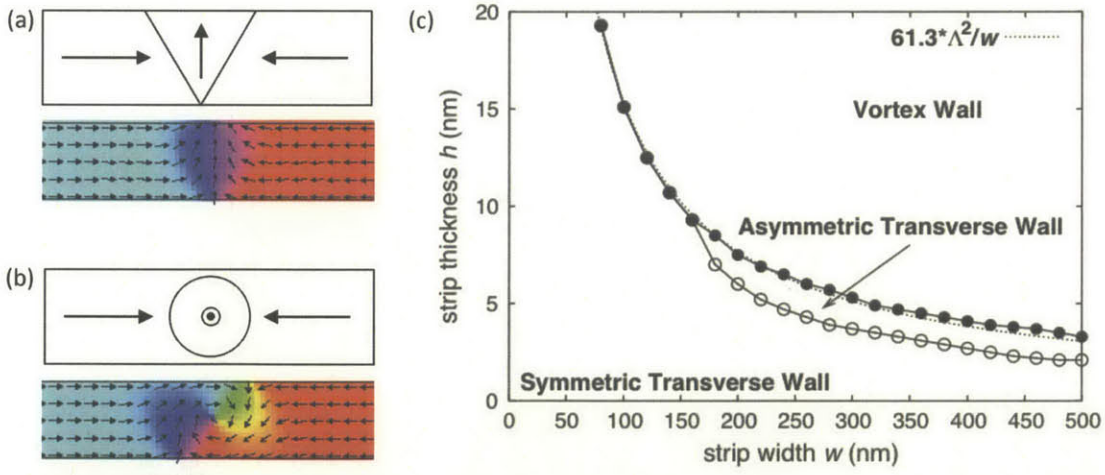

FIG. 2-4 Transverse and vortex walls

(a-b) (top) Schematic representation and (bottom) micromagnetically-generated spin configuration of a (a) transverse and (b) vortex wall. (c) Phase diagram defining the geometric conditions for which either a transverse or vortex wall is expected in a magnetic strip of thickness h and width w. Reprinted from Nakatani, Y., Thiaville, A. & Miltat, J. Head-to-head domain walls in soft nano-strips: a refined phase diagram. *J. Magn. Magn. Mater.* **290-291,** 750–753 (2005), with permission from Elsevier. Available at http://dx.doi.org/10.1016/j.jmmm.2004.11.355.

magnetization, whereas the magnetization of a vortex wall comes out of the plane. Analogous to the case of a Bloch versus Néel wall, it follows that transverse walls, which set up surface charges on the edge of the track, form preferentially in narrower, thinner tracks, whereas vortex walls, with net magnetization perpendicular to the film, form preferentially in thicker, wider ones. In either configuration, surface charges generate high gradient stray fields[41,99] in the vicinity of the wall that can be used to trap magnetic particles[35-38,40,42-45,68,69,81,100] (Section 4.1).

2.2.2 Field-induced domain wall motion

Magnetic domain walls are mobile entities that can be propagated through a magnetic film or patterned track by application of either a field[101,103-107,111] or current[112,113]. There has been much work[101,103-107,111-113,116,117] demonstrating and characterizing field-driven DW motion in ferromagnetic tracks. When an external field H_{ext} is applied along a magnetic track

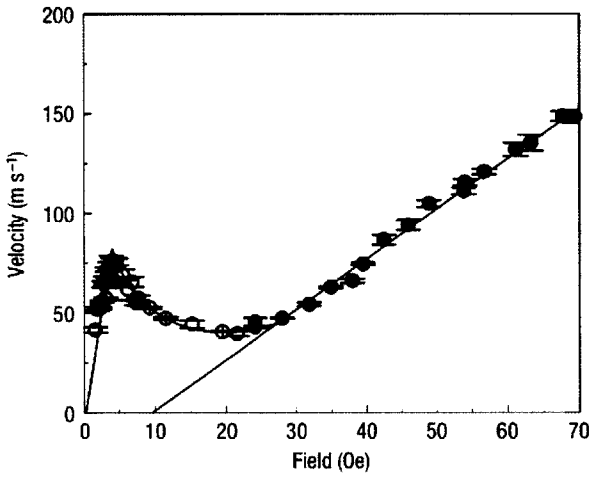

FIG. 2-5 Domain wall velocity under applied feld

Domain wall velocity in the Permalloy layer of a 600 nm wide, 20 μm long Ta(3 nm)/Permalloy(20 nm)/Ta(5 nm) trilayer track as a function of applied field amplitude. Two regimes corresponding to DW propagation by sliding and turbulent motion at low and high field, respectively, are observed. In either case, there is a linear relation between DW velocity and applied field that scales as the DW mobility. Adapted by permission from Macmillan Publishers Ltd: Beach, G. S. D., Nistor, C., Knutson, C., Tsoi, M. & Erskine, J. L. Dynamics of field-driven domain-wall propagation in ferromagnetic nanowires. *Nat. Mater.* **4,** 741–744 (2005). Available at http://dx.doi.org/10.1016/j.jmmm.2004.11.355.

containing a domain wall, the Zeeman energy (Section 2.1) of the material can be lowered by expansion of the domain with magnetization parallel to the applied field. A resulting Zeeman force[109],

$$F_Z = 2A_{cross}M_sH_{ext}, \tag{7}$$

where A_{cross} is the track cross-section area, causes DW motion. Wall motion proceeds at a velocity v, which can be generally written[101,107] as

$$v = \mu(H_{ext} - H_0), \tag{8}$$

with DW mobility μ and H_0 corresponding to the field required to overcome barriers to motion, such as pinning from defects and edge roughness. In Permalloy tracks, this can result in very fast DW velocities on the order of hundreds of m/s [FIG. 2-5]. It should be noted that two different regimes are observed at low and high applied field, corresponding to DW propagation either by sliding or turbulent motion, respectively. In both cases, however, the relation of Eq. (8) holds true, and it is only the DW mobility, due to the difference in mode of DW propagation, that differs.

2.2.3 Domain wall logic

In Section 2.2.2, the dc application of a field parallel to a straight DW-containing track caused the high-speed propagation of that DW along the stripe. Further studies of DW motion have found that time varying fields can be used to propagate DWs along non-linear elements. Indeed, a rotating field can be used to maneuver DWs through circular[44,45,116,117] [FIG. 2-6(a)] and more complicated[106,111] [FIG. 2-6(b)] geometries, with the sense (clockwise or counterclockwise) of field rotation determining the direction of DW motion. In such curved elements, the position, and consequently the speed, of a DW can be precisely controlled. This ability to prescribe DW position and speed in curved elements will be critical to the manipulation of superparamagnetic beads, which are the subject of the following section.

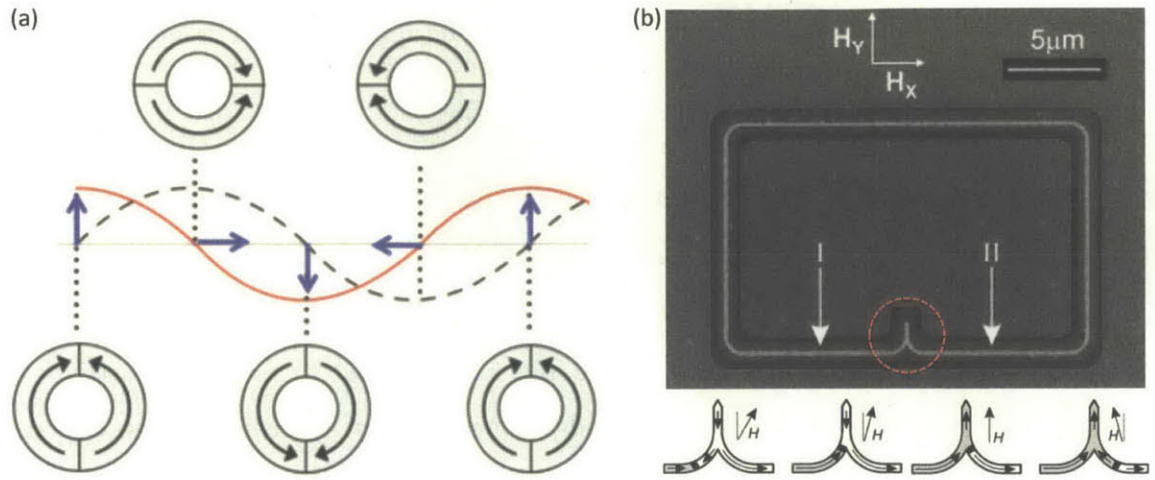

FIG. 2-6 Domain wall motion in non-linear elements

(a) Schematic describing the propagation of a domain wall around a magnetic ring by a rotating in-plane field. Reprinted with permission from Negoita, M., Hayward, T. J. & Allwood, D. A. Controlling domain walls velocities in ferromagnetic ring-shaped nanowires. *Appl. Phys. Lett.* **100,** 072405 (2012). Copyright 2012, AIP Publishing LLC. Available at http://dx.doi.org/10.1063/1.4812388. (b) Focused ion beam image of a Permalloy magnetic ring with a NOT junction (dashed circle) and schematics showing the domain wall propagation through the NOT junction when subject to a rotating in-plane field. From Allwood, D. A. *et al.* Submicrometer Ferromagnetic NOT Gate and Shift Register. *Science* **296,** 2003–2006 (2002). Reprinted with permission from AAAS. DOI: 10.1126/science.1070595.

2.3 Superparamagnetic beads

Magnetic particles for lab-on-chip and biomedical applications are generally superparamagnetic and range in size from tens of nanometers to several microns in diameter[12-14,18,79]. Given that superparamagnetism is a size-based effect (Section 2.3.1), larger particles are not themselves superparamagnetic. However, micron sized beads can be designed to exhibit superparamagnetic behavior. These beads are composed of small, superparamagnetic grains (usually iron oxide, 8-15 nm) embedded in a polymer matrix such as polystyrene[72] [FIG. 2-7]. The matrix serves to separate the individual superparamagnetic grains, thus reducing interparticle interaction that would otherwise result in the loss of superparamagnetism. Surrounding the magnetic core is usually a surface coating that serves to stabilize the beads in solution and render them non-toxic and biocompatible.

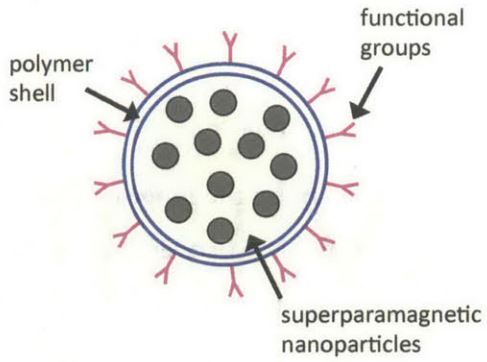

FIG. 2-7 Superparamagnetic microbead

Schematic of the typical superparamagnetic microbead structure. The core consists of superparamagnetic nanoparticles embedded in a polymer matrix. Functional groups decorate the microbead surface.

The choice of particle or bead depends on the intended application, but the advantages are common across the space. With functionalizable surfaces and sizes comparable to those of cells (10-100 um), viruses (20-450 nm), proteins (5-50 nm) and genes (2 nm wide, 10-100 nm long)[13], they can get close to and even tag biological entities of interest. Owing to their superparamagnetic nature, they are responsive to magnetic fields, yet do not maintain their magnetization upon field removal, enabling collection from and resuspension in solution. Furthermore, because biological samples are generally nonmagnetic, this action at a distance[13] is isolated to the magnetic particles, with little disturbance to the bioentity. And unlike with electric manipulation, the magnetic interaction is insensitive to variations in biological variables such as charge, pH, ionic concentration, and temperature[15].

Given the advantages of SPM particles and beads, their popularity is not surprising. In the following sections, we discuss the origins of superparamagnetism and the relevant forces on such particles and beads.

2.3.1 Superparamagnetism

Superparamagnetism is fundamentally a size-based phenomenon that occurs in ferromagnetic materials of the nanometer scale. At the small scale, the reduction in energy from realization of a multidomain magnetic configuration does not outweigh the energy penalty from introduction of a domain wall. The result is a single domain particle, with

magnetization reversal occurring via coherent spin rotation, rather than through domain expansion via domain wall propagation. The critical radius below which a particle will be single domain is given[109] by:

$$R_{sd} \approx \frac{9\sqrt{AK_u}}{\mu_0 M_S^2}. \tag{9}$$

For most magnetic materials, this radius is in the range of 10-100 nm.

From a macroscopic view, the difference between ferromagnetic and superparamagnetic materials is observed in their magnetization response to applied fields [FIG. 2-8(a)]. Whereas a ferromagnet [FIG. 2-8 (a, left)] exhibits hysteresis, due to the energy needed to overcome barriers to domain wall motion, and a nonzero remnant magnetization $\boldsymbol{M_r}$ in zero field, superparamagnetic material [FIG. 2-8 (a, right)] is non-hysteretic, has zero remnant magnetization, and a magnetization $\boldsymbol{M}$ before saturation proportional to the field $\boldsymbol{H}$ given by the expression

$$\boldsymbol{M} = \chi \boldsymbol{H} \tag{10}$$

where χ is the effective volume magnetic susceptibility of the bead. Combining this expression with that for magnetic moment,

$$\boldsymbol{m} = V\boldsymbol{M} \tag{11}$$

where $\boldsymbol{m}$ is the magnetic moment and V is the volume of the bead, we can get an expression for the magnetic moment of a bead as a function of field:

$$\boldsymbol{m} = V\chi\boldsymbol{H} \tag{12}$$

From Eq. (12) we see that in addition to the field, the moment of a bead also scales with its volume and susceptibility.

The zero remnant magnetization of superparamagnetic beads is understood when we consider the relaxation time, τ, for the net magnetization of a particle,

$$\tau = \tau_0 e^{\left(\frac{\Delta E}{k_B T}\right)} \tag{13}$$

where $k_B T$ is thermal energy, and the energy barrier to moment rotation ΔE is proportional to particle anisotropy and volume. At room temperature and for small particles, the energy barrier to magnetization rotation is comparable to thermal energy, so the time-averaged magnetization of the particle is measured as zero [FIG. 2-8 (b)]. Here we note that in addition to temperature and particle variables, the observation of superparamagnetism also depends on the measurement time τ_m. For $\tau \ll \tau_m$, rotation is fast relative to measurement,

and we observe superparamagnetism. For $\tau \gg \tau_m$, however, rotation is slow and quasi-static properties are observed[13].

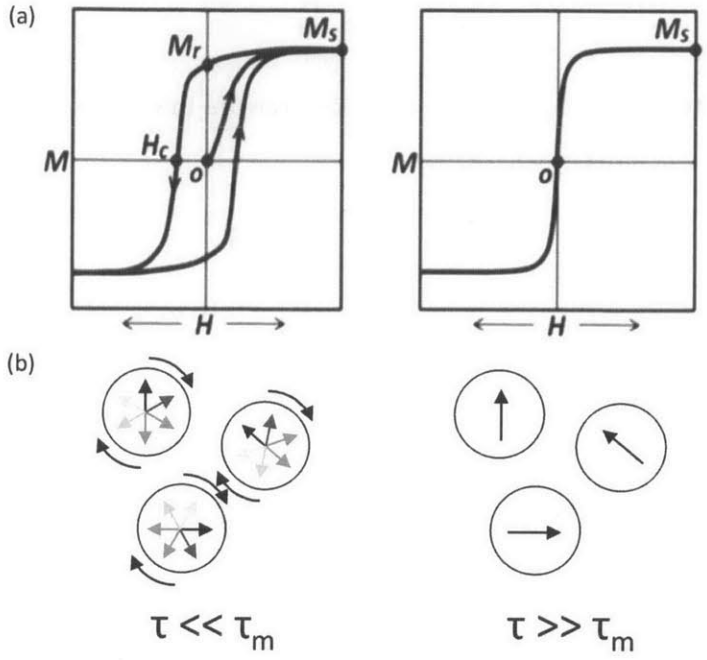

FIG. 2-8 Superparamagnetism

(a) Contrasting M-H loops for (left) ferromagnetic and (right) superparamagnetic materials. (b) The observed magnetization state of a superparamagnetic particle as a function of measurement time τ_m and particle relaxation time τ. (left) For long τ_m compared to τ, no net magnetization is observed. Reproduced from Frey, N. A., Peng, S., Cheng, K. & Sun, S. Magnetic nanoparticles: synthesis, functionalization, and applications in bioimaging and magnetic energy storage. *Chem. Soc. Rev.* **38,** 2532–2542 (2009) with permission of The Royal Society of Chemistry. DOI: 10.1039/B815548H. (right) For short τ_m compared to τ, the particle appears to have a non-zero magnetization vector. Adapted from Pankhurst, Q. A., Connolly, J., Jones, S. K. & Dobson, J. Applications of magnetic nanoparticles in biomedicine. *J. Phys. D: Appl. Phys.* **36,** R167–R181 (2003).

2.3.2 Magnetic force on bead in a magnetic field

Superparamagnetic beads are responsive to gradient magnetic fields. The form of this interaction can be derived from consideration of the potential energy of a moment $\boldsymbol{m}$ in a field $\boldsymbol{B}$:

$$U = -\boldsymbol{m} \cdot \boldsymbol{B} \tag{14}$$

Combining this with the general expression for a force as a function of potential energy U,

$$\boldsymbol{F} = -\nabla U \tag{15}$$

we obtain the expression for the force $\boldsymbol{F_m}$ on a magnetic dipole in a magnetic field:

$$\boldsymbol{F_m} = (\boldsymbol{m} \cdot \nabla)\boldsymbol{B} \tag{16}$$

Substituting in the expression for the magnetic moment Eq. (12) and using the relation

$$\boldsymbol{H} = \frac{\boldsymbol{B}}{\mu_0} \tag{17}$$

where μ_0 is the permeability of free space, we can rewrite this expression for the force on a magnetic dipole in a magnetic field gradient as:

$$\boldsymbol{F_m} = \frac{V\chi}{\mu_0}(\mathbf{B} \cdot \nabla)\mathbf{B} \tag{18}$$

From Eq. (18) we see that the magnetic force on a bead is a function of the nature of both the field and bead.

2.3.3 Drag force on beads in viscous medium

For bead transport through a liquid phase, it is necessary to consider the force exerted on a bead by a fluid. The relative importance of viscous and inertial effects on fluid moving past a particle of radius r is characterized by the dimensionless Reynolds number R_e defined as:

$$R_e = \frac{\rho v r}{\eta} \tag{19}$$

where ρ is the fluid density, v relative velocity between fluid and particle, and η is the fluid viscosity. For laminar flow, low Reynolds number R_e systems i.e. $R_e \ll 1$, motion is in the strongly viscous or creeping motion regime[118] and the hydrodynamic drag $\boldsymbol{F_d}$ force that the bead experiences due to motion through the liquid phase is given by Stoke's law[118],

$$\boldsymbol{F_d} = -6\pi\eta R\boldsymbol{v} \tag{20}$$

where R is the bead radius.

For a bead dragged parallel to a single plane wall at a distance l from its center, Faxen et al. worked out that a near surface correction factor of ξ is introduced of the form[118]

$$\xi = \frac{1}{1-\left(\frac{9}{16}\right)\left(\frac{R}{l}\right)+\left(\frac{1}{8}\right)\left(\frac{R}{l}\right)^3-\left(\frac{45}{256}\right)\left(\frac{R}{l}\right)^4-\left(\frac{1}{16}\right)\left(\frac{R}{l}\right)^5}, \tag{21}$$

resulting in modified drag force now given as:

$$\boldsymbol{F_d} = -6\pi\eta\xi r\boldsymbol{v}. \tag{22}$$

2.3.4 Other forces

Other forces[23,72,119] exerted on the bead include electrostatic, including Van der Waals attraction and double layer repulsion as described by DLVO theory, hydrophobic, and interbead magnetic forces. These are complicated forces that are unique to a particular substrate-liquid-bead system, and thus difficult to model in a general way. As such, these are not considered explicitly in our models, but they are important to keep in mind as potential sources of variation between simulated and experimental results.

2.4 Magnetoresistance

In 1988 Baibich et al.[86] and Binasch et al.[87] discovered the phenomenon now known as giant magnetoresistance, wherein the resistance through a stack of alternating ferromagnetic (FM) and nonmagnetic (NM) layers depends on the relative orientation of the magnetization of the FM layers in the stack. The effect is due to spin-dependent scattering and is explained schematically in FIG. 2-9(a). Here, a current is passed through a FM/NM stack in the current-perpendicular-to-the-plane (CPP) geometry. In most applications, however, the current-in-the-plane (CIP) geometry is used because it is easier to measure. In either case, the charge current passing through the FM material can be considered to be composed of two parallel and independent sub-currents, carried by the spin-up and spin-down electrons, each with their own spin-dependent scattering rate. Electrons with their spins parallel to the direction of magnetization in the FM layer experience less scattering and thus lower resistance than those with their spin antiparallel to the magnetization.

Given this spin-dependent resistance, we can now understand the resistance response of a FM/NM giant magnetoresistance stack as a function of field [FIG. 2-9(b)]. At zero field, antiferromagnetic coupling between the layers causes the magnetization of adjacent layers to lie antiparallel, such that both the spin-up and spin-down sub-currents experience high scattering rates in half the layers, resulting in an overall large resistance. With the application of a large enough field in either direction, the magnetization of all the layers line up parallel

along the applied field axis. In this case, the low resistance of the electrons with their spins parallel to the magnetization of the layers dominates the overall resistance, and it is observed to be low. FIG. 2-9(c) shows a pseudo-spin-valve, another type of magnetoresistive device, and its characteristic resistance response under applied field. Here, the coercivity of the two magnetic layers differ, such that the magnetization of the two ferromagnetic layers is antiparallel and parallel at intermediate and high field values, respectively, resulting in high and low resistance, respectively. In the spin-valve device scheme [FIG. 2-9(d)], only one of the layers is free to change the direction of its magnetization, while the other is has its magnetization pinned by an adjacent antiferromagnetic layer via exchange coupling.

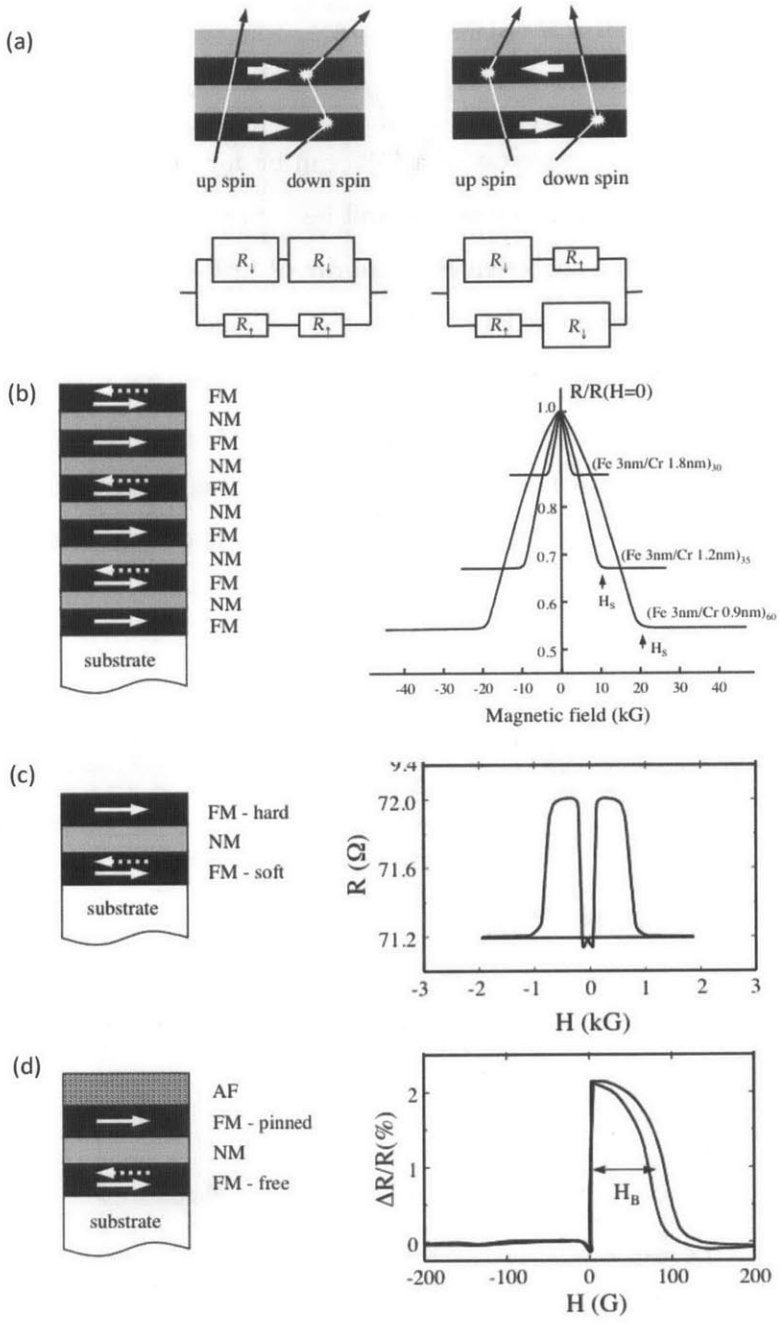

FIG. 2-9 Magnetoresistance and magnetoresistive devices

(a) Schematic illustration of electron transport through a FM/NM multilayer in the current-perpendicular-to-the-plane geometry in which the magnetization directions of adjacent FM layers are either parallel or antiparallel aligned, and corresponding two-current series resistor model. (left) In the parallel configuration, scattering for the up-spin and down-spin electrons is low and high, respectively. Given that the two spin currents flow in parallel, the overall resistance is low. (right) For the antiparallel configuration, scattering for both the up-spin and down-spin electrons is high, so the overall resistance is high. (b-d) Structure and characteristic magnetoresistive response curve of a (b) giant magnetoresistance multilayer stack, (c) pseudo-spin-valve, and (d) spin-valve. (a-d) Adapted from Tsymbal, E. Y. & Pettifor, D. G. *Perspectives of giant magnetoresistance.* Published in *Solid State Physics.* **56**, 113-237 (Academic Press, 2001) after (b) Baibich, M. N., Broto, J. M., Fert, A., Nguyen Van Dau, F. & Petroff, F. Giant magnetoresistance of (001)Fe/(001)Cr magnetic superlattices. *Phys. Rev. Lett.* **61,** 2472–2475 (1988), (c) Barnas, J., Fuss, A., Camley, R. E., Grunberg, P. & Zinn,

W. Novel magnetoresistance effect in layered magnetic structures: Theory and experiment. *Phys. Rev. B* **42,** 8110–8120 (1990), and (d) Dieny, B. *et al.* Giant magnetoresistance in soft ferromagnetic multilayers. *Phys. Rev. B* **43,** 1297–1300 (1991).

FIG. 2-10 shows how the position of a DW can be measured with a magnetoresistive device. In this case, the resistance measured will be a function of wall position along the track. If the wall is positioned such that the majority of DW-containing layer is magnetized parallel to the pinned ferromagnetic layer below, the resistance will be relatively low. On the other hand, if the wall is positioned such that the majority of the DW-containing layer is magnetized anti-parallel to the pinned ferromagnetic layer, the resistance will be higher. Thus, the resistance of a track will be proportional to the distance a wall has moved along it in a given time. This ability to track the position of a DW via electrical measurement will be taken advantage of in Section 7.3.

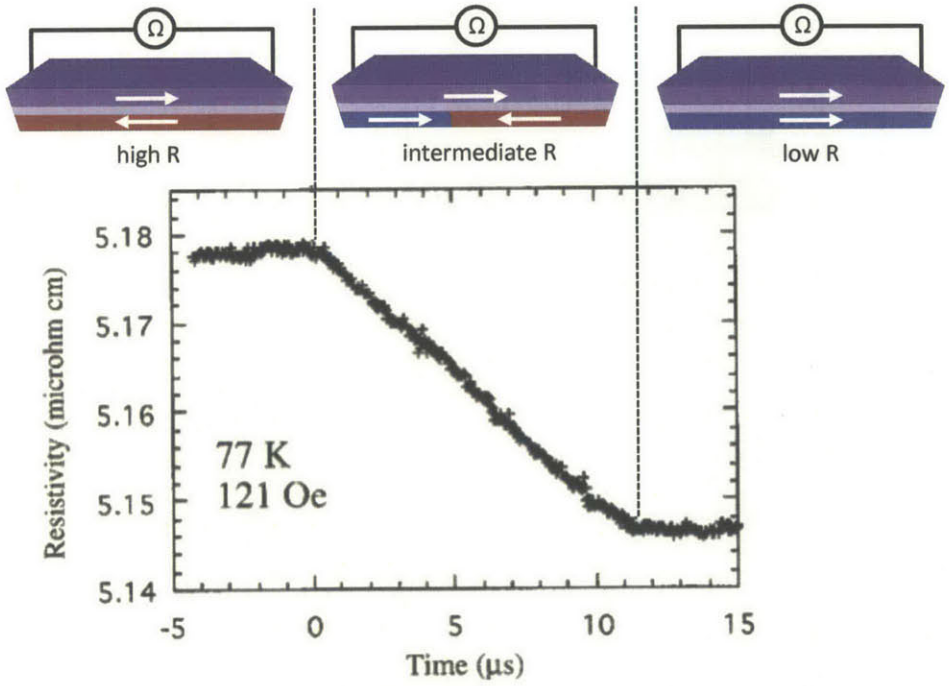

FIG. 2-10 Magetorsisiance versus domain wall position

Resistance versus time during the magnetization reversal of the 40 nm NiFe layer in a NiFe(40 nm)/Cu/NiFe(5 nm) stack at 77 K. The three distinct parts of the curve correspond to three distinct configurations of magnetization between the two ferromagnetic layers during magnetization reversal. For full antiparallel (parallel) magnetization alignment, resistance is high (low). Between these states, as the magnetization of the bottom layer reverses via domain wall motion, the magnetization of the layers is part parallel and part antiparallel aligned, resulting in intermediate resistance as a function of domain wall position. From Ono, T. *et al.* Propagation of a magnetic domain wall in a submicrometer magnetic wire. *Science* **284,** 468–470 (1999). Reprinted with permission from AAAS. DOI: 10.1126/science.284.5413.468.

Chapter 3

Simulation and experimental methods[1]

The thrust of this thesis work has been the investigation of the bead-DW interaction for the realization of an integrated magnetic lab-on-chip system. In order to conduct these studies, both simulation and experimental methods, standard and custom, were employed. Here we discuss the details of these methods.

3.1 Simulation of bead-domain wall interaction

An SPM bead sitting in the stray field of a domain wall has a magnetostatic potential energy Eq. (14). This results in a magnetic interaction force, defined as the negative gradient of the magnetostatic potential energy Eq. (15) between the wall and the bead. We quantitatively define the strength of bead-DW coupling as the maximum interaction force along the intended direction of bead-DW motion. We call this the binding force between a bead and DW, and it is given as the maximum of the absolute longitudinal gradient of magnetostatic energy.

Previously there has been work to calculate the binding force between SPM beads and domain walls as a function of bead size[36,43,81]. These calculations have limitations, however, a major of which is the handling of both the finite volume and SPM nature of real beads. Most approaches[36,81] model the SPM bead as a point dipole rather than a spherical bead with finite volume, or as a ferromagnetic rather than superparamagnetic bead. Beyond the actual model limitations, other simulations suffer in the scope of the data collected. We have developed a flexible and high throughput calculation method that can be used to calculate magnetostatic interaction energies and binding forces between beads and DWs over a range of combinations of bead radius, track width, thickness, and geometry, and domain wall configuration.

---

[1] Sections of this chapter, including figures, have been previously published in Rapoport, E., Montana, D. & Beach, G. S. D. Integrated capture, transport, and magneto-mechanical resonant sensing of superparamagnetic microbeads using magnetic domain walls. *Lab Chip* **12,** 4433–4440 (2012). Reproduced by permission of The Royal Society of Chemistry. DOI: 10.1039/C2LC40715A.

The simulation method is three-step. Micromagnetic simulations of DW structure are first calculated, followed by numerical integration of stray fields, and finally, of potential energy surfaces of the DW-bead interaction.

The approach has several attractive features that overcome the limitations of other approaches. In separating the field calculation from that of the track magnetic configuration, we are able to calculate the DW stray field over large volumes in space, which subsequently enables calculation of relevant energies and binding forces for beads normally used in biomedical applications. We are also able to accurately model SPM bead as SPM, rather than as ferromagnetic, as has been done often before.

In the first step we use the object-oriented micromagnetic framework (OOMMF)[120] to find the relaxed DW structure in $Ni_{80}Fe_{20}$ (Permalloy) tracks of various dimensions and geometries. Given an input magnetic configuration, OOMMF determines the resulting magnetic configuration by iterative calculation of the Landau-Lifshitz-Gilbert (LLG) magnetization equation of motion, expressed[120] as

$$\frac{d\boldsymbol{M}}{dt} = -\gamma \boldsymbol{M} \times \boldsymbol{H} + \frac{\alpha}{M_s}\left(\boldsymbol{M} \times \frac{d\boldsymbol{M}}{dt}\right), \tag{23}$$

with damping parameter α and electron gyromagnetic radius γ. An OOMMF .mif input consists of several blocks defining the parameters for calculation. These generally include an atlas in which the system geometry is defined, a mesh defining the discretization imposed on the simulation, all relevant energies of the system, an evolver that is responsible for updating the magnetization configuration between steps, and a driver that coordinates evolver action and which determines when a simulation step is complete. Whichever of the two evolvers is used, Oxs_EulerEvolve or Oxs_CGEvolve, the corresponding driver, Oxs_TimeDriver or Oxs_MinDriver, respectively, must be chosen. Oxs_EulerEvolve and Oxs_TimeDriver were used for the micromagnetic calculations of this thesis.

Initialization conditions for either transverse or vortex walls are chosen depending on the track dimensions[113-115]. A magnetization profile as in FIG. 3-1(a, left) is allowed to relax to initialize a transverse wall [FIG. 3-1(a, right)], whereas an initial magnetization profile as in FIG. 3-1(b, left) is used to initialize a vortex wall [FIG. 3-1(b, right)]. The materials parameters used in simulations are those appropriate for Permalloy: exchange stiffness constant, $A = 1.3\times10^{-11}$ J m^{-1}; Gilbert damping constant, α=1.0; saturation magnetization, $M_s = 8\times10^5$ A m^{-1}; and magnetocrystalline anisotropy, $K_u = 0$ J m^{-3}. The large α value is

justified because we are only interested in the final relaxed DW structure and not in relaxation dynamics. A cell thickness equal to track thickness is used to reduce the number of cells and thus calculation time. The cell dimensions in the x-y plane (5×5 nm^2 for straight tracks, 2.5×2.5 nm^2 for curved tracks) were chosen to be roughly on the order of the exchange length [Eq. (3)] of Permalloy (~5.7 nm) or smaller.

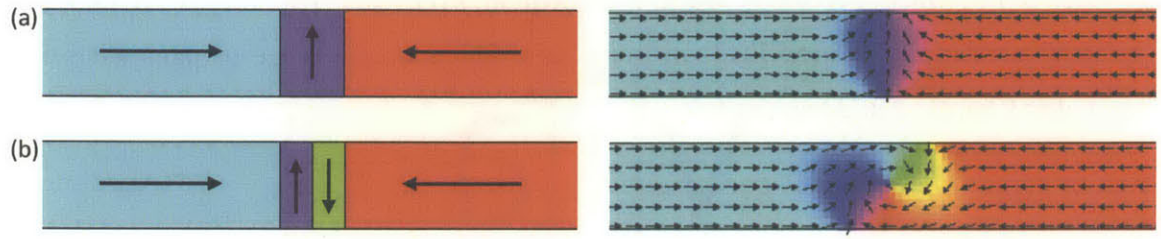

FIG. 3-1 Domain wall initialization for micromagnetic calculations

(a-b) (left) Initial and (right) resulting micromagnetically-generated relaxed spin configuration for a (a) transverse and (b) vortex domain wall.

The DW magnetization configuration output from OOMMF is used as the input for a numerical integration of the stray field coming from the domain wall. The stray field is calculated using a point dipole integration approximation, wherein each space cell i above the track has a field, $\boldsymbol{B}_i$, given by

$$\boldsymbol{B}_i = \sum_j \frac{\mu_0}{4\pi r^3}[\boldsymbol{r}_{ij}(\boldsymbol{m}_j \cdot \hat{\boldsymbol{r}}_{ij})\hat{\boldsymbol{r}}_{ij} - \boldsymbol{m}_j], \tag{24}$$

where $\boldsymbol{m}_j$ is the magnetic moment of a track cell j, $\boldsymbol{r}_{ij}$ is the distance between the space cell i and the track cell j, and $\hat{\boldsymbol{r}}_{ij}$ is the unit vector along the line connecting cells i and j. Stray fields were calculated[137] over tracks for spaces large enough to accommodate beads with diameters up to 300 nm or 2.8 μm, using a cell size of $10\times10\times10$ or $15\times15\times15$ nm^3, for curved or straight tracks, respectively. This step is the most computationally intensive, but the resulting stray field data is the basis for all subsequent calculations of DW-bead interaction potential energy surfaces and binding forces, which are fast calculations.

From the stray field, the magnetostatic potential energy of a spherical SPM bead of radius R at a height z from the top of the track was estimated by integrating the dipolar energy density $-\boldsymbol{M}\cdot\boldsymbol{B}$ over the bead volume, assuming[72] a bead magnetization $\boldsymbol{M} = \chi\boldsymbol{B}/\mu_0$ [Eq. (10) and Eq. (17)] with $\chi = 800$ kA m^{-1} T^{-1} and $M_s = 43.2$ kA m^{-1}, and a sphere demagnetization factor of 1/3. In the present calculations, bead height above the track is set

to $z = 0$ nm i.e. the bead at the track surface, because it has been shown[36,81] that there is a strong force in the negative z direction that pulls the bead towards the surface. Although it is expected that the presence of the bead may cause some distortion of the DW structure in the magnetic track, these effects were neglected in the current calculations.

With our approach, we model the bead as truly superparamagnetic. An example energy contour obtained using this method for a 1 μm diameter bead over a transverse wall in 200 nm wide, 5 nm thick Permalloy track is shown in FIG. 3-2. The results of detailed, systematic calculations of bead-DW energetics as a function of a range of parameters are presented in Chapter 4 and Section 6.4.

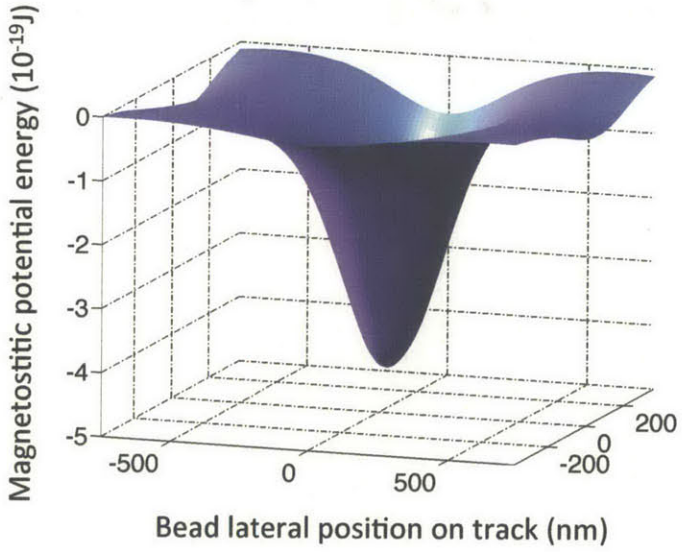

FIG. 3-2 Example magnetostatic potential energy well

Magnetostatic potential energy well calculated for a 1.0 μm diameter SPM bead sitting above a transverse wall in 200 nm wide, 5 nm thick Permalloy track.

3.2 Sample fabrication

All sample devices were prepared by a combination of lithographic patterning, deposition, and in the case of electron beam or optical lithography, liftoff. Three types of samples were fabricated for this work, each requiring a different combination of the aforementioned steps. For all non-eclectically contacted samples, fabrication consisted of electron beam lithography, sputter deposition, and liftoff on Si(100) wafers with native oxide

(SiO_2). The fabrication of pseudo-spin-valve test structures for stack composition optimization consisted of shadow mask lithography and sputtering on Si wafers with 50 nm thermally-grown SiO_2. Lastly, samples for electrical measurement of DW position (Section 7.3) were fabricated by a combination of electron beam lithography and sputtering, and optical lithography and evaporative deposition for devices and contacts, respectively, on Si wafers with 50 nm thermally-grown SiO_2. All samples that were tested with beads were also covered in a final 70-150 nm thick SiO_2 passivation layer via rf sputter deposition. The thicker oxide layers were used to prevent shorts in samples that underwent electrical testing. The details of each of these fabrication steps are discussed in the sections that follow.

3.2.1 Shadow mask lithography

Shadow mask lithography is a simple method for creating patterned thin films in which a pre-fabricated mask cut with features of arbitrary geometry is used. During deposition, the shadow mask is mounted on or above the sample such that it is between the substrate and deposition source, resulting in selective material deposition in the regions not blocked by the mask. The advantages of this technique include mask reuse and one-step fabrication. However, it suffers from potential mask clogging by deposited material, and resolution in pattern placement and size is limited as compared to in other lithographic processes. Shadow mask lithography was used to fabricate test pseudo-spin-valve structures (Section 7.3), for which composition rather than lateral dimensions were important.

3.2.2 Electron beam and optical lithography

For structures requiring a higher level of resolution than can be achieved by shadow mask lithography, photolithographic techniques such as electron beam and optical lithography are preferred. In both cases, a polymeric mask is created directly on a sample surface by exposure of a photosensitive polymer resist to light, and followed by subsequent chemical development to remove unwanted polymeric material. During development, whether those regions exposed to or shielded from light are removed is a function of whether positive or negative resist, respectively, is used. In optical lithography, a mask placed

between the resist and light source determines the resulting lithographic pattern. In the case of electron beam lithography, a focused beam of electrons is rastered to selectively expose certain regions of resist.

Structures for direct electrical contact to devices were patterned by optical lithography. Fabrication first consisted of mask generation via optical lithography. A chrome/photoresist on glass plate was patterned with a Heidelberg μPG 101 (365 nm UV) desktop microlithography system and developed in 352 developer for 1 minute, then rinsed in deionized water and dried in nitrogen. The chrome was etched with CR-7 chrome etchant and then rinsed in order with water, acetone, methanol, and isopropanol, and dried with nitrogen. The mask was put through a final descum step in the plasma asher (Technics PlanarEtch II with Model 750 plasma generator) at 200 W under ~350 mTorr O_2 flow for 1-2 minutes.

Sample substrates were treated with an initial layer of hexamethyldisilazane (HMDS) to promote subsequent photoresist adhesion. The HDMS was applied for 1 min and then spun of at 3000 rotations per minute (rpm) to remove the excess. S1813 photoresist was spun onto the pretreated substrate at 3000 rpm for 1 minute and then baked on a hot plate for 3 minutes at $90°$. The resist-coated substrate was then exposed through the chrome mask (chrome side down) in a Tamarack mercury lamp system for a total of 75 seconds (15 second initial exposure, 1 minute wait time to allow for outgassing, and then final 60 second exposure) and developed in 352 developing solution for 1 minute. Finally, samples were rinsed in deionized water and dried with nitrogen.

Devices were patterned by electron beam lithography. Poly(methyl methacralate) (PMMA) positive resist was spin-coated on substrates at 2000 rpm for 1 minute to achieve a PMMA thickness of ~150 nm. Resist-coated substrates were then baked either in an oven at $150 - 170°$ for 30-60 minutes or on a hot plate at $180 - 185°$ for 90 seconds. A Raith 150 scanning electron beam (10 keV) was used to pattern the resist. Finally, resist patterns were developed for 90 seconds in 3:1 (by volume) isopropanol:methyl isobutyl ketone (MIBK) solution, rinsed with isopropanol, dried with nitrogen, and descummed in the Asher at 50 W under ~350 mTorr O_2 flow for 2-5 seconds.

3.2.3 Sputter and evaporative deposition

Sputter deposition is a thin film growth technique by which material ejected from a target by ion bombardment is deposited on a substrate. All devices and surface passivation layers were grown in a 4-target dc/rf magnetron sputterer operating at a base pressure of $\sim 10^{-7} - 10^{-8}$ Torr. Metallic layers were generally deposited in rotation mode under an argon pressure of 2-3 mTorr using a dc power supply at 0.05-0.4 A and 300-450 V. An rf power supply operating at 200 W was used for SiO_2 deposition. The thickness of deposited layers was defined by the material deposition time and rate, where rates were calculated from the thickness of test films deposited for a known time. Film thicknesses were obtained via x-ray reflectivity or ellipsometry of metallic or SiO_2 films, respectively. In all cases, targets were pre-sputtered for at least a minute to clear them of surface contaminants before material deposition.

Au/Ti contacts were deposited in the MIT NanoStructures Lab by electron beam evaporation, which uses a focused electron beam to locally melt and evaporate target material onto a substrate. The Ti underlayer was used to promote adhesion between the Au film and SiO_2 substrate surface.

3.2.4 Liftoff

Liftoff is the final step in the fabrication process consisting of photolithographic masking and deposition in which photoresist is removed from the substrate, leaving only the deposited material in the desired pattern. Lift-off was done in 135 °C N-methyl-2-pyrrolidinone (NMP) with periodic 30 second sonication intervals for ~10 minutes, followed by a rinse in acetone, methanol, and isopropanol and drying in nitrogen.

3.3 Sample characterization and data acquisition

This section discusses the various techniques, tools, and programs used to obtain and analyze the experimental data discussed in this thesis.

3.3.1 Scanning electron beam microscope

Scanning electron microscopes (SEMs) exploit the interaction between a focused beam of electrons and a material to investigate the topographic and compositional information of sample surfaces. The dimensions and quality of patterned structures were characterized with a Zeiss/Leo Gemini 982 SEM operating at 5 keV.

3.3.2 Superparamagnetic beads

Experiments were performed using three different types of commercially available superparamagnetic beads. These were Dynabeads MyOne Carboxylic Acid (1.0 μ m diameter) and Dynabeads M-270 Carboxylic Acid (2.8 μm diameter) from Life Technologies, and COMPEL Magnetic, COOH modified (UMC3N/11086) beads (5.8 μm diameter) from Bangs Laboratories. These beads will be referred to as MyOne, M-270, and COMPEL, respectively, throughout the remainder of this thesis. In each case, the stock bead solutions were diluted down to ~10^5 beads/mL either in deionized water or phosphate buffered saline solution with optional 0.1 % (v/v) Tween 20 detergent.

3.3.3 Sample preparation

Samples of lithographically defined thin-film magnetic tracks on Si wafers were used as DW conduits [FIG. 3-3(a)]. A dilute suspension of SPM beads (Section 3.3.2) would be placed in a PDMS well on the wafer surface [FIG. 3-3(b-c)] and sealed with a microscope cover slip [FIG. 3-3(d)]. The sample with suspended SPM beads was then placed in the plane between the poles of a custom vector electromagnet (Section 3.3.4), and an in-plane drive field was used to initialize DWs within the track. Bead capture by DW fringing fields was monitored via a CCD camera fitted to a custom microscope apparatus (Section 3.3.7). Beads far from the tracks executed a Brownian random walk across the wafer surface, but those wandering to within ~ 10 μm of a track were abruptly drawn towards and trapped by the nearest DW. A significant number of capture events typically occurred across the array within a few minutes of bead introduction.

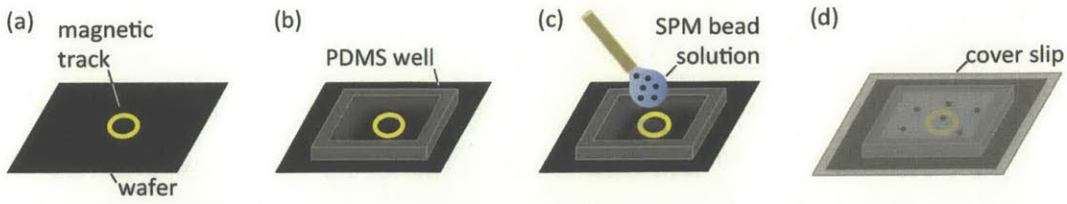

FIG. 3-3 Sample preparation with suspension of magnetic beads

(a) Sample before bead deposition. (b) Sample overlain with PDMS well. (c) Deposition of bead suspension into PDMS well. (d) Sample with bead suspension covered with glass cover slip.

3.3.4 Custom vector electromagnet

In order to conduct bead transport studies, it was necessary to design a projection magnet capable of producing a large, rotating, high bandwidth, and homogenous in-plane vector field. Large enough fields were necessary to initialize and propagate DWs. As will be discussed in more detail in Section 5.1, a rotating field was required for controlled domain wall, and thus bead, motion. The high bandwidth requirement was important to both bead velocity (Chapter 5) and magneto-mechanical resonance (Chapter 7) measurements. The field homogeneity requirement was important to ensure that bead motion was due to the domain wall stray fields and not to the external field. Using Infolytica's MagNet software to model the fields produced by a quadrupole magnet, we determined the optimum pole piece geometry that maximized the region of homogeneous field to a 2×2 mm^2 area, which is much larger than the region occupied by the lithographically defined magnetic structures. The geometry is also such that it allows for convenient optical access to samples while still

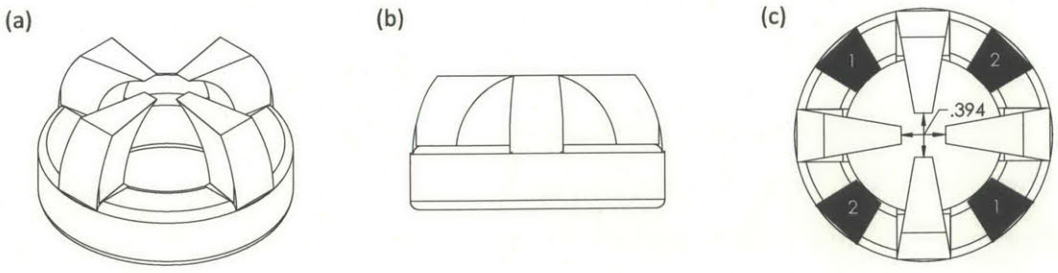

FIG. 3-4 Vector electromagnet schematics

(a-c) Entire magnet assembly from (a) top-side, (b) side, and (c) top-down view. Location of coil pairs (1-1 and 2-2) indicated in (c). Schematics by A. Gallant at the MIT Central Machine Shop, based on given specifications and drawings.

ensuring that the sample is in the region of homogeneous field. The schematics for the optimized geometry are shown in FIG. 3-4(a-c).

The black trapezoids in FIG. 3-4(c) indicate where pairs (1-1 and 2-2) of in-series electromagnetic coils are wound, with each pair driven by its own current channel. To generate a rotating vector field in the plane of the magnet, the two current channels are driven by sinusoidal current waveforms offset from each other by 90°. FIG. 3-5 shows the field angle as a function of current in the two channels for various points during rotation.

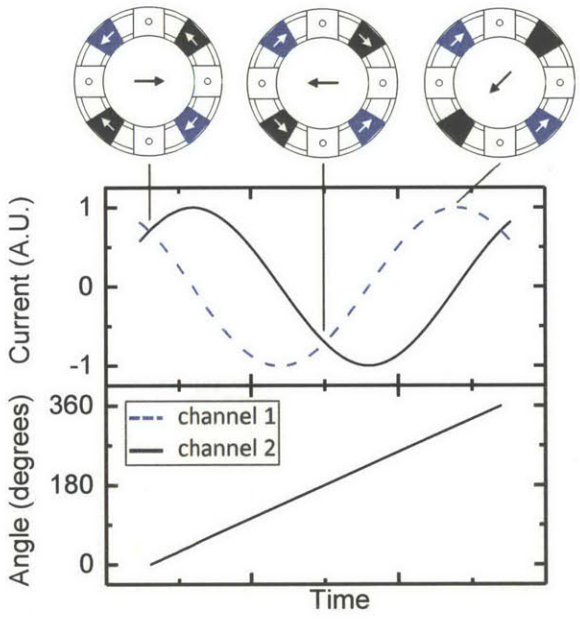

FIG. 3-5 Vector electromagnet field vector

Field vector angle as a function of relative current in channels 1 and 2, corresponding to current through coil pairs 1-1 and 2-2, respectively.

We constructed a magnet based on this optimum geometry using iron powder cores from Micrometals (powder mix -26). Powder cores were chosen for their low losses at high frequencies. Because of the brittle nature of the powder cores, an Electric Discharge Machine (EDM) was used for precision cutting. The constructed magnet is seen in FIG. 3-6(a) below. The entire magnet assembly has a small footprint of only 3.5×6 in^2, suitable for point-of-care applications. It also includes several accessory components including an air coil [FIG. 3-6(b)] for vertical field generation in addition to the vector field, and a contact plate [FIG. 3-6(c)] and switchbox for sample electrical measurements. When in use, the

vertical field electromagnet sits on top of the vector magnet, aligned to center with 4 pins. It generates ~68 Oe A^{-1} and allows for continued optical access owing to its 1 in diameter through hole. The contact plate and switchbox will be discussed in more detail in Section 3.3.5.

The in-plane field magnitude of the vector electromagnet was measured along a grid of points covering the active area between the pole pieces. Using a Gaussmeter mounted on a micrometer at fixed height, the field was measured as the magnet moved via a precision axis

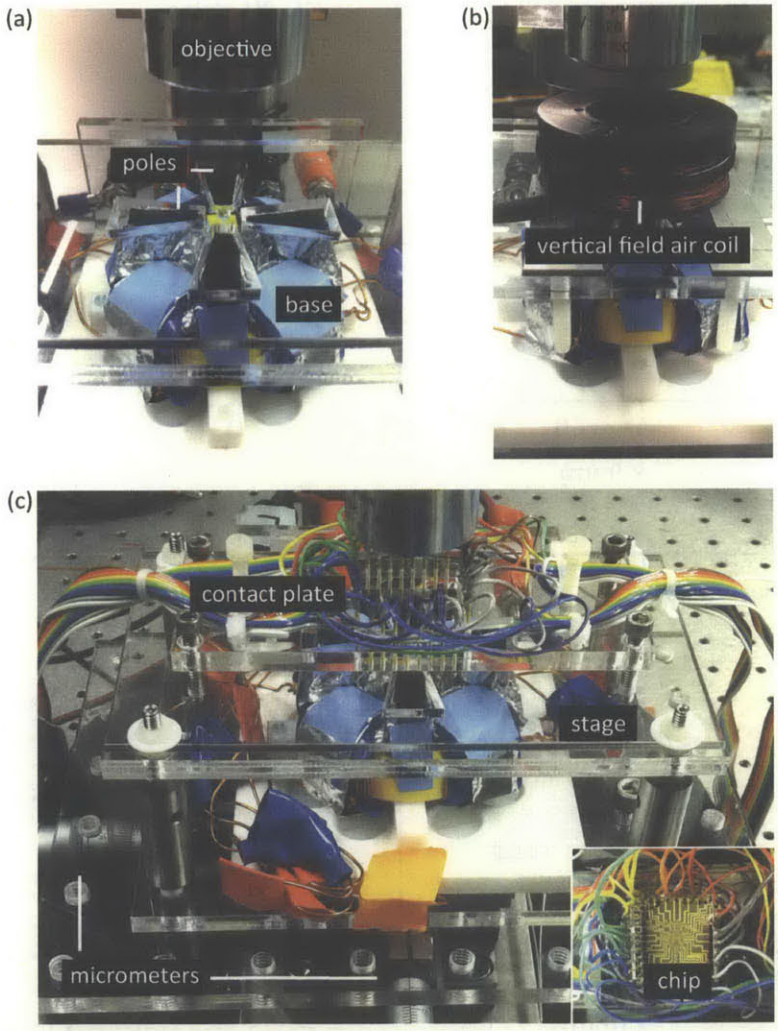

FIG. 3-6 Vector electromagnet assembly

(a) Constructed vector electromagnet integrated with optical imaging capability, with magnet base and poles indicated. (b) Vector electromagnet with optional vertical field air coil in place. (c) Entire magnet assembly (measuring $3.5\times6.6\times6.2\ in^3$) for on-chip bead manipulation and electrical measurement. Stage for sample mounting and contact plate for electrical contact to chips (inset) are indicated.

stage by 100 μm steps. For each of the +x, +y, -x, and -y field orientations, the grid was measured twice, with the Gaussmeter probe at orthogonal positions, in order to calculate the field vector at each grid point. FIG. 3-7 and FIG. 3-8 plot measured points for the field pointing along each of the four directions +x, +y, -x, and -y where the field amplitude is within 5% of that at center and the field angle is within 5° of the nominal field angle, respectively. Both the field amplitude and angle are found to be relatively homogenous within the 2×2 mm^2 center region. The field was also probed vertically via micrometer

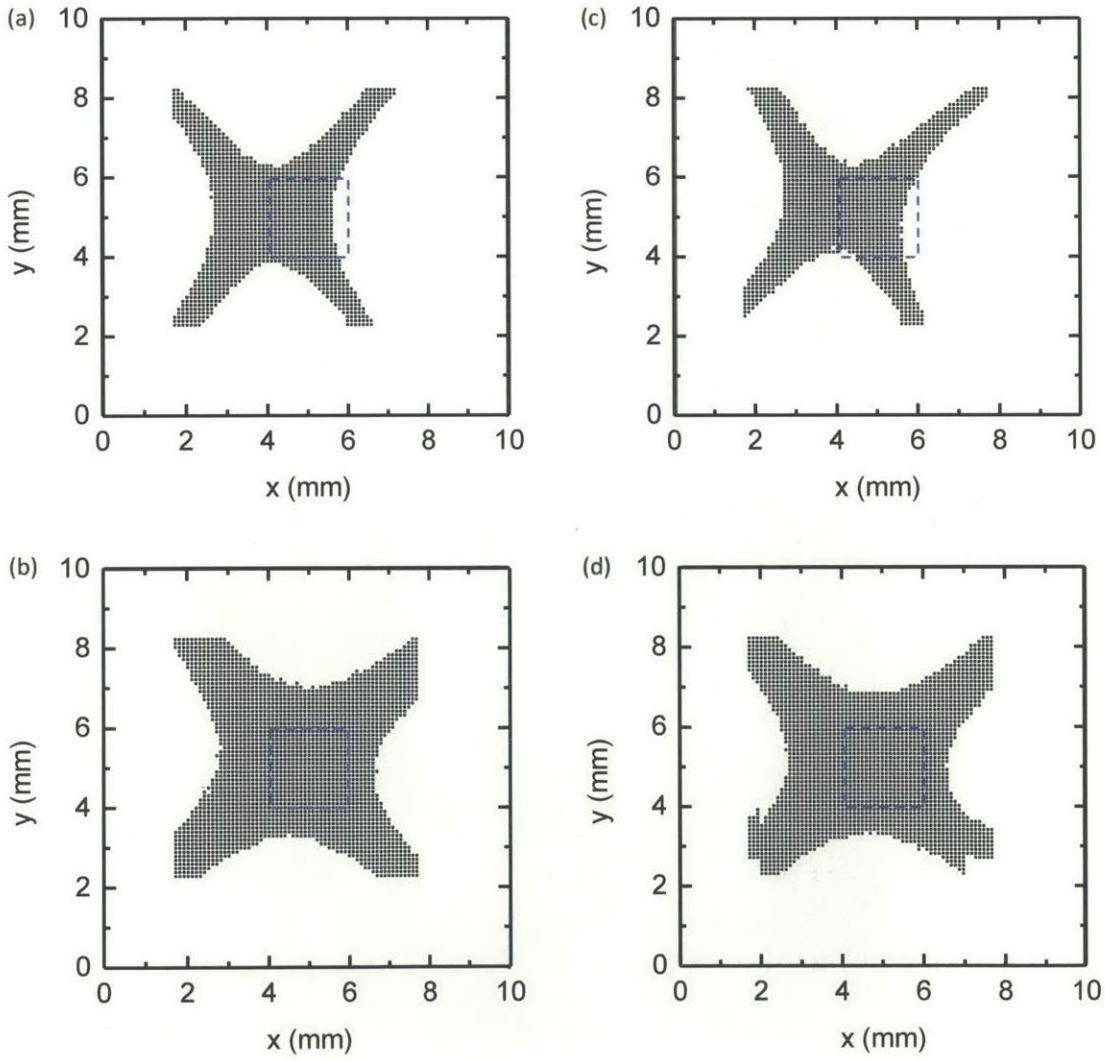

FIG. 3-7 Vector electromagnet field amplitude homogeneity

(a-d) Measured points with field amplitude within 5% of that at center of magnet active area when field points along (a) +x, (b) +y, (c) –x, and (d) –y. Field amplitude is nearly homogeneous within the $4\ mm^2$ dashed square area at center.

adjustment in the center of the magnet and found to be constant over a range of several millimeters above the plane of the pole pieces.

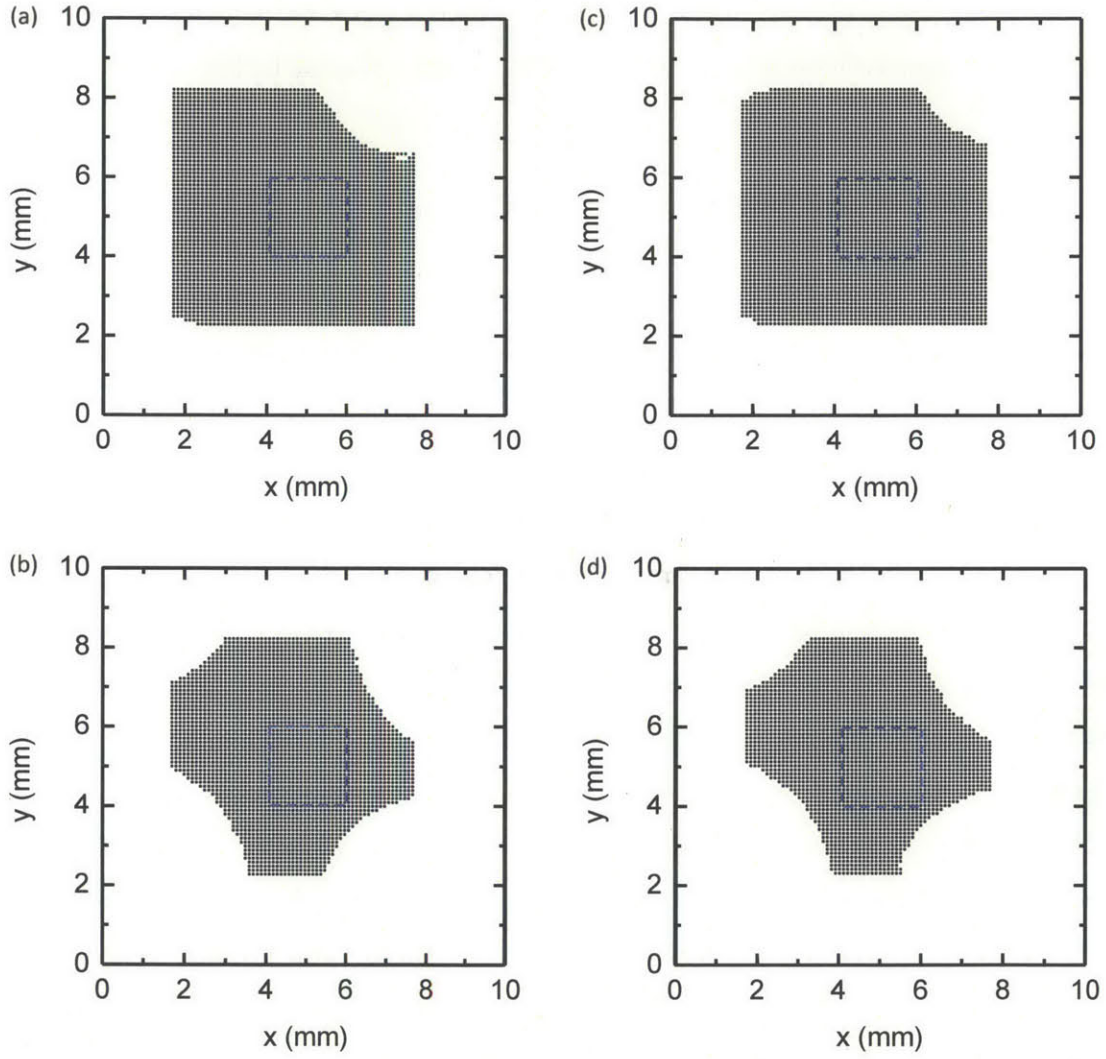

FIG. 3-8 Vector electromagnet field angle homogeneity

(a-d) Measured points with field angle within 5° of nominal angle when when field points along (a) +x, (b) +y, (c) –x, and (d) –y. Field angle is nearly homogeneous within the $4\ mm^2$ dashed square area at center.

The magnet, powered by a two-channel power amplifier (Crown DC-300A Series II or Tecron 5530), can generate in-plane fields of up to ~500 Oe and has a bandwidth of ~1 kHz. The magnet has a high field-to-current ration of ~40 Oe A^{-1} (with the same current amplitude in both channels). It follows from FIG. 3-5 that a field with magnitude X Oe at an angle θ is generated when the current in the two channels is of the form:

$$Channel\ 1 = \frac{X}{40}\sin(\theta + \frac{\pi}{4}) \tag{25}$$

$$Channel\ 2 = \frac{X}{40}\cos(\theta + \frac{\pi}{4}) \tag{26}$$

It is important to note that the high field-to-current ratio is especially beneficial because large fields can be generated without overheating, which would otherwise be harmful to biological samples.

3.3.5 Contact plate and switchbox for electrical characterization

In Section 7.3, we describe the electrical measurements of DW oscillation as a means of identifying a bead. For these measurements, a custom electrical probe contact plate [FIG. 3-6(b)] and switchbox were used. 32 spring-loaded contact pin probes (pogo receptacle PR261-1 and P2662BG-1R1S pogo from Ostby Barton Pylon) fixed along the perimeter of a square window ($1\times1\ in^2$) in an acrylic plate make contact to sample devices [FIG. 3-6(b, inset)] via gold contact pads (2×2 mm^2) and tracks patterned and deposited by optical lithography and electron beam evaporation, respectively. The contact plate mates with the quadrupole vector magnet stage such that the optical access is maintained and sample devices are centered with respect to the magnet. Simultaneous contact can be made to up to 8 devices for four-point probe resistance measurements. The probes are wired to a switchbox though which connection to a current source and voltmeter can be made to any of the 8 devices. FIG. 3-9(a) shows a schematic representation of the contact plate in which each set of four colored squares corresponds to probes wired to the ground, V^+, V^-, and ref in decks in the switchbox, marked A, B, C, and D, respectively, for a particular device. The details of the wiring from these probes to the switchbox are outlined in FIG. 3-9(b).

(a)

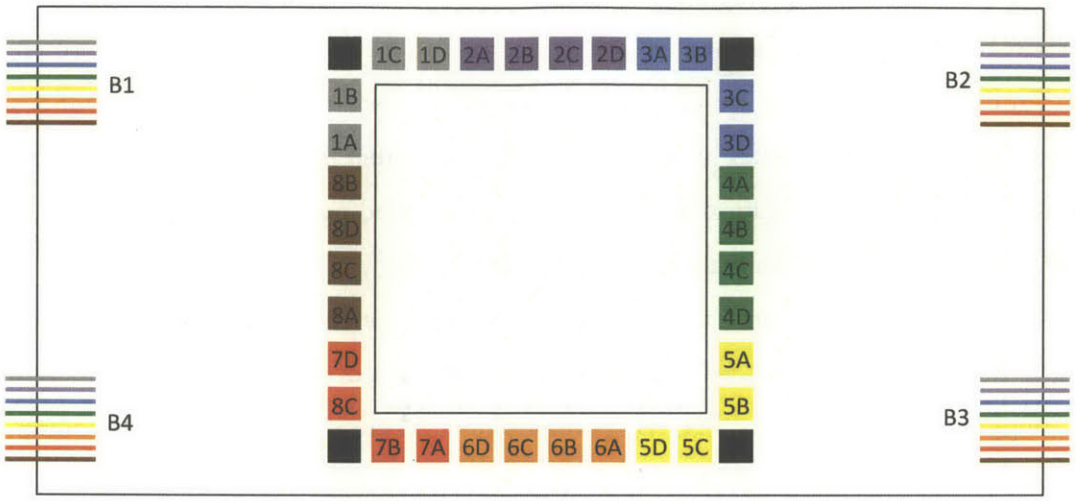

(b)

Device Pin	Bundle Wire	Device Pin	Bundle Wire
1A	B4-1	5A	B2-5
1B	B1-1	5B	B3-5
1C	B2-1	5C	B1-5
1D	B3-1	5D	B4-5
2A	B4-2	6A	B2-6
2B	B1-2	6B	B1-6
2C	B2-2	6C	B3-6
2D	B3-2	6D	B4-6
3A	B4-3	7A	B4-7
3B	B1-3	7B	B1-7
3C	B2-3	7C	B2-7
3D	B3-3	7D	B3-7
4A	B1-4	8A	B4-8
4B	B2-4	8B	B3-8
4C	B3-4	8C	B1-8
4D	B4-4	8D	B2-8

FIG. 3-9 Contact plate for electrical measurements

(a) Schematic top-down view of acrylic contact plate with 32 probes wired for four-point probe resistance measurement of up to 8 devices. Each set of four colored squares corresponds to the ground, V^+, V^-, and ref in, for a particular device, marked A, B, C, and D, respectively. Probes are positioned around the perimeter of a $1\times1\ in^2$ square cutout for optical access, and connect to a switchbox via 4 wire bundles (B1-B4). (b) List of and wiring associations between probes and wires in the bundles. Within each bundle, wires 1-8 correspond to the grey, purple, blue, green, yellow, orange, red, and brown wire, respectively.

3.3.6 Magneto-optic Kerr effect system

The magneto-optic Kerr effect (MOKE) is the observation that linearly polarized light experiences a rotation of its polarization angle upon interaction with magnetic material.

Because the extent of polarization rotation can be easily measured with comparatively inexpensive optical components, MOKE systems[121-123] have become popular tools for the characterization and study of magnetic materials. Indeed, the high temporal and spatial resolution of MOKE makes it a versatile technique that has been used to study such phenomena as DW propagation in thin films and patterned nanotracks[107], and magnetization switching behavior of individual magnetic elements[122,124].

MOKE can be configured to measure any of the three components of magnetization in a sample. As shown in FIG. 3-10(a), in-plane components of magnetization are measured in the longitudinal or transverse MOKE configuration, whereas the perpendicular component is measured in the polar MOKE configuration. In all cases, the principle is the same. Incident polarized light is reflected from a magnetic sample, resulting in a rotation of the axis of polarization that is proportional to the magnetization of the sample. In FIG. 3-10(b), it is shown how this can be used to obtain a hysteresis loop for a magnetic element. With the applied field causing the magnetization to point into or out of the page, the axis of polarization rotates clockwise or counterclockwise, respectively, an angle that is proportional to the magnitude of the magnetization. This main components required to measure such an effect are shown schematically in FIG. 3-10(c). A source of coherent light e.g. a laser is directed at a sample mounted in the active area of an electromagnet. Before hitting the sample, the beam is passed through a polarizer such that the light hitting the sample is linearly polarized along a known direction. Let this direction be E_p. After the sample, the light is passed through another polarizer set at an angle $0° < \theta < 90°$ to the first polarizer. The light intensity I measured by the photodiode is then of the form[121]

$$I \approx E_s^2 \left(\theta + \frac{1}{\tan \phi_k}\right)^2, \tag{27}$$

from which the Kerr rotation angle ϕ_k, due to interaction with the magnetic sample, can be obtained.

We have built a custom high-resolution scanning MOKE system that can be operated in either polar or longitudinal MOKE configurations. In this work, the longitudinal MOKE system was used as a probe of both bead motion (via reflected light intensity) and DW motion (via Kerr rotation) along sample magnetic structures.

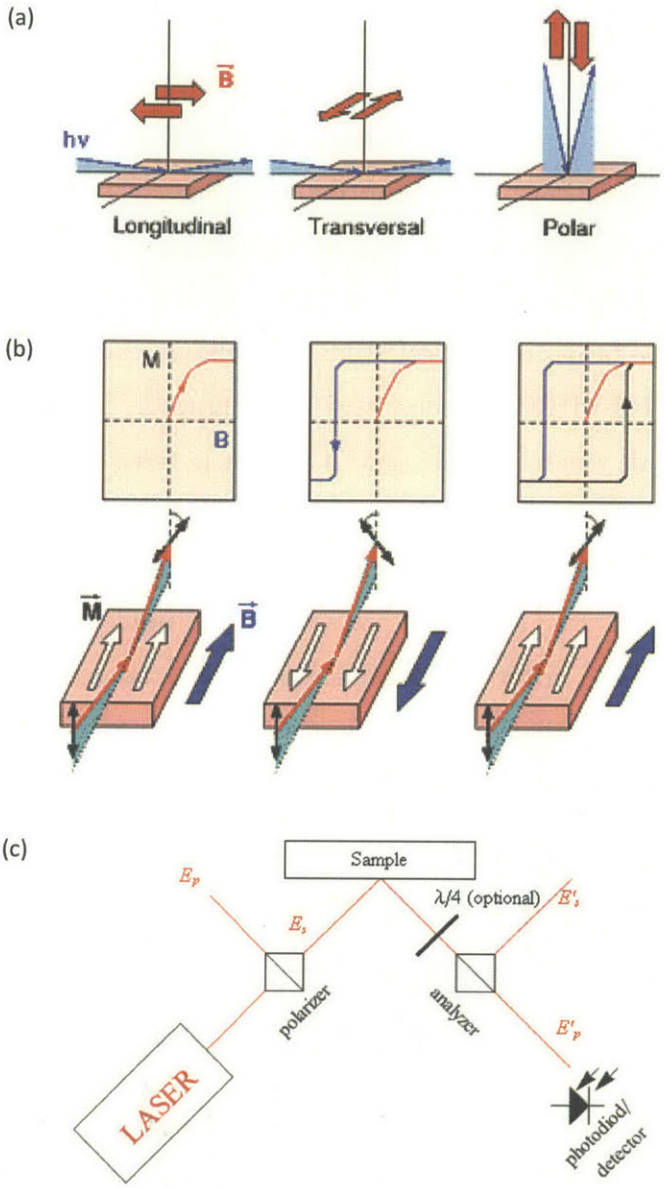

FIG. 3-10 Magneto-optic Kerr effect (MOKE)

(a) The three modes of MOKE, with sensitivity to either the in-plane longitudinal or transverse, or the out-of-plane component of magnetization. (b) Schematic depiction of the use of MOKE to obtain a hysteresis loop. (a-b) Adapted from http://www.fmc.uam.es/lasuam/glossary.php#moke. (c) Schematic of a typical MOKE setup. Adapted from http://en.wikipedia.org/wiki/File:Setup_Magneto-Optic-Kerr-Effect_A.png.

3.3.7 Optical detection with LabVIEW

The motion of individual trapped beads carried by field-driven DWs was programmed and tracked by a custom set-up, shown schematically in FIG. 3-11. During field rotation, the current amplitude and frequency supplied to the two channels of the vector electromagnet (Section 3.3.4) was modulated with a custom two-channel quadrature rotation box[138] while field information was passed to the custom LabVIEW program. For dc vector fields, specific low-frequency rotating fields, or vertical fields with the accessory air coil electromagnet (Section 3.3.4), the LabVIEW program was used instead. The dynamic response of individual trapped beads was tracked using a CCD camera fitted to a long working distance imaging microscope objective (Mitutoyo 10x M Plan APO) integrated with the LabVIEW program. The program allows for the definition of zero or more regions of interest (ROIs). Coupled with integration over ROI pixel greyscale values, bead passage through ROIs can be monitored in real time. Information obtained via ROI bead tracking can be used to trigger events such as vertical field application (Section 6.4) and track the direction and velocity of bead motion (Chapter 5 and Chapter 6).

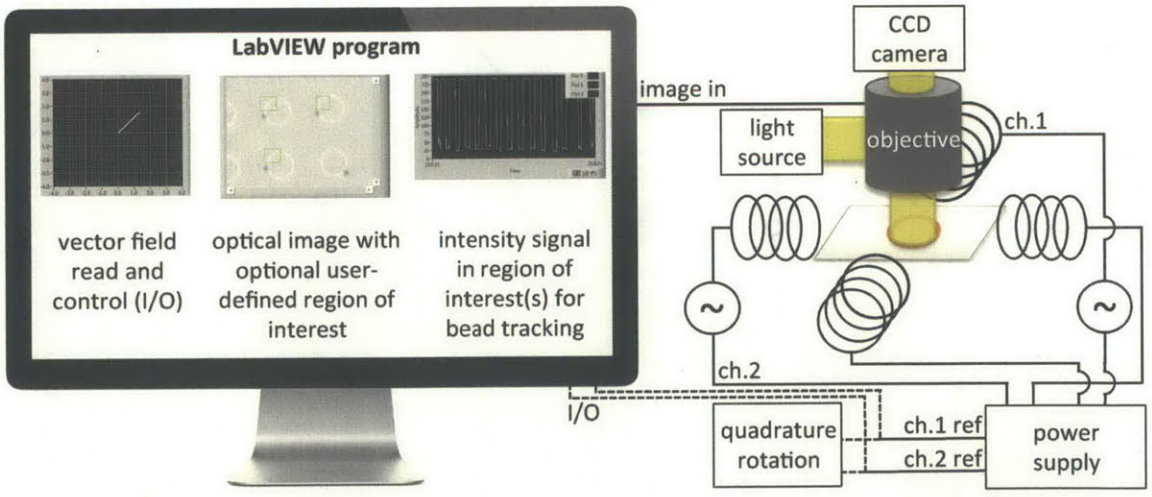

FIG. 3-11 Optical detection with LabVIEW

Schematic of optical detection setup consisting of vector electromagnet and power supply, microscope with camera, and custom LabVIEW program. Magnet is optionally driven by either a custom quadrature rotation drive box, LabVIEW program, or function generator (not shown). Quadrature rotation drive box designed and built by D. Bono.

Chapter 4

Numerical Studies of Interactions in the Bead-domain wall system[1]

In Section 2.2 we introduced the concept of magnetic domain walls and described the ways in which such entities can be driven along and positioned in arbitrary magnetic tracks by e.g. magnetic fields. Here, we discuss the theoretical viability of using DWs as bead carriers, and show that, owing to their highly localized stray fields, magnetic domain walls in magnetic nanotracks should be capable of shuttling superparamagnetic microbeads and magnetically tagged entities across the surface of a substrate.

The dynamics of such fluid-borne superparamagnetic bead transport by field-driven domain walls in submicrometer ferromagnetic tracks is studied with numerical and analytical modeling. We first carefully investigate the strength of interaction between a bead and DW. Although several estimates of the binding strength between a wall and trapped bead have been reported[36,43,81], these calculations have generally been limited to model parameters which do not accurately represent the size and magnetic state of the bead-DW system. In this work, we use a combination of micromagnetic modeling and numerical calculation (Section 3.1) to predict the strength of bead-domain wall interaction for experimentally relevant track geometries and bead sizes.

From the basis of these calculations, the maximum domain wall velocity for continuous bead transport through a viscous fluid is predicted. Furthermore, the effects of various parameters on such transport are investigated. In Section 5.1, we follow with experimental results that are found to agree with predictions made here.

[1] Sections of this chapter, including figures, have been previously published in Rapoport, E. & Beach, G. S. D. Transport dynamics of superparamagnetic microbeads trapped by mobile magnetic domain walls. *Phys. Rev. B* **87,** 174426 (2013). Reprinted with permission from *Physical Review B* **87,** 174426 (2013), Copyright 2013, American Physical Society. Available at http://dx.doi.org/10.1103/PhysRevB.87.174426.

4.1 Magnetostatic bead-domain-wall interaction

We consider a SPM bead proximate to a submicrometer-wide track of soft magnetic material. FIG. 4-1(a) shows the geometry of the modeled system. In such a track, the shape anisotropy forces magnetic domains to orient along the length, separated by DWs that generate high-gradient stray magnetic fields due to the strong divergence of DW magnetization.

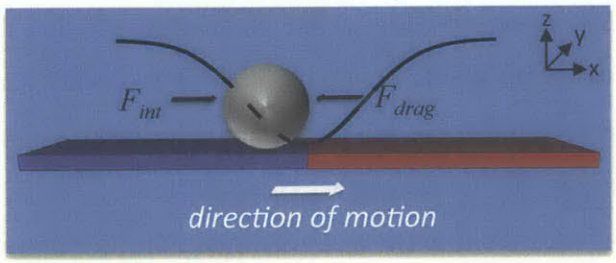

FIG. 4-1 Bead-DW system

Schematic of bead-DW interaction showing magnetostatic potential energy well and relevant forces during DW-mediated bead transport. Track generated by U. Bauer.

Bead capture occurs when the stray field of the DW induces a magnetic moment in the nearby SPM bead, creating an attractive magnetostatic potential well localized at the DW center. The bead-DW interaction force F_{int}, calculated from the energy gradient along the track direction as a function of bead-DW separation, draws the bead toward the DW. Once the bead is trapped in the potential well of the DW, the DW can be used to manipulate individual beads. Indeed, bead transport has been realized by either stepping a bead from one DW trap site to the next[35-38,40,42,43,100] or moving it continuously with a propagating DW[38,40,44,45,68,69]. Continuous transport is limited, however, by the viscous drag exerted on the bead as it is driven through the host fluid. As the DW moves, while F_{int} acts to keep the bead with the DW, the drag force displaces the bead from the DW center by an amount that increases the faster the pair move. The limit for continuous transport is thus set by the maximum interaction force, or binding force F_{bind}, between the bead and DW, which must overcome the hydrodynamic drag force F_{drag} on the bead as it is pulled through the host fluid[81].

In order to investigate the limits of continuous transport, following the methods described in Section 3.1, we have calculated the magnetostatic potential energy landscape and binding forces for SPM beads near a DW in a Permalloy nanotrack for a range of bead sizes and track dimensions. Track thicknesses were either 5 or 40 nm, with an OOMMF cell size of 5×5 nm^2 in the x-y plane.

We first considered the effect of DW structure on bead-DW interaction. Recall (Section 2.2.1) that, depending on the dimensions and material properties of a magnetic element, a DW can take a variety of forms. In the soft magnetic tracks considered here, magnetization rotation through the DW is forced in plane (Néel wall), and the DW takes one of two main geometries. In narrower, thinner tracks, transverse walls are favored, whereas in wider, thicker tracks, vortex walls are expected (Section 2.2.1). FIG. 4-2(a) and FIG. 4-2(b) show the top-down view of the spin configuration in the x-y plane of a head-to-head transverse and vortex DW, respectively, in a 200 nm wide, 5 nm thick Permalloy track. In a track of these dimensions, either a transverse or vortex wall could be observed [FIG. 2-4(c)], so a direct comparison of the two DW topologies on bead-DW interaction can be made.

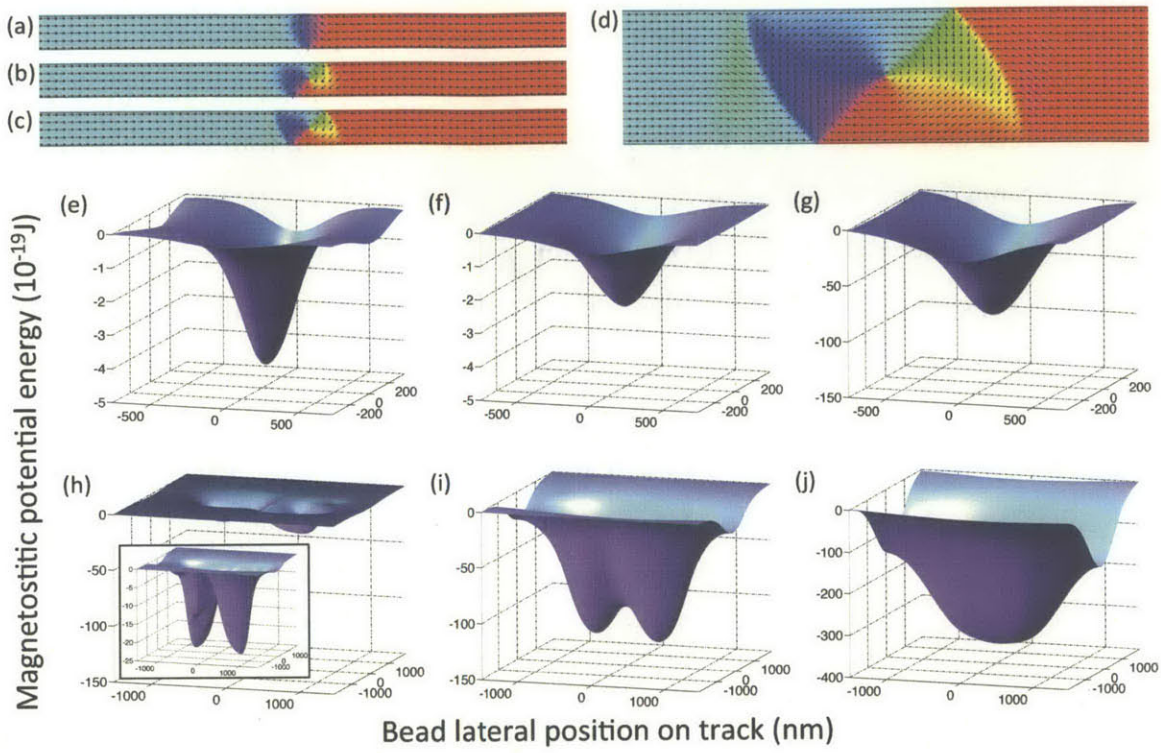

FIG. 4-2 DW topography and bead-DW energetics

(a-d) Micromagnetically calculated DW topology as a function of width and thickness in a Permalloy track, with (a) transverse wall in 200 nm wide, 5 nm thick track; (b) vortex wall in 200 nm wide, 5 nm thick track; (c) vortex wall in 200 nm wide, 40 nm thick track; and (d) vortex wall in 800 nm wide, 40 nm thick track. (e-j) Magnetostatic potential energy surfaces for a (e) 1.0 μm diameter bead over track (a); (f) 1.0 μm diameter bead over track (b); (g) 1.0 μm diameter bead over track (c); (h) 350 nm diameter bead over track (d); (i) 1.0 μm diameter bead over track (d); (j) 2.8 μm diameter bead over track (d).

The two wall structures exhibit different stray field profiles, which manifests as a difference in the strength of magnetostatic interaction with a SPM bead. This difference is shown in FIG. 4-2(e) and FIG. 4-2(f), which show energy surfaces for a 1 μm diameter bead over a transverse and vortex wall, respectively, in a in a 200 nm wide, 5 nm thick Permalloy track. For the same bead and track dimensions, the effect of DW topology on the magnetostatic potential energy surface is clearly visible. The potential well is deeper, and thus the binding force is greater, for a bead over a transverse wall than for a bead over a vortex wall. In terms of stray field energy density, the transverse structure is clearly preferred.

In order to increase the strength of interaction, thicker tracks i.e. ones with more magnetic material would be used, but the transverse structure cannot be maintained over a wide range of thicknesses[113,115]. However, as shown in FIG. 4-2(b) and FIG. 4-2(c), the

vortex wall structure is only marginally affected by an increase in track thickness. Moreover, despite having a lower stray field energy density, vortex walls in sufficiently thick tracks exhibit a total stray field energy that is greater than that of a transverse wall in a thinner track. FIG. 4-2(g) shows the magnetostatic potential energy surface for a 1 μm diameter bead over a vortex wall in 200 nm wide, 40 nm thick Permalloy track. Compared to that of FIG. 4-2(f), the well in FIG. 4-2(g) has approximately the same spatial extent but is more than 20 times deeper. This corresponds to about a 20-fold increase in binding strength [FIG. 4-3(a)]. This large increase in binding force is a result of the quadratic dependence of bead energy on stray field strength. Both the gradient field and the induced moment of the bead scale with the stray field amplitude, which in turn scale with the track thickness. Because the stray field scales linearly with the thickness of the track in this range, in this case, the binding force should increase approximately $8^2 = 64$ times between a 5 and 40 nm thick track. However, because of saturation effects in the bead, only a 25- to 30-fold increase in binding force is predicted.

Track width and bead diameter also have an effect on the magnetostatic energy well profile. FIG. 4-2(d) shows a vortex wall in an 800 nm wide, 40 nm thick Permalloy track. The vortex structure is maintained as compared to that of FIG. 4-2(c), but in agreement with prior work[115] showing DW width proportional to track dimensions, its spatial extent is about 4 times greater. Because the DW in a wider track is larger, for the same size bead, the potential landscape is more sensitive to local DW stray field variation. Where a larger bead averages out field variation, a smaller bead becomes a probe of the local DW stray field profile, giving physical insight into the field configuration. FIG. 4-2(i) shows the potential landscape for a 1.0 μm diameter bead over the DW in FIG. 4-2(d). Two local minima are now visible, compared to the one in FIG. 4-2(g). These local minima become even more distinct at smaller bead sizes. In FIG. 4-2(h), a 350 nm diameter bead probes the DW stray field profile, and in addition to the appearance of fine surface features that reflect the local stray field profile [FIG. 4-2(h, inset)], the reduced overall well depth, compared to that of FIG. 4-2(i), is also seen. This corresponds to a decrease in magnetic moment due to the decreased bead size. In contrast, for a larger 2.8 μm diameter bead over the same vortex wall of FIG. 4-2(d), the well is both deeper and more smoothed out [FIG. 4-2(j)].

In the section that follows, we put the attractive interaction between bead and DW, visualized here in terms of magnetostatic potential energy surfaces, in the context of bead transport.

4.2 Variables for bead transport

Binding strengths between beads and DWs were calculated from magnetostatic potential energy surfaces. FIG. 4-3(a) shows binding strength as a function of bead diameter, for beads with diameter $D = 2R$ spanning 100 nm to 2 μ m, over seven track-DW configurations. F_{bind} increases with D up to $D \sim 800$ nm, then saturates as the stray field falls off with distance from the track. The effect of increasing track thickness on binding force is seen as a greater than order of magnitude increase in F_{bind} for beads over vortex walls in 200 wide tracks, and a less dramatic but still significant variation in F_{bind} with track width is also seen. An optimal track width is observed, which reflects the tradeoff in increased stray field energy due to a larger DW, with the larger spatial extent of the stray field.

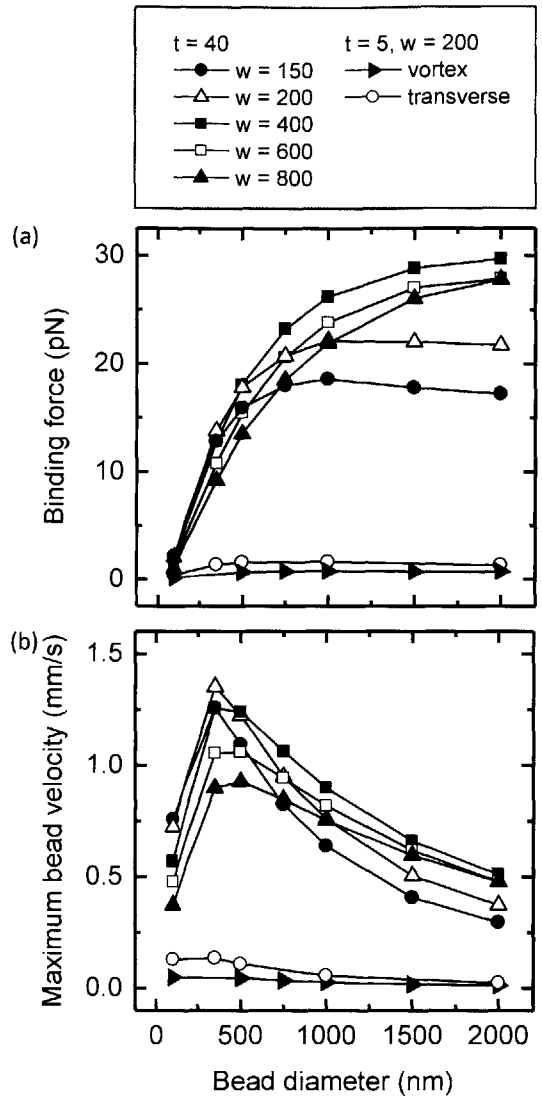

FIG. 4-3 Binding forces and maximum velocities

(a) Calculated longitudinal magnetostatic binding force and (b) maximum coupled transport velocity versus bead diameter for several track dimensions and wall topologies.

Maximum coupled transport speeds v_{max} were estimated by equating F_{bind} with viscous drag F_{drag} assuming the modified Stoke's form [Eq. (22)] with a viscosity $\eta = 10^{-3}$ Pa s of water and a near surface correction factor [Eq. (21)] of $\xi = 3.1$ for a bead touching and moving parallel to a plane wall. As seen in FIG. 4-3(b), v_{max} increases rapidly with D until F_{bind} plateaus, then falls off as $\sim 1/D$ as viscous drag continues to increase. Over a wide range of D, transport speeds in the mm/s range are predicted.

Higher transport velocities can be achieved by increasing the strength of bead-DW interaction via bead or DW moment enhancement. Due to the primarily out-of-plane stray field from the DW, an additional externally applied homogeneous out-of-plane field H_z can be used to augment the moment of the bead[36]. Magnetostatic potential energy surfaces of a 1.0 μm diameter bead over the DW of FIG. 4-2(c) were calculated as a function of H_z and the longitudinal cross sections of these surfaces are shown in FIG. 4-4(a). As expected, the increased moment of the bead leads to a stronger bead-DW interaction in the form of a deepening well over the same spatial extent. Conversely, an applied field of reverse polarity can be used to decrease the strength of bead-DW interaction. A plot of the binding force calculated from these surfaces [FIG. 4-4(b)] shows a linear relationship between F_{bind} and out-of-plane field in a range in which the effect of field on the domain wall structure can be neglected. These data suggest that the application of a vertical field can be used to tune the maximum transport velocity of a given bead. Furthermore, a higher saturation magnetization track material, such as CoFe, would enhance the moment of the DW and thus increase bead-DW magnetostatic interaction and binding forces. Thus, application of an out-of-plane field or use of a higher M_S material can be used to increase maximum transport speeds.

In the next chapter, we present experimental results in support of theoretical predictions, and demonstrate the feasibility of bead transport by field-driven DWs.

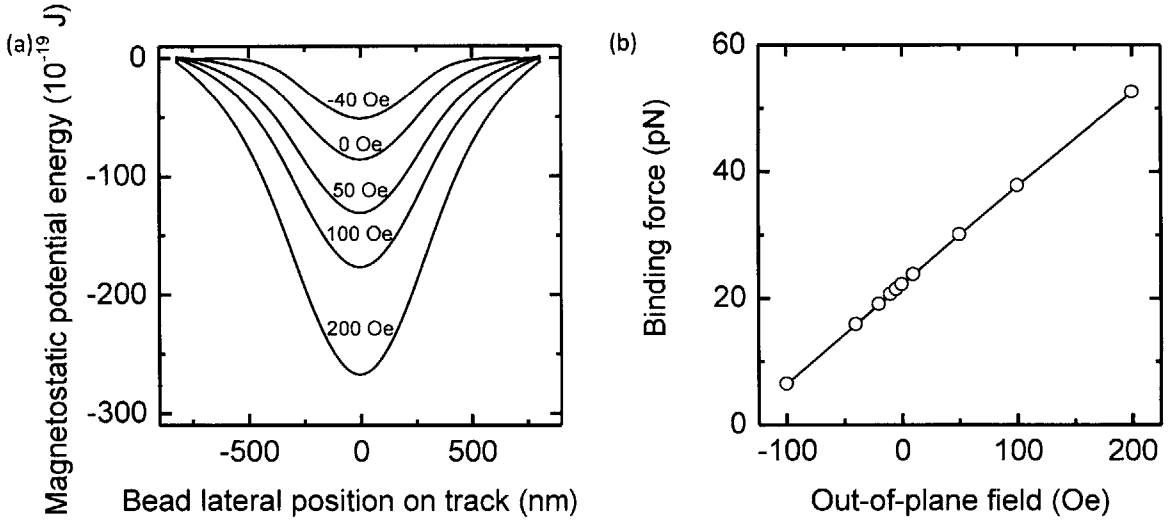

FIG. 4-4 Bead-DW energy and binding in vertical field

(a) Calculated cross-sectional profiles of magnetostatic potential energy wells and (b) longitudinal binding forces for a 1.0 μm diameter bead over a vortex wall in a 200 nm wide, 40 nm thick Permalloy track as a function of out-of-plane applied field.

Chapter 5

Domain-wall-driven bead transport dynamics[1]

In the previous chapter, we used a combination of micromagnetic modeling and numerical calculation to calculate magnetostatic potential energy wells and the strength of bead-DW interaction for a range of experimentally relevant track geometries, DW topologies, and bead sizes. Over a wide range of bead sizes and track geometries, we found the magnetostatic binding between a bead and a magnetic DW to be much stronger than had been expected[36,81], and theoretically capable of moving beads through viscous fluids at speeds on the order of mm/s. In this chapter, the dynamics of fluid-borne superparamagnetic bead transport by field-driven domain walls in submicrometer ferromagnetic tracks is studied experimentally.

This discussion is framed in the context of the three major features of the characteristic bead velocity versus DW velocity (VV) curve [FIG. 5-1]. Details regarding the generation and implications of the VV curve will be discussed extensively throughout the remainder of this chapter, but here it is important to note the main features: the low DW velocity (continuous transport) regime, the maximum bead velocity v_{max}, and the high DW velocity (knocking mode) regime.

[1] Sections of this chapter, including figures, have been previously published in Rapoport, E. & Beach, G. S. D. Dynamics of superparamagnetic microbead transport along magnetic nanotracks by magnetic domain walls. *Appl. Phys. Lett.* **100,** 082401 (2012) and Rapoport, E. & Beach, G. S. D. Transport dynamics of superparamagnetic microbeads trapped by mobile magnetic domain walls. *Phys. Rev. B* **87,** 174426 (2013). Reprinted with permission from *Applied Physics Letters* **100,** 082401 (2012), Copyright 2012, American Institute of Physics, and *Physical Review B* **87,** 174426 (2013), Copyright 2013, American Physical Society, respectively. Available at http://dx.doi.org/10.1063/1.3684972 and http://dx.doi.org/10.1103/PhysRevB.87.174426, respectively.

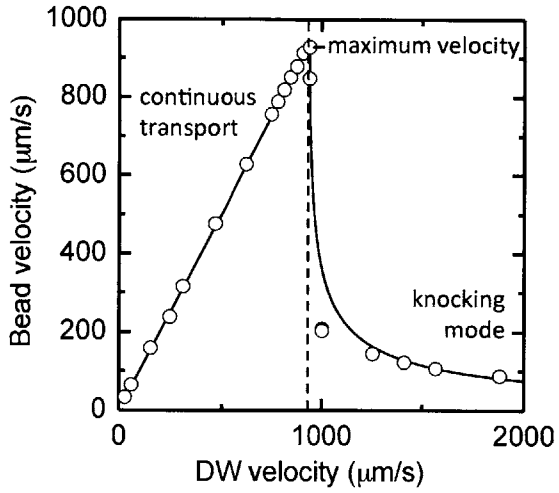

FIG. 5-1 Characteristic bead velocity versus DW velocity (VV) curve

Bead velocity versus DW velocity for a 1.0 μm diameter bead over a 10 μm outer diameter, 800 nm wide, 40 nm thick Permalloy track.

In Section 5.1 we discuss the low domain wall velocity, or continuous transport, regime. First, we propose a means of realizing bead transport by DW motion. Field-driven DWs normally travel along straight tracks at 100s m/s [FIG. 2-5], too fast for bead transport through a fluid. Thus, to achieve bead transport in a real system, slower DWs are required. Using a prototype ring structure in which the speed of DWs can be easily controlled[116], we demonstrate that DW-mediated bead transport continuously coupled to DW motion is indeed possible.

In Section 5.2, we explore bead motion in the high DW velocity regime. Contrary to expectations, it is found that for DWs traveling above the maximum velocity for continuous bead transport, a second "knocking" mode is exhibited, in which a rapid train of fast DWs can propel a bead quasicontinuously along a track. The dynamics of this mode are characterized both numerically and experimentally, and the implication of these results toward DW-mediated bead transport along straight tracks is discussed.

Following these dynamics studies, we explore the limits of synchronous bead-DW motion in the continuous transport regime. Maximum bead transport velocities are presented, and subsequently shown capable of being enhanced by appropriate material selection or field application.

5.1 Continuous bead transport by field-driven DWs

In this section we discuss the details of bead transport in which a trapped bead continuously tracks a moving DW, and consequently, bead velocity matches DW velocity v_{DW}.

We experimentally characterized the dynamics of SPM bead transport through an aqueous medium using DWs confined to circular ferromagnetic tracks. In this geometry, a strong in-plane magnetic field can take the ring from a "vortex" magnetization state [FIG. 5-2(a, left)], in which there are no DWs, to a bi-domain "onion" state[62,125-129] [FIG. 5-2(a, right)], in which two circumferential domains are separated by DWs lying along the field axis. These DWs can then be repositioned or continuously driven around the track simply by rotating the field axis. A rotating field can thus be used to circulate DWs around a ring at a frequency, and thus a velocity, dictated by the frequency of field rotation. This makes slow DW motion, and thus bead transport, possible. In this arrangement, the field is transverse to the track, so little longitudinal magnetic force is exerted on the domain wall, which would otherwise cause the DW to accelerate along the track at high speeds.

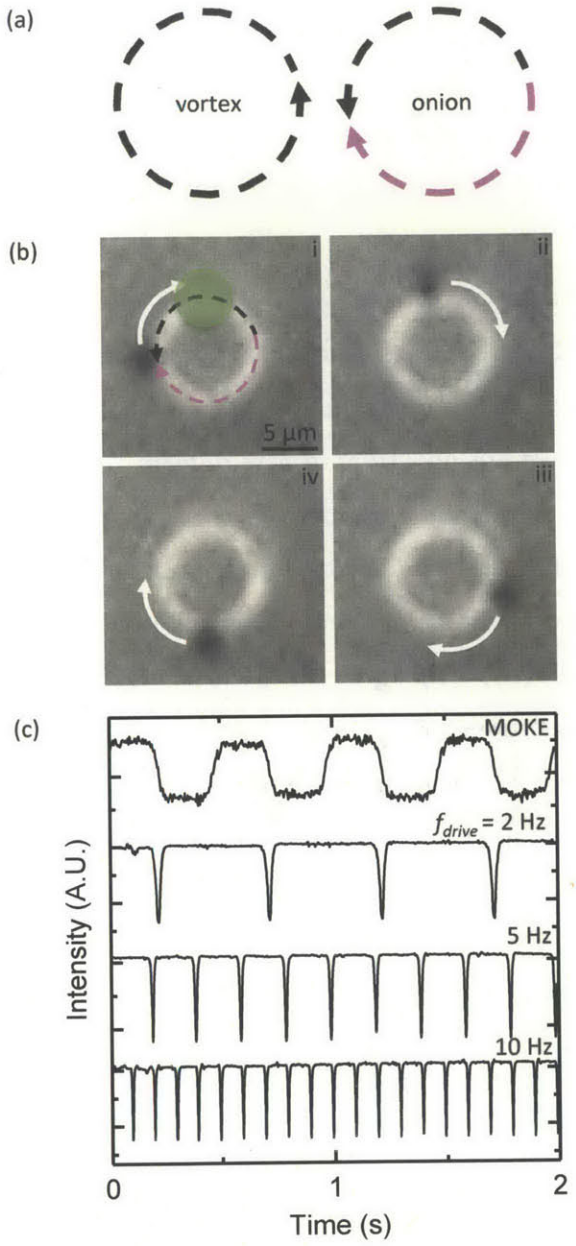

FIG. 5-2 Observation of synchronous bead-DW motion

(a) Two possible domain configurations in a magnetic ring. (b) (i-iv) Sequential snapshots of a 1.0 μm diameter bead driven around a 10 μm outer diameter, 800 nm wide, 40 nm thick Permalloy track by a 1 Hz clockwise rotating magnetic drive field. Domain orientation (dashed circle) and laser spot (solid circle) for optical reflectivity measurement shown schematically in image (i). (c) MOKE signal (top trace) at 2 Hz and optical reflectivity trace after bead capture at several drive frequencies.

Arrays of 800 nm wide, 40 nm thick, 10 μm outer diameter $Ni_{80}Fe_{20}$ tracks were fabricated on a Si wafer by electron beam lithography (Section 3.2.2), sputter deposition (Section 3.2.3), and liftoff (Section 3.2.4). After initializing the tracks into the bi-domain

state, a dilute suspension of 1.0 μm diameter MyOne SPM beads in phosphate buffered saline was placed on the wafer surface, as described in Section 3.3.3.

The sequential snapshots in FIG. 5-2(b, i-iv) show a single trapped bead driven around a track by a 1 Hz rotating field. The bead continuously followed the field axis with a direction and speed consistent with the sense and rate of field rotation, respectively. The CCD frame rate was sufficient to monitor bead motion up to a drive frequency f_{drive} of several Hz. At higher speeds, beads were tracked using a 352 nm solid-state laser probe, linearly polarized and attenuated to ~0.1 mW, and focused to a ~ 2 μm spot through the microscope objective. The probe spot was positioned at the track perimeter [FIG. 5-2(b, green spot)], where the reflected intensity was monitored in time. Bead traversal through the spot was accompanied by a momentary reflectivity dip. The laser probe also enabled direct detection of DW motion, via longitudinal MOKE (Section 3.3.6), upon insertion of a polarizer in the reflected beam path[107,121-123].

A MOKE signal trace acquired on the track in FIG. 5-2(b) under application of a 220 Oe, 2 Hz rotating field prior to bead capture is shown in FIG. 5-2(c, top trace). Each step in the trace represents a switch in the direction of tangential magnetization, due to passage of alternately head-to-head and tail-to-tail DWs, thus confirming the presence of DWs in the track. After bead capture, periodic reflectivity dips synchronous with DW circulation appeared [FIG. 5-2(c, second trace from top)], marking continuous bead transport as confirmed in simultaneous video imaging. The dip frequency tracked f_{drive} up to a limit of 19 Hz, corresponding to a maximum velocity of $v_{max} \approx 600$ μm/s.

Here it is important to recognize two main points. First, bead transport through a viscous fluid at a speed closely following numerical predictions [FIG. 4-3(b)] and far exceeding that of previous work is demonstrated. Indeed, speeds approaching 1 mm/s [FIG. 5-1] for a nominally identical bead-DW pair were observed. Second, by using a rotating field in conjunction with a curved track, DW speed is controlled, thereby realizing bead transport by, and synchronous with, these controlled DWs. The limits of this continuous transport are studied in more detail in Section 5.3.

In the next section, we study the behavior of beads driven by DWs traveling at speeds exceeding the limit for continuous transport and find, surprisingly, that a secondary mode of bead motion exists in this high DW velocity regime.

5.2 Slow bead motion by domain wall knocking

Recalling the bead from Section 5.1 [FIG. 5-2], we observed that the bead tracked DW motion up to a frequency of 19 Hz. Taking this as the maximum frequency f_{max} for which the bead could track the DW, it was expected that beyond this frequency, F_{bind} should overcome F_{drag} and consequently, the bead should no longer exhibit any motion. However, upon increase of the drive field frequency f_{drive} further, dips in the reflectivity trace could still be seen, albeit at a lower frequency than that of the drive field. This is seen in the reflectivity traces of FIG. 5-3(a). At $f_{drive} = 20$ Hz, dips were occasionally absent [FIG. 5-3(a, arrows)], indicating intermittent bead dropping by one DW and subsequent capture and carry by the other. For $f_{drive} = 21$ Hz, dropping and re-capture became regular with each revolution, evidenced by reflectivity dips at precisely half f_{drive}. At still higher f_{drive} the dip frequency fell precipitously, but regular bead circulation was sustained.

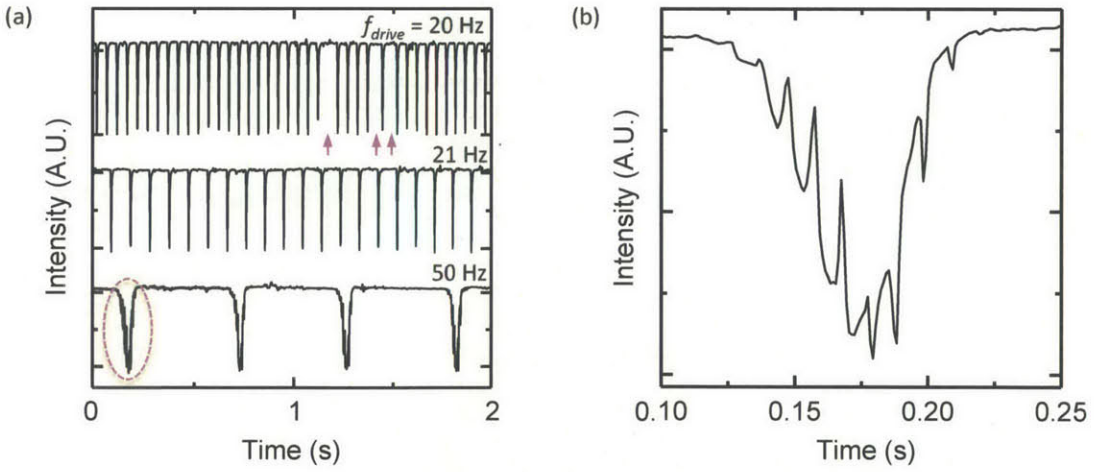

FIG. 5-3 Observation of bead motion in the knocking regime

(a) Optical reflectivity traces for a 1 μm diameter bead driven around a 10 μm outer diameter, 800 nm wide, 40 nm thick Permalloy track at several drive frequencies at which the bead cannot synchronously track with the DW. (b) Zoom of the circled intensity dip in (a) showing progressive oscillatory stepping of the bead through the laser spot by each passing DW.

Upon examination with video imaging, DWs under high f_{drive} showed continuous bead circulation in the direction of DW motion, at a decreased (with respect to f_{drive}), but finite

frequency. This motion suggested that the rapidly circulating DWs continually "knocked" the bead forward each time they passed, and that this knocking motion was responsible for the points in the high DW velocity regime of the VV curve [FIG. 5-1]. This theory was supported by closer inspection of one of the reflectivity dips in the 50 Hz trace [FIG. 5-3(a, dashed oval)]. The laser-probe technique employed permitted detection of sub-100 nm transient bead displacements with high time resolution, providing evidence for this fast DW-driven transport mechanism. Stepwise motion is visible in the high-f_{drive} reflectivity traces [FIG. 5-3(b)], which exhibit oscillations at $2f_{drive}$, commensurate with circulation of the two DWs. Upon entering the laser spot, forward (backward) bead displacement manifests as a decrease (increase) in reflected intensity. This correspondence is reversed as the bead emerges from the other side of the spot.

To explain this observation, we proposed the following model of bead-DW interaction in the high-v_{DW} regime [FIG. 5-4(a)]. As a DW approaches the bead, it pulls the bead abruptly back, resulting in a short negative bead displacement. After its initial backward motion into the potential well, the trapped bead travels with the propagating DW until it is eventually ripped out of the well by viscous drag that exceeds the bead-DW binding force. This longer forward travel results in overall forward displacement of the bead due to its interaction with the passing DW. A rapid train of DWs could thus propel a bead along a track even if their speed exceeds v_{max}.

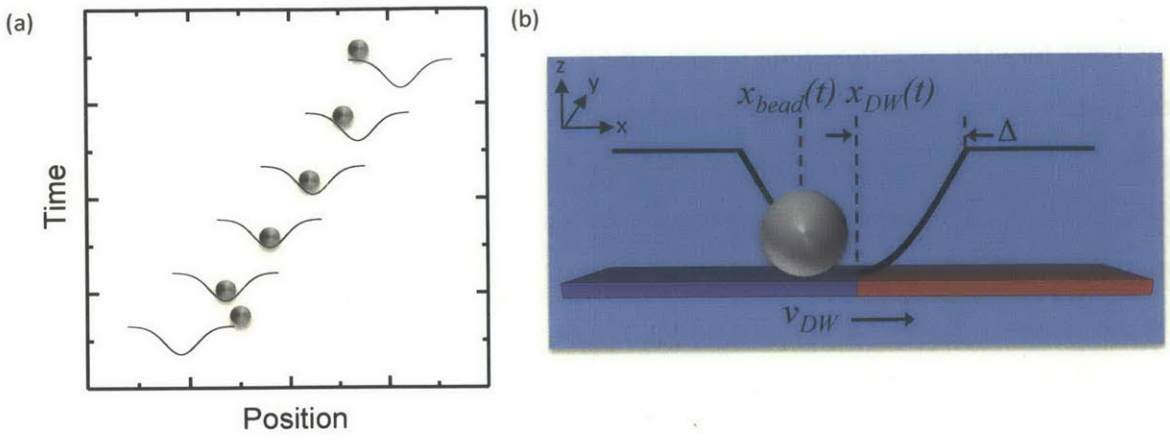

FIG. 5-4 Model for bead-DW interaction in high DW velocity regime

(a) Schematic of bead-DW interaction in the high DW velocity regime. (b) Schematic of model bead-DW system, with truncated potential well of half width Δ. Track generated by U. Bauer.

We analytically model this response of a bead to a passing DW in a circular track of radius R. The analysis is limited to the x-axis i.e. the axis of motion, because no forces act on the bead in the transverse (y) or, in our simplified model, in the z direction. The DW magnetostatic potential energy surface is approximated as a truncated parabolic well with half width Δ, and $x_{DW}(t)$ and $x_{bead}(t)$ are defined as the position of the well and bead as a function of time, respectively [FIG. 5-4(b)].

When the DW approaches the bead, it interacts with the bead via the restoring interaction force,

$$F_{int} = k(x_{DW}(t) - x_{bead}(t)), \tag{28}$$

with restoring force constant k. As the bead is forced though the liquid by the DW, it also experiences a strong counteracting damping force from the hydrodynamic drag, which can be written as

$$F_{drag} = -b\frac{dx_{bead}(t)}{dt}, \tag{29}$$

where $b = 6\pi\eta\xi r$ is the composite drag coefficient (Section 2.3.3). Letting time $t = 0$ be when the well first begins interacting with the bead (placed at the origin) such that $x_{bead}(0) = 0$ and $x_{DW}(0) = -\Delta$, and taking an equilibrium approximation of the bead and approaching DW, we can describe the interaction with the following force balance equation:

$$0 = k\left(v_{DW}t - \Delta - x_{bead}(t)\right) - b\frac{dx_{bead}(t)}{dt}, \tag{30}$$

where v_{DW} is the DW velocity. This expression can then be solved for $x_{bead}(t)$ to get the following:

$$x_{bead}(t) = v_{DW}t - \Delta - \frac{bv_{DW}}{k} + \frac{k\Delta + bv_{DW}}{k} e^{\frac{-kt}{b}}. \quad (31)$$

Eq. (31) gives the position of a bead interacting with an approaching DW as a function of time. Thus, bead displacement δ due to a passing DW can be expressed as $\delta = x_{bead}(\tau_{int})$, where the interaction time, τ_{int} can be written as

$$\tau_{int} = \frac{2\Delta + \delta}{v_{DW}}. \quad (32)$$

Recognizing that the bead is traveling at its maximum velocity $v_{max} = \frac{k\Delta}{b}$ just before it comes out of the well, we can solve for δ:

$$\delta = -\Delta(2 + \frac{v_{DW}}{v_{max}} \ln(\frac{v_{DW} - v_{max}}{v_{DW} + v_{max}})). \quad (33)$$

To express the bead transport velocity in terms of the DW velocity, we recognize that

$$\delta = \frac{v_{bead}}{(\frac{v_{DW}}{\pi R})}, \quad (34)$$

such that the average bead velocity in the high-v_{DW} regime is given as:

$$v_{bead} = -\frac{v_{DW}\Delta}{\pi R}(2 + \frac{v_{DW}}{v_{max}} \ln(\frac{v_{DW} - v_{max}}{v_{DW} + v_{max}})). \quad (35)$$

In agreement with observation [FIG. 5-1] the model predicts finite bead velocities even when $v_{DW} > v_{max}$. Furthermore, using Eq. (31), we can plot the expected trajectory for a bead interacting with a DW in the high-v_{DW} regime. FIG. 5-5(a) shows several simulated trajectories of a 2.8 μm diameter bead driven by a vortex DW in a 800 nm wide, 40 nm thick track at various f_{drive} corresponding to velocities above v_{max}. The k and Δ values used were obtained from the simulated potential energy well for this system [FIG. 4-2(j)] and b was taken assuming the viscosity of water and a ξ [Eq. (21)] value for a bead touching and moving parallel to a plane wall, as in Section 4.2. Each trajectory is characterized by a step-like behavior corresponding to the periodic displacement of a bead by passing DWs, as described in FIG. 5-4(a). A closer look at one of the steps [FIG. 5-5(a, inset)] shows the short backward displacement of a bead as it falls into the well of an approaching DW, followed by a longer forward travel before detachment from the traveling DW potential. Both the average step size per DW and bead velocity decrease with increasing DW frequency, as per Eq. (34) and Eq. (35), respectively.

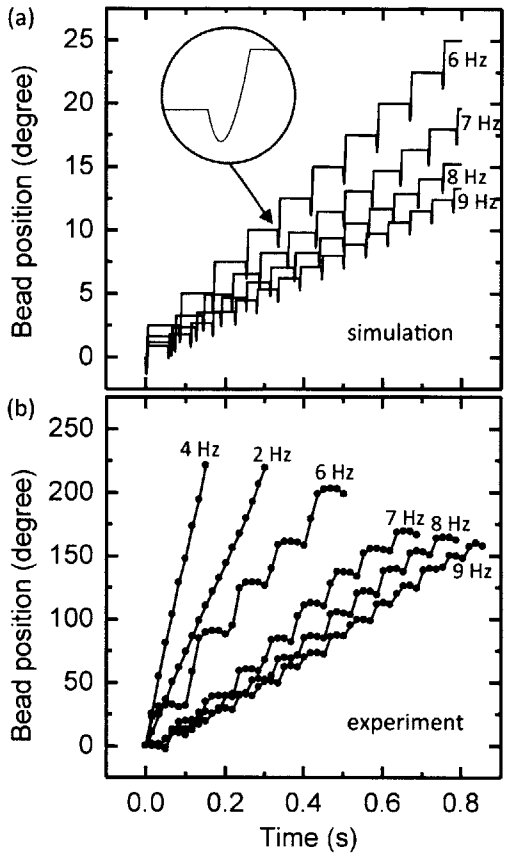

FIG. 5-5 Simulated and experimental bead trajectories in the high DW velocity regime

(a) Simulated and (b) experimental trajectories of bead motion due to DW-mediated transport as a function of drive field frequency. Simulation parameters correspond to those calculated for the experimental system. Experimental data shows trajectories for a 2.8 μm diameter bead driven by a DW in a 20 μm outer diameter, 800 nm wide, 40 nm thick Permalloy track at DW frequencies spanning the low and high DW velocity regimes.

These dynamics of bead motion due to passing DWs traveling faster than v_{max} were experimentally confirmed using the optical setup described in Section 3.3.7. Videos of bead motion at 60 fps taken at various f_{drive} were analyzed using a custom LabVIEW program that detected the particle and tracked its position over time. The main components of the video processing are shown in FIG. 5-6. For a given video input [FIG. 5-6(a)], two parallel views are generated by the application of different threshold parameters: one such that the bead is highlighted [FIG. 5-6(b)], and one such that the magnetic track is highlighted [FIG. 5-6(c)]. In each of these processed views, we select the objects to be tracked by defining a region of interest [FIG. 5-6(b-c, solid lines)]. To ensure that only absolute bead motion was tracked, wafer vibration was removed by subtracting the position of a stationary reference point e.g. the magnetic track [FIG. 5-6(c)] from that of the bead for each frame.

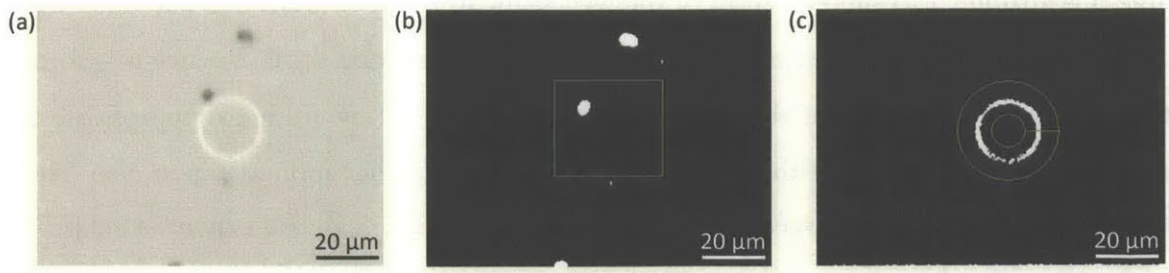

FIG. 5-6 Video analysis of bead trajectory

(a) Still taken from raw video of a 2.8 μm diameter bead driven around a circular track. (b-c) Threshold processing of image (a) with threshold such that only (b) beads or (c) magnetic track is highlighted. Only the motion of objects in the user-defined green regions of interest of (b) and (c) are tracked.

FIG. 5-5(b) shows the experimental trajectories of a 2.8 μm diameter M-270 bead driven by a DW in a 800 nm wide, 40 nm thick track at six different drive field frequencies spanning both the low and high DW velocity regimes. In the low DW velocity regime (below the maximum frequency for continuous bead transport $f_{max} = \frac{v_{max}}{2\pi R} \sim 4.5$ Hz), bead position around the ring changes linearly in time. An increase in drive field frequency also results in a corresponding increase in slope i.e. overall bead velocity v_{bead}. Above f_{max}, however, slope decreases with increasing f_{drive}, and periodic stepwise motion develops. That the step period is twice that of f_{drive}, commensurate with the circulation of the two DWs, and the features and trends of the trajectories closely match those of the simulated results, are evidence corroborating the model above.

A significant difference between the simulated and experimental trajectories is observed, however, in the time between DW passings. The simulated results exhibit plateaus between steps, suggesting that the bead sits stationary for some period of time between dislodgement from one DW and capture by the next. The experimental trajectories reveal a lack of such plateau behavior. This, along with observations of bead capture by DWs up to $\sim 10\,\mu$m away (Section 3.3.3), suggests that the tail of bead-DW interaction beyond the truncated well half-width is not insignificant.

The significance of the bead-DW interaction tail is also evidenced in the fit of Eq. (35) to the high-v_{DW} points of the VV curve of FIG. 5-1(a). The solid black line represents the fit, with fitting parameters $\Delta = 49\ \mu$m and $v_{max} = 227\ \mu$m/s. v_{max} is in relatively good agreement with the data and the fit curve qualitatively reproduces the experimental results. If compared to the potential well of FIG. 4-2(j), however, Δ is much larger than expected. This

large Δ is attributed to simplification of the well shape to that of a truncated parabolic well. Under this approximation, the tail of bead-DW interaction beyond the Δ distance is ignored. Thus, in fitting experimental results, unrealistically large Δ values are more appropriate to account for the effect from the bead-DW interaction tail. This approximation also likely explains the discrepancy between the scale in simulated [FIG. 5-5(a)] and experimental [FIG. 5-5(b)] trajectory data.

Finally, we investigated the bead displacement per DW as a function of drive field amplitude. As seen in FIG. 5-7, for a given field amplitude, bead displacement [Eq. (33)] decreases with increasing v_{DW} or f_{drive}, due to the decreasing interaction time of the bead with the wall. For a given f_{drive}, as the drive field amplitude is lowered, displacement per DW remains approximately constant till around the threshold field amplitude, below which it falls off. At the limit of very low drive field amplitude, displacement per DW appears to plateau on a constant value. AS will be seen, this trend is consistent with the data of FIG. 5-12(b), in which maximum velocity falls off below threshold due to increased DW pinning.

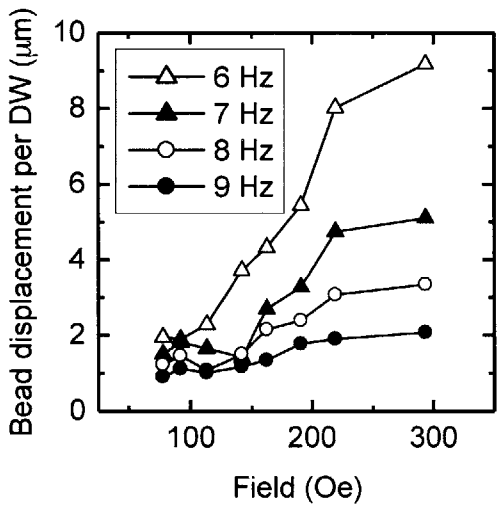

FIG. 5-7 Bead displacement per DW in the high DW velocity regime

Displacement of a 2.8 μm diameter bead by a vortex wall traveling faster than the maximum velocity for continuous transport as a function of drive field amplitude for several drive field frequencies. DW in a 20 μm outer diameter, 800 nm wide, 40 nm thick Permalloy track.

5.3 Maximum bead velocity via continuous transport

In the previous two sections, we investigated the dynamics of bead transport in the continuous and knocking transport regimes. At the crossover between these two transport modes, the bead reaches the maximum velocity with which it can track continuously with a DW. Recalling the discussion of Section 4.2, we determined that this maximum velocity depends on the ratio of drag force on the bead to binding force between the bead and DW. From this discussion, we predicted maximum transport velocities in the mm/s range. We also posited that we should be able to tailor v_{max} by tuning F_{bind} via vertical field application or track material selection. We have already seen evidence of fast bead transport (Section 5.1). Here, we provide experimental support to the claim that v_{max} results from the balance of F_{bind} and F_{drag}, and should therefor be tunable.

To verify these predictions, maximum velocities were measured experimentally. In order to have fine control over the DW velocity, the circular ring geometry was again chosen for the magnetic tracks. Recall that in such structures, the DW velocity can be precisely clocked with a rotating field. Arrays of $Ni_{80}Fe_{20}$(40 nm)/Pt(2 nm) and Cu(2.5 nm)/$Co_{50}Fe_{50}$(40 nm)/Pt(2 nm) circular tracks were prepared by electron beam lithography (Section 3.2.2), dc sputtering (Section 3.2.3), and liftoff (Section 3.2.4). The Cu underlayer of the CoFe tracks was used to reduce the coercivity in the CoFe layer[130]. Each track was 800 nm wide and 20 μm in outer diameter. Experiments were performed using commercial M-270 beads.

Magnetic fields were applied using the custom magnet described in Section 3.3.4 and the dynamic response of individual trapped beads was tracked using the optical detection scheme described in Section 3.3.7. In the previous section, we investigated the motion of individual 1.0 μm diameter trapped beads by monitoring the reflected light intensity from a focused laser spot as the bead passed underneath the beam. Here, the LabVIEW ROI replaces the laser of previous work, and ROI pixel information substitutes reflected laser light intensity.

The image in FIG. 5-8(a) shows a single 2.8 μm diameter bead trapped by a DW in a circular Permalloy ring. An in-plane rotating field was used to drive the bead-DW pair around the ring, and the pair followed the field axis with a direction consistent with the sense of field rotation. With an ROI (typically ~5×5 mm^2) positioned on the track perimeter, and the CCD frame rate set at 70 frames per second (fps), pixel intensity in the ROI was monitored in time. Bead traversal through the ROI was accompanied by a dip in pixel intensity. Real time single-shot measurement of dip frequency, corresponding to bead frequency f_{bead} around the ring, was taken as f_{drive} was slowly ramped up to ~30 Hz. Taking the linear bead and DW velocity as $v_{bead} = 2\pi R f_{bead}$ and $v_{DW} = 2\pi R f_{drive}$, respectively, VV curves were plotted. With this technique, a maximum observable bead velocity of $\frac{2\pi R}{1/(frame\ rate)} \approx 4400\ \mu$ m/s could be measured. The results of velocity measurements taken under different conditions are shown in FIG. 5-8, FIG. 5-9, and FIG. 5-10.

FIG. 5-8(b) investigates the effect of bead size and compares a VV curve for a 2.8 μm diameter M-270 bead to that of a 1.0 μm diameter MyOne bead[44]. Both beads exhibit motion in the two transport regimes in their VV curves. At low DW velocities, there is a linear relationship between bead and DW velocity, whereas above v_{max}, bead velocity falls off precipitously with DW velocity. The difference in the two curves is due to the difference

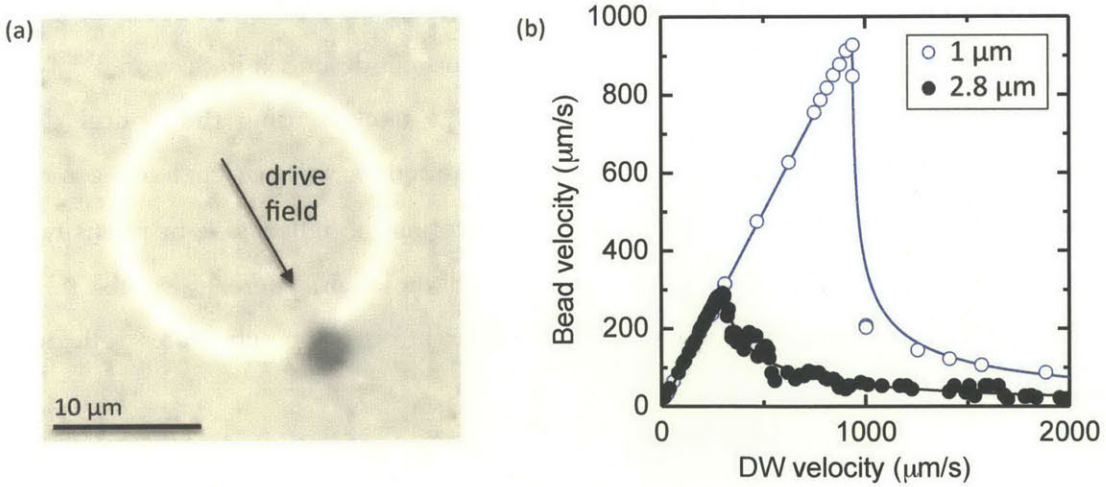

FIG. 5-8 Bead velocity versus DW velocity as function of bead size

(a) 2.8 μm diameter bead trapped by a DW in a circular 20 μm outer diameter, 800 nm wide, 40 nm thick Permalloy track. (b) Bead velocity versus DW velocity curves for beads driven by DWs in a 20 μm outer diameter, 800 nm wide, 40 nm thick Permalloy track as a function of bead diameter.

in bead size. From the calculations of binding force as a function of bead diameter [FIG. 4-3(a)], it is expected that these beads should have similar binding forces with the DW, and that their v_{max} should be approximately inversely proportional to their radii. Indeed this is observed, with the large and small beads reaching v_{max} of 290 and 925 μm/s, respectively, and provides a means to distinguish beads based on their size.

Next, out-of-plane fields were applied to increase the moment and thus the maximum velocities of beads, as per the discussion in Section 4.2. The VV curve of the same 2.8 μm diameter M-270 bead in zero and non-zero (H_z= 250 Oe) out-of-plane field [FIG. 5-9] shows a 2-fold enhancement of v_{max}. We can compare these results to those of FIG. 4-4(b), which show an approximately 3-fold increase in F_{bind} for a 1.0 μm diameter bead over a vortex wall in a 200 nm wide, 40 nm thick Permalloy track in a 250 Oe field. Since for a given size bead F_{drag} does not change with H_z, v_{max} should scale directly with F_{bind}. FIG. 4-4(b) thus predicts a 3-fold increase in v_{max} at this H_z, which is somewhat larger than the 2-fold increase observed experimentally. Since the slope of binding force vs. H_z is proportional to the susceptibility, the quantitative discrepancy can likely be attributed to a difference in the susceptibility of this bead compared to the value used in simulations. Despite quantitative differences, the experimental results are in good qualitative agreement with calculation, and show a clear maximum velocity enhancement by application of an out-of-plane field.

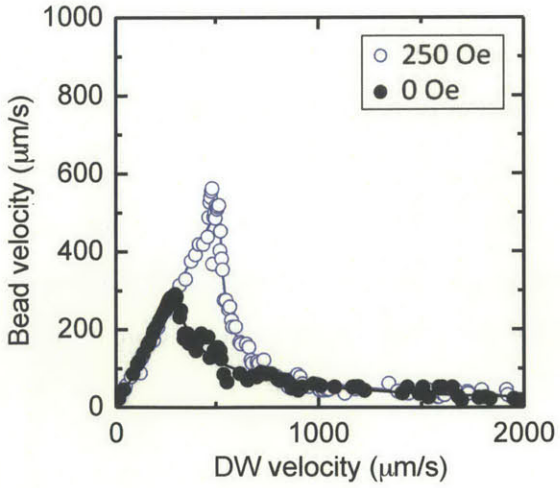

FIG. 5-9 Bead velocity versus DW velocity as function of vertical field

Bead velocity versus DW velocity curves for the same 2.8 μm bead over a 20 μm outer diameter, 800 nm wide, 40 nm thick Permalloy track as a function of vertical field.

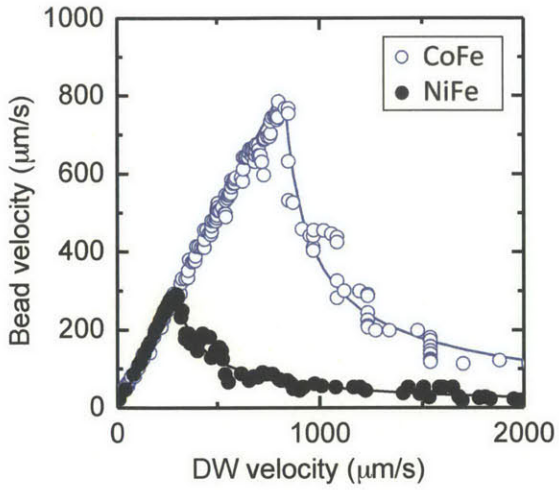

FIG. 5-10 Bead velocity versus DW velocity as function of track material

Bead velocity versus DW velocity curves for a 2.8 μm bead over a 20 μm outer diameter, 800 nm wide, 40 nm thick track of either NiFe or CoFe.

Finally, the effect of track material was investigated. As mentioned in Section 4.2, an increase in saturation magnetization of the track should result in a larger binding force. FIG. 5-10 plots the VV curves of two 2.8 μm diameter beads driven around CoFe (M_S=1910 kA m^{-1})[131] and NiFe (M_S=800 kA m^{-1})[81] rings of the same dimensions. The bead on the CoFe ring exhibits a v_{max} (785 mm/s) higher than that of the bead on the NiFe ring, proportional to the ratio of M_S between the two materials.

VV curves for 28 beads on CoFe and 30 on NiFe rings were measured and the maximum velocity distributions for these two populations can be seen in FIG. 5-11. The data show a narrow distribution for the beads on NiFe rings, centered on a mean at 273 μm/s with a standard deviation of 6 μm/s. For beads on CoFe rings, however, the average velocity is 539 μm/s with standard deviation 24 μm/s. The average upward shift in v_{max} is consistent with the data shown in FIG. 5-10, but the significantly larger standard deviation in v_{max} for these beads compared to that of beads over NiFe is unexpected given that the beads and surfaces used for both these measurements were nominally the same.

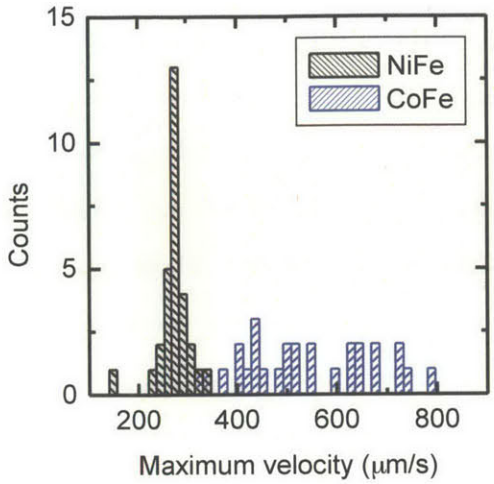

FIG. 5-11 Maximum velocity statistics as function of track material

Distribution of maximum transport velocities measured for 2.8 μm diameter beads driven by domain walls in 20 μm outer diameter, 800 nm wide, 40 nm thick NiFe and CoFe tracks.

The difference in standard deviation is understood through an analysis of maximum velocity versus drive field amplitude. This relationship reflects the influence of pinning on domain wall propagation around the rings. Hysteresis loops measured on continuous films exhibit coercivities of ~1 Oe for Permalloy and ~10 Oe for Cu/CoFe. Domain wall pinning due to lithographic defects in the patterned rings is likewise expected to be larger in the CoFe rings than in the Permalloy rings. As DWs are driven around the tracks, they encounter lithographically induced defects. The magnetostatic stray fields in the vicinity of such defects create local potentials that act as pinning sites for DWs[116,117]. Given that the stray field strength scales with the track material M_s, for the same landscape, a DW should experience stronger pinning in a higher M_s material track. It follows that a DW will encounter stronger pinning sites as it is driven around a CoFe track than around a NiFe one, such that larger drive field amplitudes will be necessary to move DWs smoothly through the former than the latter. Below the threshold field for smooth DW motion, DWs exhibit jagged motion. The DW is repeatedly pinned by defects and subsequently depinned by the increasing tangential component of field as the lag between the field axis and DW position increases. During depinning, as the DW accelerates to overcome the lag between the DW and field axis, the instantaneous linear velocity of the DW is greater than that of the field axis. For sufficiently large lags, the instantaneous DW velocity exceeds the maximum bead transport velocity, despite the average DW velocity being lower than v_{max}. Negoita et

al.[116,117] studied the motion of DWs in lithographically patterned NiFe rings of similar dimensions and found that the field-DW lag increases with both decreasing field amplitude and increasing field frequency. Thus, one should observe a decrease in maximum bead velocity with decreasing drive field amplitude below threshold.

The maximum velocity versus field curves for two 2.8 μm diameter beads over NiFe tracks [FIG. 5-12] are consistent with this analysis, showing a constant v_{max} above[139] and a decreasing v_{max} below threshold. Curves taken for two beads over CoFe tracks exhibit the same trend below threshold. Due to limitations of the electromagnet used in experiment, however, only field amplitudes below threshold for CoFe rings could be generated. As a result, while the 295 Oe field used to measure v_{max} for beads over both NiFe and CoFe rings is above threshold for NiFe, it is below for CoFe, such that the measured velocities were subject to the local pinning profiles of each circular track used. Thus, the insufficient field amplitude used to measure beads on CoFe rings is likely the cause of the wide distribution in v_{max} [FIG. 5-11].

It is clear from this discussion that the maximum transport speed of a bead by a field-driven DW is a function of several parameters, both material and processing. This knowledge gives us the tools both to optimize experimental velocities towards their

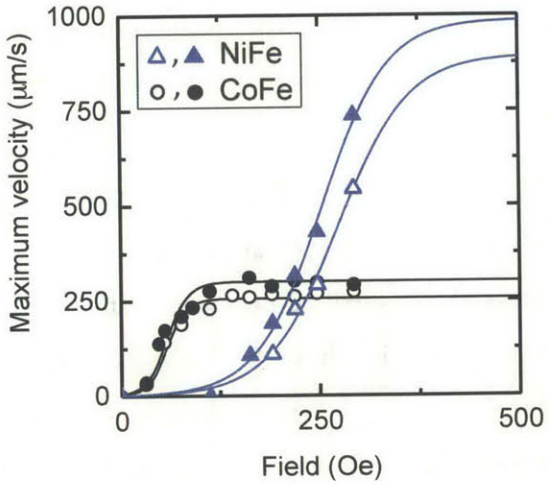

FIG. 5-12 Maximum bead velocity versus drive field amplitude

Maximum velocities for two 2.8 μm beads over each of 20 μm outer diameter, 800 nm wide, 40 nm thick NiFe and CoFe tracks as a function of applied field amplitude. Lines are meant as guides to the eye.

theoretical limit v_{max} (or in the case of linear transport, $\frac{2v_{max}}{\pi}$, taking into account geometrical considerations) and to tailor bead velocities for a given application.

5.4 Discussion

In this chapter, the transport dynamics of bead motion along circular tracks has been experimentally investigated. Using ring tracks, we demonstrated that bead motion synchronous with field-driven DWs is indeed possible. In this regime, the magnetic binding force holding the bead to the DW exceeds that of the hydrodynamic drag force that acts to separate the two. The use of DW as mobile trapping potential rather than stationary attractive element should be noted, as this subtle difference allows for the precision and speed of DW transport demonstrated here. Indeed, the high speeds reported open up the possibility of high-throughput microbead-based on-chip devices for sorting and sensing applications.

We also showed that DWs traveling faster than the limit for coupled transport remain capable of displacing a bead. The knocking transport mode has implications for moving beads along simpler geometries such as straightaways, where DWs travel much faster than v_{max}. Here, one could imagine a scheme whereby a train of high speed DWs periodically injected into a straight track at high frequency results in the net displacement of a bead. This, in addition to the added ability to tailor bead step size per passing DW by application of the appropriate field, is promising for fine bead positioning along tracks of arbitrary geometry.

In the next chapter, we discuss the extension of bead transport by field-driven DWs to more complicated tracks, thereby making bead routing along complex circuits possible.

Chapter 6

Programmable bead motion along a magnetic circuit[1]

Thus far, we have demonstrated the capability of DWs to capture beads and move them around ring tracks at tailored slow or fast speeds. However, in order to achieve the goals of lab-on-chip devices, extended transport along more complicated circuitry must be possible. In this chapter, we first show smooth transport along a curvilinear backbone consisting of linked semi-circular segments, proving the capability for long-distance linear bead transport at controlled speeds. Then, the transport capability of domain walls to move beads through a junction in such curvilinear tracks is investigated. Numerical and analytical modeling suggests that a vertically applied field of appropriate magnitude and sign can be used to select the direction of bead motion at a junction. Experiment on a population of nominally identical beads supports simulation data and reproducible bead behavior at a junction is achieved. Furthermore, this routing technique is also shown to be able to sort a mixed population of beads by simple application of a vertical field, thus advancing the realization of magnetic lab-on-chip devices.

6.1 Bead motion along a curvilinear backbone

DW-mediated bead transport is not limited to bead motion around a ring, and indeed we are able to realize fast bead transport over an extended distance. FIG. 6-1(a) shows a curvilinear track architecture composed of linked semi-circular segments, joined at tapered points to avoid DW nucleation[132-134]. As in the ring, in which each of the two DWs of the onion state [FIG. 5-2(a, right)] track the drive field vector, a rotating field controllably drives parallel DW motion in the curvilinear backbone. DWs progress along the track in tandem, moving from one segment to the next with each half cycle of the field. Beads trapped by DWs in the

[1] Sections of this chapter, including figures, have been previously published in Rapoport, E. & Beach, G. S. D. Dynamics of superparamagnetic microbead transport along magnetic nanotracks by magnetic domain walls. *Appl. Phys. Lett.* **100,** 082401 (2012). Reprinted with permission from *Applied Physics Letters* **100,** 082401 (2012), Copyright 2012, American Institute of Physics. Available at http://dx.doi.org/10.1063/1.3684972.

curvilinear backbone follow their motion. In FIG. 6-1(b) we demonstrated such motion, and translation speeds up to 150 μm/s were sustained as the bead was shuttled back and forth more than 200 times with no missteps, for a total travel distance of several cm. At higher speeds, the bead was intermittently trapped at the segment junctions, but junction optimization should enable higher translational speeds.

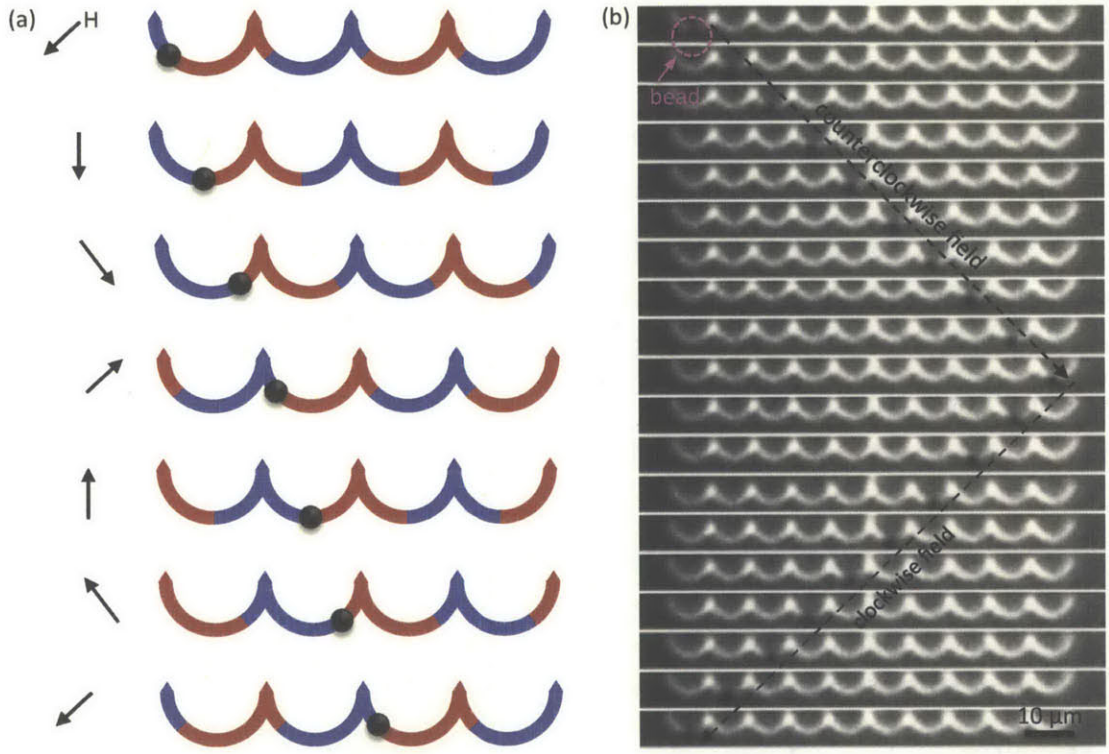

FIG. 6-1 Bead transport along curvilinear track

(a) Schematic representation of parallel DW motion through a curvilinear track in a rotating in-plane field. Parallel DWs move one circular segment every half-field rotation. Position of a bead driven by DW motion also indicated. (b) Sequential snapshots at 180° field rotation intervals show a trapped 1.0 μm diameter bead driven along a 10 μm outer diameter, 800 nm wide, 40 nm thick Permalloy curvilinear track. Counterclockwise and clockwise field rotation results in motion to the right and the left, respectively.

6.2 Junction geometries

In order to implement a change in direction with the curvilinear backbone necessary for bead transport, the junction must not introduce a discontinuity to the flow of rotating-field-driven DW motion. Consequently, a junction realized by a rotary-like structure is considered. FIG. 6-2(a-b) shows two possible rotary geometries in which an inlet diverges off into

several outlets. In both cases, a clockwise rotating field will drive a bead from the inlet to the rotary. Where the two differ is in the orientation of the outlets with respect to the inlet. If we define inbound and outbound as movement towards and away from the rotary, respectively, then we can characterize the motion as being driven either by a clockwise or counter-clockwise rotating field [FIG. 6-2(c)]. In the case of FIG. 6-2(a), once a bead is driven into the rotary by a clockwise rotating field, it will circulate within the rotary indefinitely until ejected by a counter-clockwise field, since all outbound motion is driven by a CCW field. This geometry can thus be considered sense-controlled. In the case of FIG. 6-2(b), however, a CW field will both drive a bead into the rotary, and direct its outbound motion along the outlets. Thus, at the approach of an outlet junction, the bead has two options: to continue around the rotary or to diverge off into the outlet. Which of these two options the bead takes is the focus of this chapter, and as we will see, is a function of vertical field. We begin the analysis in the next section with a discussion of the motion of a DW through such a vertical-field-controlled junction.

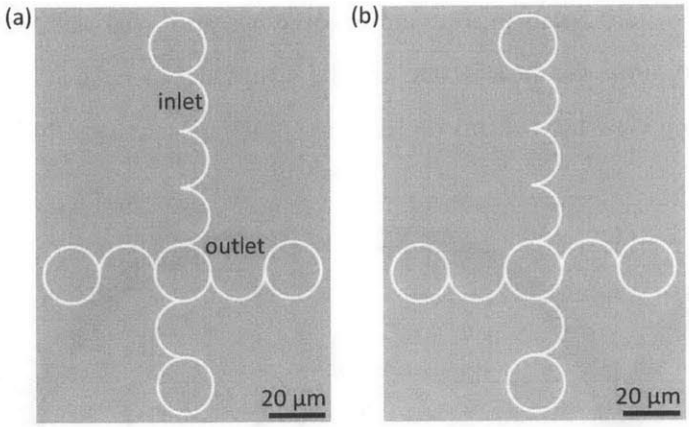

(c)

	Inlet	Outlet	
		(a)	(b)
Inbound	CW	CW	CCW
Oubound	CCW	CCW	CW

FIG. 6-2 Junction geometries

(a) Sense- and (b) vertical-field-controlled junction geometries. (c) Characterization of field rotation direction required for inbound and outbound motion along the inlets and outlets in the two junction geometries of (a) and (b).

6.3 Domain wall motion through a curvilinear junction

The motion of a DW through a field-controlled junction [FIG. 6-4(a, black square)] was first calculated micromagnetically using OOMMF (Section 3.1). A vortex DW was initialized in a model junction 100 nm wide, 60 nm thick, and with 2 μm outer diameter by letting the magnetization state shown in FIG. 6-3(a) relax under a 625 Oe bias field at 66.1°. The relaxed junction magnetization state [FIG. 6-3(b)] was then subjected to a rotating field of 625 Oe. In each simulation stage, the field angle was stepped 2 degrees, and the spin configuration in the strip was allowed to relax for the duration of the stage (5 nanoseconds).

The spin configuration in the junction as a function of rotating in-plane field is shown in FIG. 6-4(b-g). As the field is rotated in-plane, the initialized DW [FIG. 6-4(b)] begins to move in the direction of field rotation, tracking the field axis [FIG. 6-4(c)]. Upon entering the junction branch point, the DW becomes attracted and pinned to the local magnetostatic potential well created by the junction notch [FIG. 6-4(d)]. While pinned, the DW does not track with continued field rotation, but rather stretches and eventually splits into two DWs of opposite configuration i.e. head-to-head (H-H) and tail-to-tail (T-T) [FIG. 6-4(e)]. The resulting DWs, which now lag behind the field axis, then accelerate around the track to align

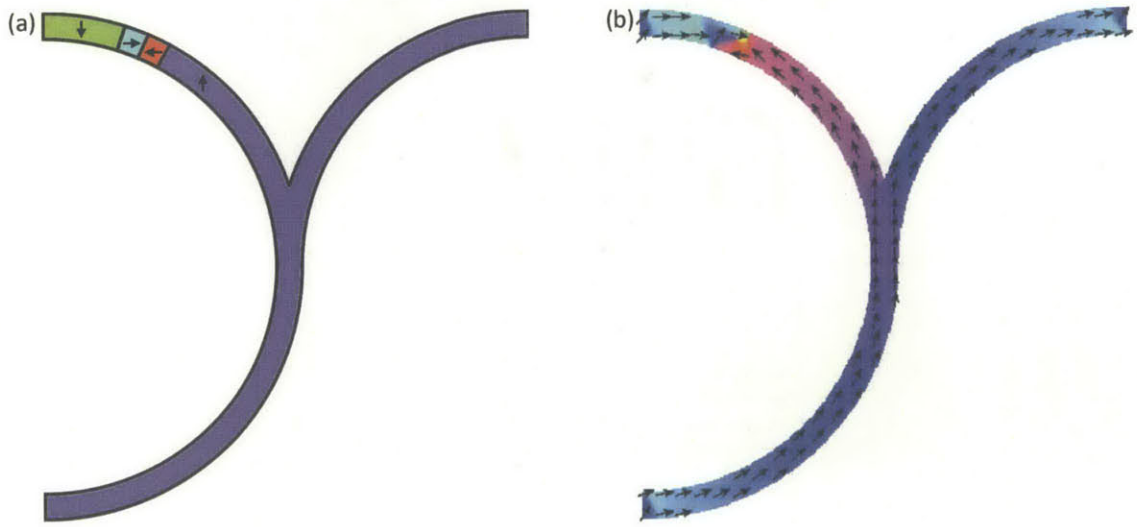

FIG. 6-3 Domain wall initialization in a junction for micromagnetic calculations

(a) Initial and (b) resulting micromagnetically-generated relaxed spin configuration for a vortex domain wall in a junction in a curvilinear track 60 nm thick, 100 nm wide, and with a 2 μm outer diameter.

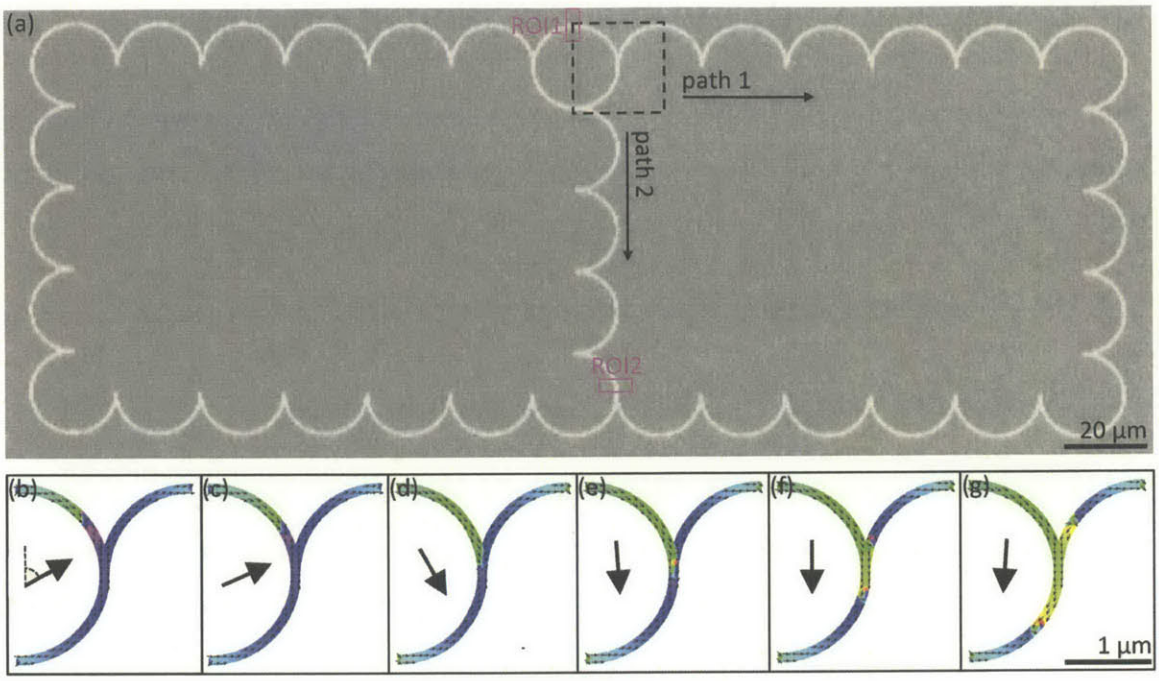

FIG. 6-4 DW motion through a field-controlled junction

(a) Optical image of branched 20 μm outer diameter, 800 nm wide, 40 nm thick curvilinear Permalloy track. Dashed square highlights micromagnetically simulated junction region. (b-g) Steps in micromagnetic simulation of magnetic configuration in dashed square region in part (a) in 2 μm outer diameter, 100 nm wide, 60 nm thick track as an externally applied in-plane field (arrow) is rotated in time. A single head-to-head DW enters the junction, and two DWs, one head-to-head and one tail-to-tail, exit. Two regions of interest (ROI1 and ROI2) are indicated.

with the field [FIG. 6-4(f-g)].

This single incoming DW splitting into two of opposite configuration creates an asymmetry in the system that can be exploited for selective bead motion. Recall that bead capture and transport occurs when the stray field of a DW induces a magnetic moment in a nearby bead, creating a magnetostatic potential energy well localized at the DW center. Here, both of the two DWs of opposite configuration exiting the junction can act as magnetostatic potential wells for a bead, yielding two possible paths for bead motion. However, the stray field above the two DWs is of opposite sign [FIG. 6-5(a)], and thus an externally applied vertical field can be used to strengthen the bead-DW interaction for one DW configuration, while simultaneously weakening the strength of interaction for the other. It is this asymmetry in bead interaction with DWs of opposite configuration upon application of a vertical field that will be used to direct bead motion at a junction. This will be the subject of Section 6.4.

6.4 Bead motion through a curvilinear junction

In this section, the use of vertical field to select the direction of bead motion at a junction is realized, not only to achieve the routing of a single bead, but also the sorting of a two-bead population.

6.4.1 Asymmetric bead interaction with domain walls of opposite configuration under vertical field

The effect of vertical field on bead interaction with the asymmetric DWs exiting a junction was investigated numerically. The track magnetization profile from a simulation stage at which two DWs are present in the junction was used to compute the stray field above the track via the method described in Section 3.1.

FIG. 6-5(b-d) show magnetostatic potential energy surfaces for a 300 nm diameter bead over a junction containing two DWs as a function of vertically applied field. In the absence of any vertical field [FIG. 6-5 (c)], the potential energy wells above the two DWs are nominally identical (excluding the contribution from the junction notch). However, with the application of a negative vertical field, which is simultaneously additive to the negative stray field above a T-T DW and subtractive to the positive field above a H-H DW, it is possible to selectively strengthen the interaction between a bead and a T-T DW over that of a H-H DW [FIG. 6-5(b)]. In the same manner, a positive vertical field can be used to preferentially select for a H-H DW over a T-T DW [FIG. 6-5(d)]. In fact, in strong enough vertical fields, one of the wells will invert, the beginning stages of which can be seen above the T-T DW in FIG. 6-5(d).

These results begin to suggest that a vertical field of appropriate sign can be used to impose bead preference for one DW over another and thus theoretically direct the motion of a bead at a junction. FIG. 6-6 elaborates on the results of FIG. 6-5 and shows the calculated junction energy landscape for a 300 nm diameter bead under rotating in-plane field and dc vertical field over time for three different vertical field amplitudes. In each case of FIG. 6-6(a-c), a H-H wall enters the junction and both a H-H and T-T wall exit. Under no vertical field [FIG. 6-6(b)], the bead is sensitive to the stray field of both exiting DWs, as is evidenced by the two potential wells. However, when either a negative or positive vertical

field is applied, the bead becomes sensitive to the stray field of only the T-T or H-H exiting DW, respectively.

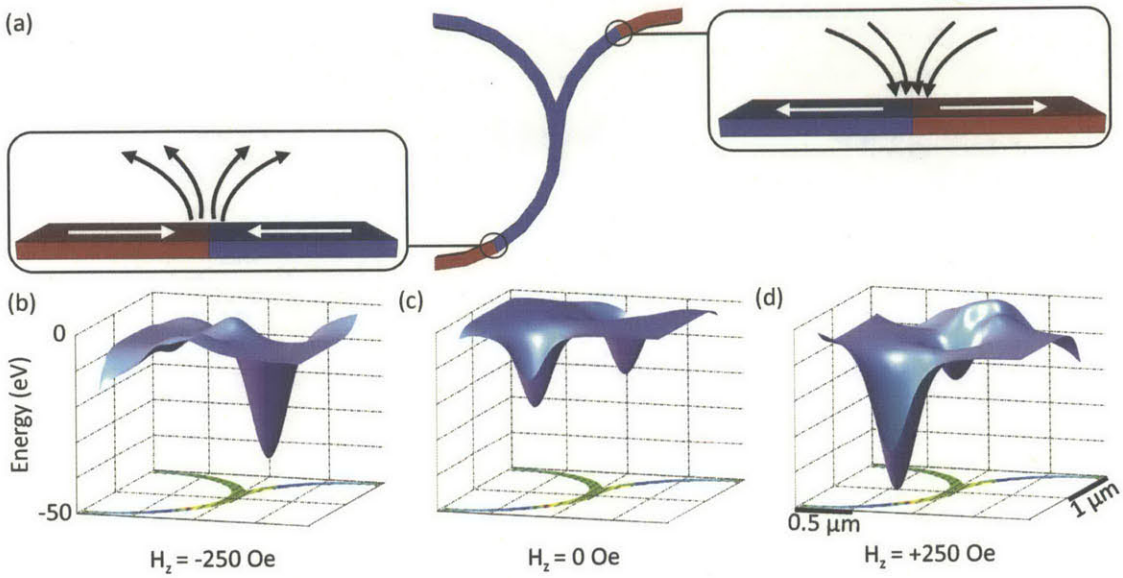

FIG. 6-5 Asymmetric interaction under vertical field

(a) Schematic of resulting DW configurations and associated stray fields after propagation of a single head-to-head DW through a curvilinear junction. Head-to-head (bottom left) and tail-to-tail (upper right) DWs yield positively and negatively oriented stray fields, respectively. Tracks generated by U. Bauer. (b-d) Calculated magnetostatic potential energy surfaces for a 300 nm diameter bead over a junction in a 2 μm outer diameter, 100 nm wide, 60 nm thick Permalloy track containing two opposite DWs, as in (a), in (b) -250 Oe, (c) 0 Oe, and (d) +250 Oe vertical field.

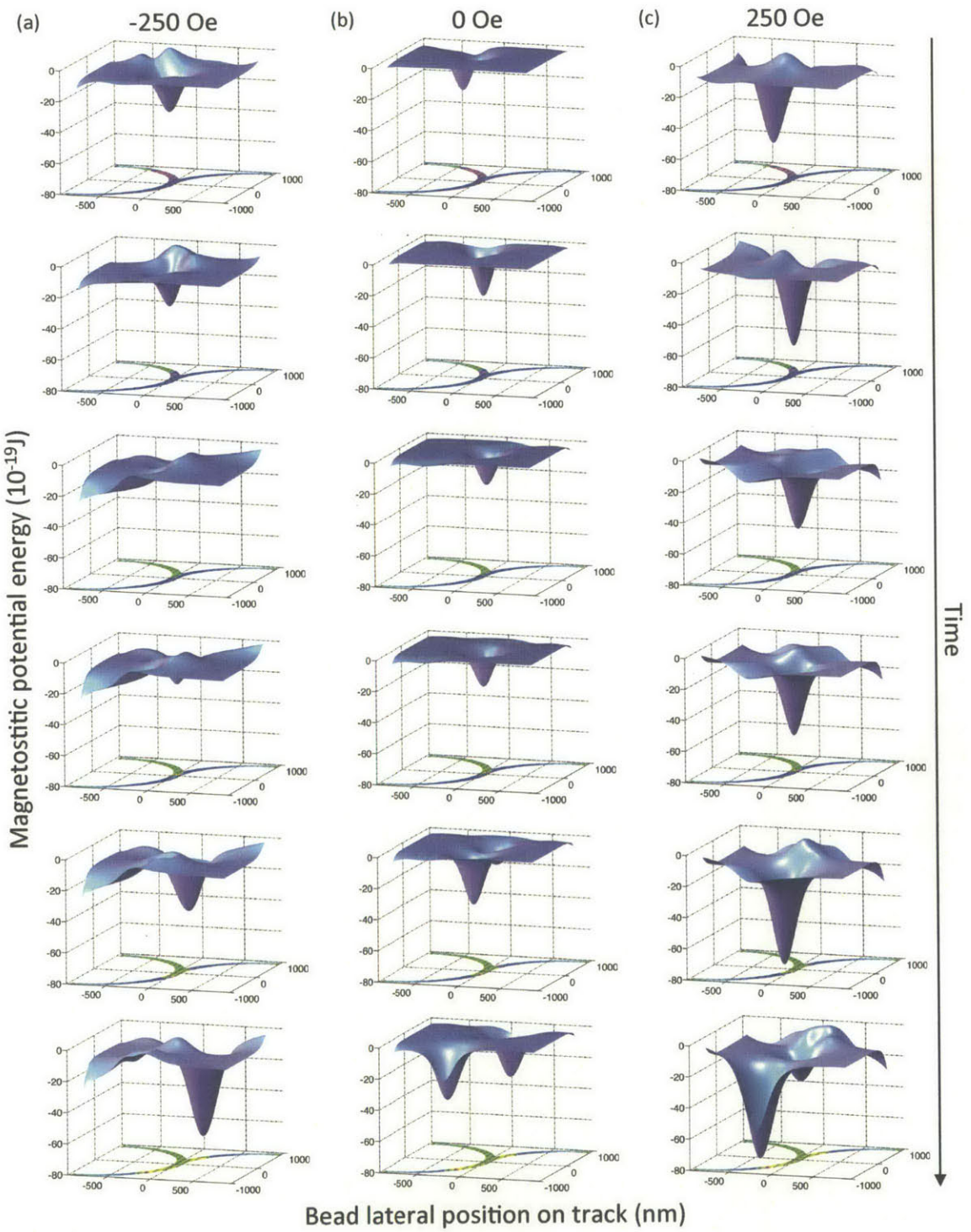

FIG. 6-6 Junction energy landscape under rotating in-plane field and dc vertical field

(a-c) Calculated magnetostatic potential energy surfaces for a 300 nm diameter bead over a junction in a 2 μm outer diameter, 100 nm wide, 60 nm thick Permalloy track containing two opposite DWs under rotating in-plane field and (a) -250 Oe, (b) 0 Oe, and (c) +250 Oe vertical field.

To verify the response of a bead at a junction to a vertical field, closed-loop curvilinear branching test structures [FIG. 6-4(a)] were fabricated. Such structures allow for the controlled motion of bead-DW pairs, while also keeping a bead in a closed circuit, which is useful for repeat measurements. Arrays of $Ni_{80}Fe_{20}$(40 nm)/Pt(2 nm) curvilinear tracks were prepared by electron beam lithography (Section 3.2.2), dc sputtering (Section 3.2.3), and liftoff (Section 3.2.4). Each track was 800 nm wide and composed of linked semi-circular segments with 20 μm outer diameter. Experiments were performed using M-270 beads. The motion of individual trapped beads was tracked using the assembly described in Section 3.3.7. Here, an ROI was defined at the inlet of a junction [FIG. 6-4(a, ROI1)] and used to trigger the application of a vertical field of a specific magnitude, polarity, and duration. The motion of a bead along either Path 1 or Path 2 was then obtained by the absence or passage, respectively, of the bead at ROI2 [FIG. 6-4(a)]. FIG. 6-7 shows how a vertical field is indeed able to select the direction of bead motion at the junction. A M-270 bead approaching the junction [FIG. 6-7(a)] is subjected to either a zero [FIG. 6-7(b)] or large [FIG. 6-7(c)] vertical field, resulting in its motion along Path 1 or Path 2, respectively.

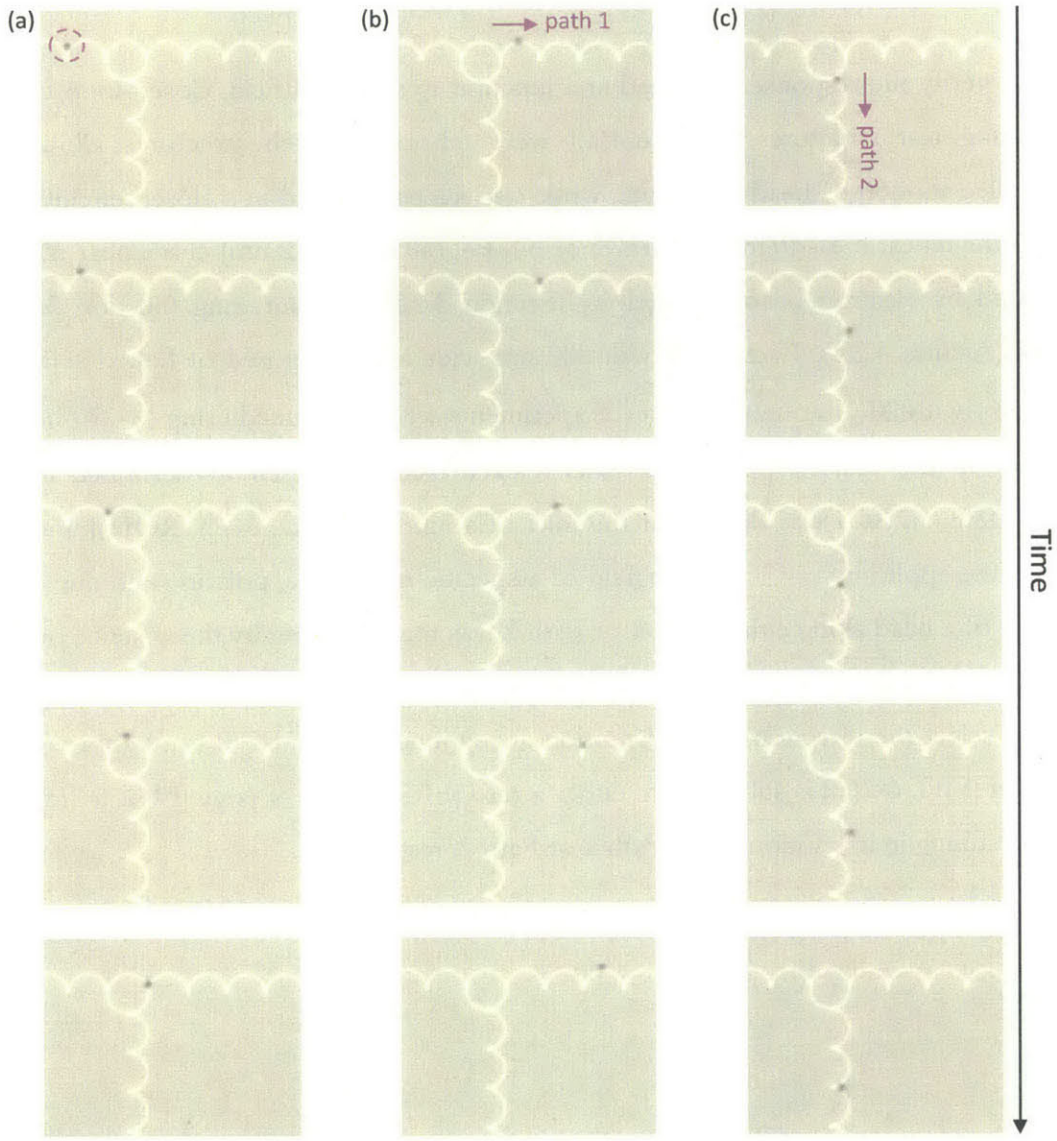

FIG. 6-7 Programmed bead motion through a junction

(a) M-270 bead (dashed circle) carried towards junction in a 20 μm outer diameter, 800 nm wide, 40 nm thick Permalloy track by a DW driven by an in-plane rotating field. (b) Under no vertical field, bead continues along Path 1. (c) Under large vertical field, bead continues along Path 2.

Repeated measurements of the motion of a M-270 bead across a junction, subject to positive and negative vertical fields ranging between 0 and 150 Oe, were collected. From these data, the probability for the bead taking Path 2 under various conditions was calculated. FIG. 6-8 shows the probability of the bead taking Path 2 as a function of vertical field polarity and magnitude, and the configuration of the DW exiting into Path 2 (Path 2 DW). The filled triangle data represent combinations of Path 2 DW and vertical field in which the applied field is subtractive to the DW stray field i.e. positive (up) with T-T DWs,

or negative (down) with H-H DWs. From simulation results [FIG. 6-5(b-d) and FIG. 6-6] we expect that the bead-DW interaction is weakened for the Path 2 DW and that consequently at no field magnitude should the bead prefer to move along Path 2. This is indeed seen experimentally in the data.

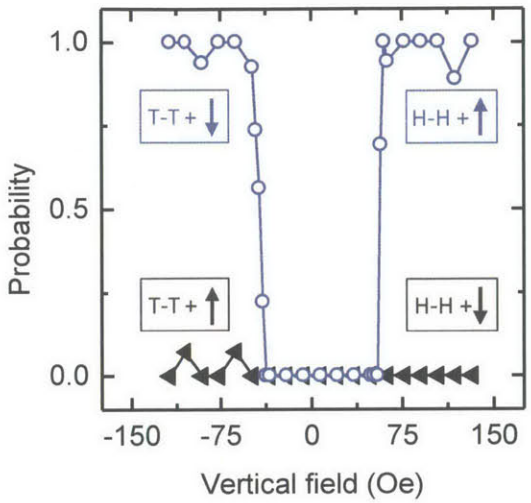

FIG. 6-8 Probability curves for bead motion at a junction

Probability of a M-270 bead taking Path 2 as a function of vertical field polarity and magnitude, and the configuration of the DW exiting into Path 2 (Path 2 DW). The two curves represent Path 2 DW and field polarity combinations in which the applied field is (filled triangle) subtractive and (open circle) additive to the DW stray field.

The open circle data represent combinations of Path 2 DW and vertical field in which the applied field is additive to the DW stray field i.e. negative (down) with T-T DWs, or positive (up) with H-H DWs. Here, we expect that the bead should travel along Path 2. These data show a clear threshold vertical switch-field value at 57 Oe, below which the bead travels along Path 1, but above which the preference for the Path 2 DW dominates, and the bead travels along Path 2. From these data it is clear that to achieve selection of bead direction at a junction, not only must the vertical field be of appropriate sign, but it must also be of appropriate magnitude.

It should be noted that the track for Path 2 itself contains a junction identical to the one under investigation. In order to insure a bead did not take, effectively, the Path 2 of Path 2, triggered vertical fields were applied only for the duration of bead passage through the junction of interest. The lack of vertical field during bead passage through the junction within Path 2 ensured that the bead continued along Path 2 and back into the circuit.

6.4.2 Sorting a two-bead population

That the bead will, for small vertical fields, still travel with the Path 1 DW despite the enhancement to the interaction with the Path 2 DW, suggests that there is threshold interaction between the bead and Path 2 DW necessary for Path 2 travel, and below which the bead will preferentially travel along Path 1. Given that the extent of bead-DW interaction depends on the size and susceptibility of the bead, we investigated whether observed thresholding in conjunction with differing bead characteristics could be used to realize bead-specific behavior under the same field conditions.

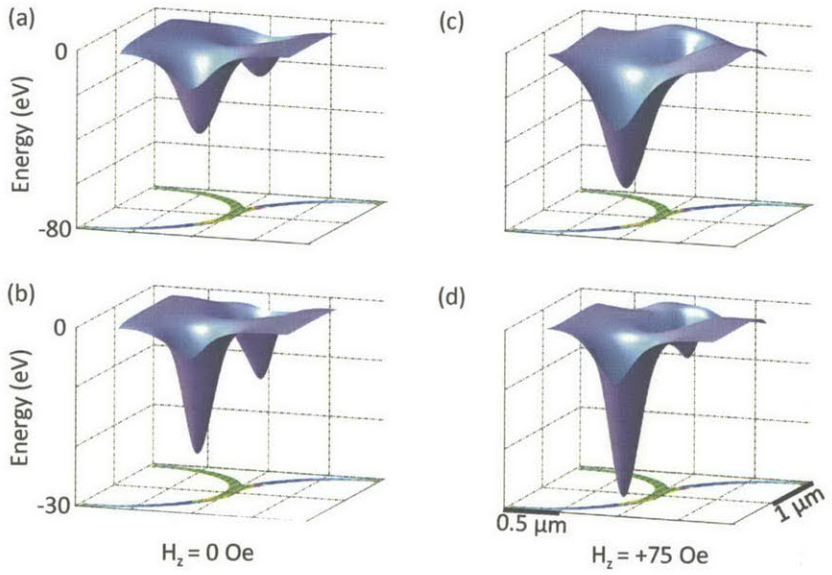

FIG. 6-9 Junction energy landscapes as a function of bead

(a-d) Calculated magnetostatic potential energy surfaces for (a) a 600 nm diameter and (b) 300 nm diameter bead in 0 Oe vertical field, and (c) a 600 nm diameter and (d) 300 nm diameter bead in +75 Oe vertical field over a junction in a 2 μm outer diameter, 100 nm wide, 60 nm thick Permalloy track containing two opposite DWs.

The effect of bead size was numerically simulated, and FIG. 6-9 shows the potential energy surfaces for two beads of different size over a junction under different vertical field conditions. FIG. 6-9(a-b) show the energy surfaces over a junction containing two exiting DWs for a 600 nm and 300 nm diameter bead, respectively, in zero vertical field. Although the energy surfaces for the two beads have similar features, it is clear they are very much a function of the particular bead being simulated. As such, it should be expected that the energy surfaces under vertical field should not respond identically, but rather also be a

function of the particular bead being simulated. Indeed, when a vertical field of +75 Oe is applied to the 600 nm and 300 nm diameter beads [FIG. 6-9(c-d)], in both cases the well above the Path 2 DW deepens while the well above the Path 1 DW gets shallower, but these changes for the two beads do not happen identically. From these results it is clear that whatever the threshold for travel with the Path 2 DW, it should occur at different values of vertical field for different beads. That is, the nature of the bead should determine the threshold vertical switch-field.

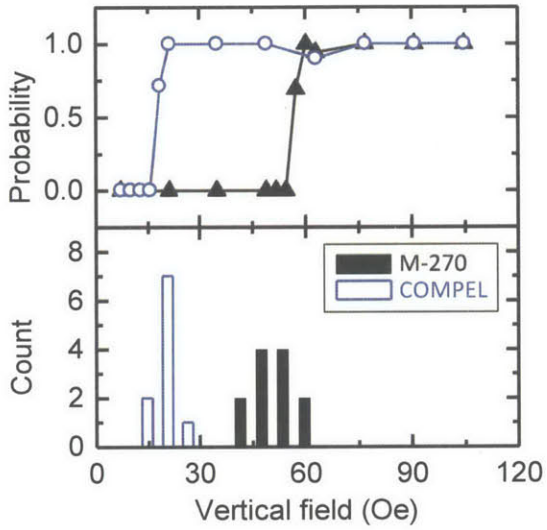

FIG. 6-10 Threshold vertical switch-field as function of bead

Threshold vertical switch-field data for (top) single and (bottom) population of COMPEL and M-270 bead(s).

This prediction was investigated experimentally. Following the approach previously outlined for the collection of FIG. 6-8 data, repeated measurements of the motion of two beads of different size and susceptibility across a junction were collected. In these measurements, the polarity of the applied vertical field was programmed to always be such as to enhance the bead interaction with the Path 2 DW, regardless of the incoming DW configuration. The probability for each bead taking Path 2 was then calculated as a function of vertical field magnitude and plotted in FIG. 6-10(top). The open circle curve represents data for a COMPEL bead, and the filled triangle curve represents data for a M-270 bead. There is a clear shift in threshold vertical switch-field, corroborating the predictions of FIG. 6-9. To test the reproducibility of these results, curves of Path 2 probability vs. vertical field amplitude were obtained for 10 COMPEL beads and 12 M-270 beads. A MATLAB fitting

program was then used to extract the threshold vertical switch-field from each curve. This point was taken as the vertical field amplitude at which the probability of the bead taking Path 2 was 0.5. The results of these statistics are plotted in FIG. 6-10(bottom), with the open bars representing the switch-field for COMPEL beads, and the filled bars representing switch-fields for M-270 beads. Again, there is a significant shift in the threshold vertical switch-field between the two populations, with the COMPEL beads averaging at 19 Oe and the M-270 beads at 52 Oe.

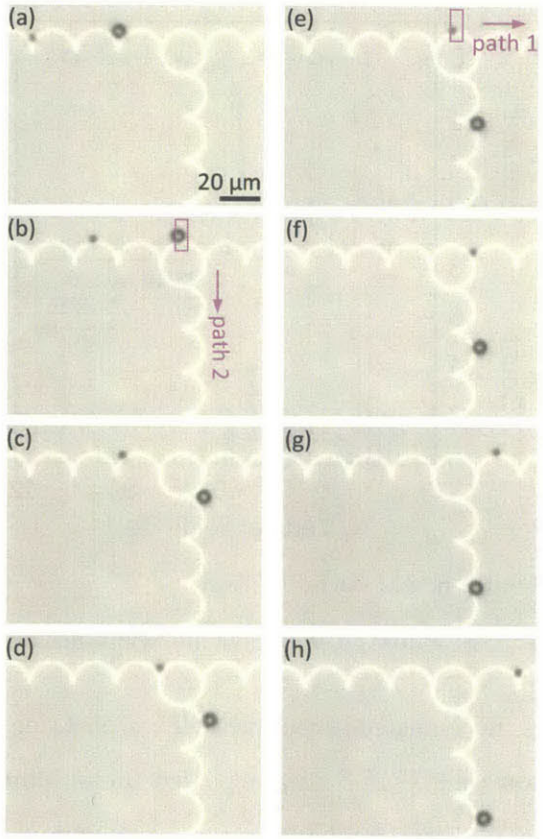

FIG. 6-11 Sorting a two bead population

(a-h) Motion of a COMPEL and M-270 bead through a junction in a 20 μm outer diameter, 800 nm wide, 40 nm thick Permalloy track, with a 35 Oe vertical field triggered by bead passage through ROI1 (rectangle) in (b) and (e). M-270 bead takes Path 1 whereas COMPEL bead takes Path 2.

Given these results, it follows that a vertical field of appropriate sign whose amplitude is between the switch-field values for the two bead populations would direct COMPEL beads along Path 2 and M-270 beads along Path 1, serving as a means of sorting. This capability is demonstrated in FIG. 6-11(a-h). FIG. 6-11(a) shows the approach of two beads, a COMPEL

bead followed by that of a M-270 bead, to a junction. As the COMPEL bead enters the junction [FIG. 6-11(b)] it triggers the ROI [FIG. 6-11(b, rectangle)] and a vertical field of 35 Oe is applied. Because this vertical field is larger than the threshold vertical switch-field for the COMPEL bead, the bead continues along Path 2 [FIG. 6-11(c-d)]. However, when the M-270 bead enters the junction and triggers the same 35 Oe vertical field [FIG. 6-11(e)], owing to that this triggered field is smaller than the switch-field for a M-270 bead, it continues along Path 1 [FIG. 6-11(f-h)]. Here, we have demonstrated a simple mechanism for the sorting of a mixed two-bead population.

6.5 Discussion

The goal of lab-on-chip systems is the fast, accurate, and automatic manipulation of biological species. One desirable feature is the identification and subsequent sorting of populations. In the next chapter and in other work[62-64,68,69], beads can be detected using DWs in magnetic tracks. However, there have been very few solutions[43] to handling post-identification sorting that integrate with a DW-based detection mechanism. The results reported in this chapter offer a DW-based mechanism for sorting, and one that, as will be seen in the next chapter, is compatible with our DW-based detection architecture.

With some simple track modifications, these results also enable improved sorting speed and resolution. We have shown the behavior of beads at circular nodes with three junctions. However, the number of junction branch points need not be limited to three. With the manipulation technique described, an arbitrarily large number of branch points can be defined off a circular node, and is only limited by the space required for each branching track. With more available paths comes an increase in potential device functionality.

Lastly, unlike other schemes whereby filtering is a result of different interaction between different species and the device, the interaction in this system is not predetermined by the track. That is, though the switch-field for a bead will be a function of its interaction with the track, whether it goes along e.g. Path 1 or 2 is not fixed, but rather controlled by an external stimulus. This allows for dynamic filtering despite the fixed track pattern.

This essential new capability of actively routing beads along specific routes in a complex nanotrack network adds a key building block for the development of magnetic lab-on-chip systems.

Chapter 7

Magneto-mechanical resonance detection[1]

Thus far, we have demonstrated that curvilinear tracks offer a suitable architecture in which DWs can be precisely controlled for bead manipulation and transport. By integrating a single-bead detection mechanism into such DW-based transport structures, microscale sorting and sensing of single cells or biomolecules could be achieved in magnetic lab-on-chip devices. Here we show that the bead-DW interaction can be used not only to reversibly trap individual beads for transport, but also to characterize the trapped beads based on their hydrodynamic response within a host fluid.

We show that the strong magnetostatic interaction between a bead and a domain wall leads to a distinct magneto-mechanical resonance that reflects the susceptibility and hydrodynamic size of the trapped bead. Numerical and analytical modeling is used to quantitatively explain this resonance, and the magneto-mechanical resonant response under sinusoidal drive is experimentally characterized both optically, whereby we demonstrate size-based discrimination amongst commercial microbead populations, and electrically, whereby we demonstrate resonance detection in a DW transport conduit. The observed bead resonance presents a new mechanism for microbead sensing and metrology. The dual functionality of domain walls as both bead carriers and sensors is a promising platform for the development of lab-on-a-bead technologies.

7.1 Magneto-mechanical resonance theory

FIG. 7-1(a-b) shows the cross sections of the calculated potential energy wells of FIG. 4-2(i)-(j), respectively, corresponding to bead sizes (2.8 μm and 1.0 μm diameter) used in

[1] Sections of this chapter, including figures, have been previously published in Rapoport, E. & Beach, G. S. D. Magneto-mechanical resonance of a single superparamagnetic microbead trapped by a magnetic domain wall. *J. Appl. Phys.* **111,** 07B310 (2012) and Rapoport, E., Montana, D. & Beach, G. S. D. Integrated capture, transport, and magneto-mechanical resonant sensing of superparamagnetic microbeads using magnetic domain walls. *Lab Chip* **12,** 4433–4440 (2012). Reprinted with permission from *Journal of Applied Physics* **111,** 07B310 (2012), Copyright 2012, American Institute of Physics and reproduced by permission of The Royal Society of Chemistry, respectively. Available at http://dx.doi.org/10.1063/1.3672406 and DOI: 10.1039/C2LC40715A, respectively.

experiment. The energy surface [FIG. 7-1(a, solid line)] for a 2.8 μm diameter bead is very well approximated by a parabolic harmonic potential [FIG. 7-1(a, dashed line)], such that the bead-DW restoring force F_{int} can be modeled as linear with force constant k for small relative displacements between the DW and trapped bead. For the smaller 1.0 μm diameter bead, whose potential landscape [FIG. 7-1(b, solid line)] is more sensitive to local DW stray field variation, a parabolic approximation [FIG. 7-1(b, dashed line)] holds relatively well for displacements on the order of half the bead diameter or larger.

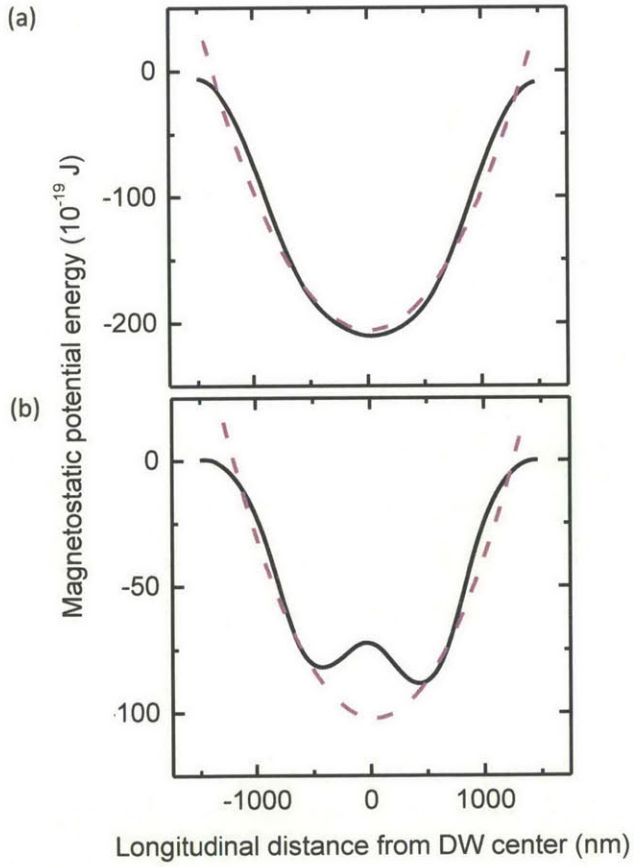

FIG. 7-1 Cross sections of magnetostatic potential energy surfaces

(a-b) Longitudinal magnetostatic potential energy surface cross sections (solid lines) fitted to harmonic potentials (dashed lines) versus lateral position for a (a) 2.8 μm diameter and (b) 1.0 μm diameter bead at the surface of a 800 nm wide, 40 nm thick Permalloy track containing a vortex wall.

Because of its quasilinear restoring force, the coupled bead-DW system should behave as a harmonic mechanical oscillator. If the DW is driven sinusoidally about a fixed position at low frequency, the bead is expected to track the DW motion. However, at higher

frequencies, the bead should lag behind the DW due to viscous drag, leading to a frequency-dependent phase shift between the motion of the two. Due to viscous damping in the fluid, the coupled system should thus exhibit an overdamped resonant response to an external periodic excitation, with a characteristic resonance frequency dependent on the restoring force and the viscous drag.

We consider the curved track geometry of FIG. 7-2, in which a DW is driven about a fixed position by a pair of orthogonal in-plane magnetic fields. A radial bias field $H_b\hat{\boldsymbol{y}}$ establishes the equilibrium DW position, while a tangential ac field $h(t)\hat{\boldsymbol{x}}$ drives the DW sinusoidally about that position. As the DW is displaced by an angle ϕ from the $\hat{\boldsymbol{y}}$ axis, it experiences a force $-2\mu_0 M_s t w H_b \sin(\phi)$ from the bias field proportional to the tangential projection of the field along the track. If the DW displacement x_{DW} along the track perimeter is small compared to the track radius R_{track}, then $\sin(\phi) \approx x_{DW}/R_{track}$ and the bias field exerts a linear restoring force on the DW. In the absence of a trapped bead, the DW simply follows $x_{DW} = (h(t)/H_b)R_{track}$.

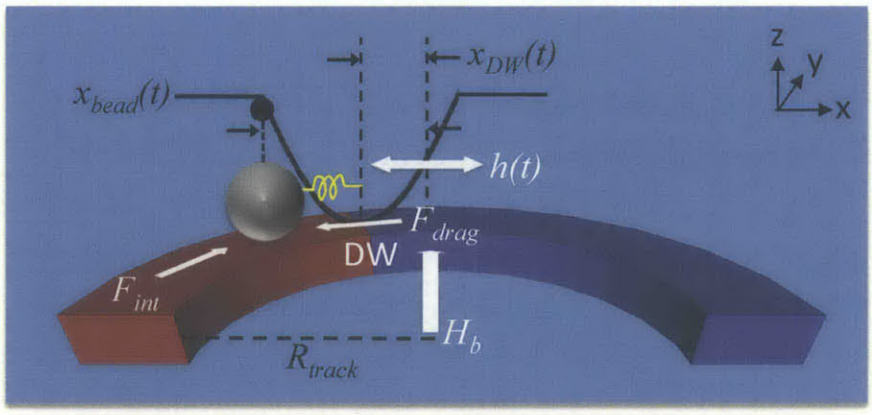

FIG. 7-2 Model of resonance dynamics for the bead- DW system

Schematic of the oscillator geometry in the bead-DW system with curvilinear track. The bead at position $x_{bead}(t)$ is tethered to the DW at position $x_{DW}(t)$ by a restoring force F_{int} arising from the magnetostatic interaction potential. The viscous drag force F_{drag} from the fluid on the bead resists bead motion that is a result of DW oscillation from $h(t)$ around an equilibrium position defined by H_b. Track generated by U. Bauer.

When an oscillating DW has trapped a SPM bead, its motion couples to that of the bead through a magnetostatic interaction via a force[139] linear in their relative displacement [Eq. (28)]. Viscous drag from the fluid acts to resist the motion of the bead as it is dragged by the

DW, leading to a damping term [Eq. (29)]. Assuming strongly overdamped conditions (i.e., neglecting inertial terms), we hence arrive at a set of coupled equations of motion for the bead and DW coordinates $x_{bead}(t)$ and $x_{DW}(t)$,

$$-k(x_{bead} - x_{DW}) - b\frac{d}{dt}x_{bead} = 0 \tag{36}$$

$$+k(x_{bead} - x_{DW}) - \frac{CH_b}{R_{track}}x_{DW} + Ch(t) = 0, \tag{37}$$

where $C = 2\mu_0 M_s tw$. Eq. (36) and Eq. (37) account for forces on the bead and DW, respectively. For a sinusoidal drive field $h(t) = h_0 e^{-i\omega t}$, these equations can be solved assuming a harmonic response from both the bead and DW, $x_{bead}(t) = \delta_{bead} e^{-i\omega t}$ and $x_{DW}(t) = \delta_{DW} e^{-i\omega t}$, where δ_{bead} and δ_{DW} are the complex oscillation amplitudes of the bead and DW, respectively.

In the dc limit, the bead and DW move in unison, following the driving field with a displacement amplitude $\delta^0_{bead} = \delta^0_{DW} = R_{track}h_0/H_b$. At higher frequencies, viscous drag causes the bead to lag behind the DW, resulting in an overdamped resonant response given by

$$\frac{\delta_{bead}}{\delta^0_{bead}} = \frac{1}{1+\omega^2/\omega_0^2} + \frac{\omega/\omega_0}{1+\omega^2/\omega_0^2}i. \tag{38}$$

Here, the resonance frequency is given by

$$\omega_0 = \Gamma\tilde{\omega}_0, \tag{39}$$

where we define

$$\tilde{\omega}_0 = \frac{k}{b} \tag{40}$$

and

$$\Gamma = \left(1 + \frac{kR_{track}}{CH_b}\right)^{-1}. \tag{41}$$

The quantity CH_b/R_{track} is the effective linear restoring force constant that the bias field imposes on the DW. For large bias fields, $\Gamma \to 1$ and the bead exhibits a magneto-mechanical resonance at a frequency $\omega_0 \to \tilde{\omega}_0 = k/b$. Note that a finite bias field is required for a finite resonance frequency of the coupled system.

Because the bead and DW are coupled, the latter exhibits a response that closely follows the former, given by:

$$\delta_{DW} = \Gamma\delta^0_{bead} + (1 - \Gamma)\delta_{bead}. \quad (42)$$

Compared to the bead response, the amplitude of the dissipative peak and the falloff of the in-phase oscillation amplitude as the system goes through resonance are smaller for the DW by a factor $(1 - \Gamma)$. This factor is a measure of the dominant restoring force on the DW. In the limit of a large bias field, $\Gamma \to 1$ and the DW simply tracks the ac field with oscillation amplitude $\Gamma\delta^0_{bead}$ as the bead goes through resonance. However, at smaller $H_{//}$, magnetostatic coupling between the bead and the DW has increasing influence on the latter, leading the DW oscillation amplitude to more closely follow that of the bead as the coupled pair are driven through resonance.

This analysis suggests that resonance can be used to distinguish beads of different sizes from either the bead or the DW response to a frequency-dependent drive field.

7.2 Optical characterization of resonant dynamics

We experimentally characterized the small-amplitude magneto-mechanical resonant response of a trapped bead under sinusoidal drive. Arrays of identical $Ni_{80}Fe_{20}$ ring tracks were prepared by electron beam lithography (Section 3.2.2), dc sputtering (Section 3.2.3), and liftoff (Section 3.2.4). Each track was 800 nm wide, 40 nm thick, and 30 μm in outer diameter. Experiments were performed using MyOne and M-270 beads, with mean diameters of 1.0 μm and 2.8 μm, respectively.

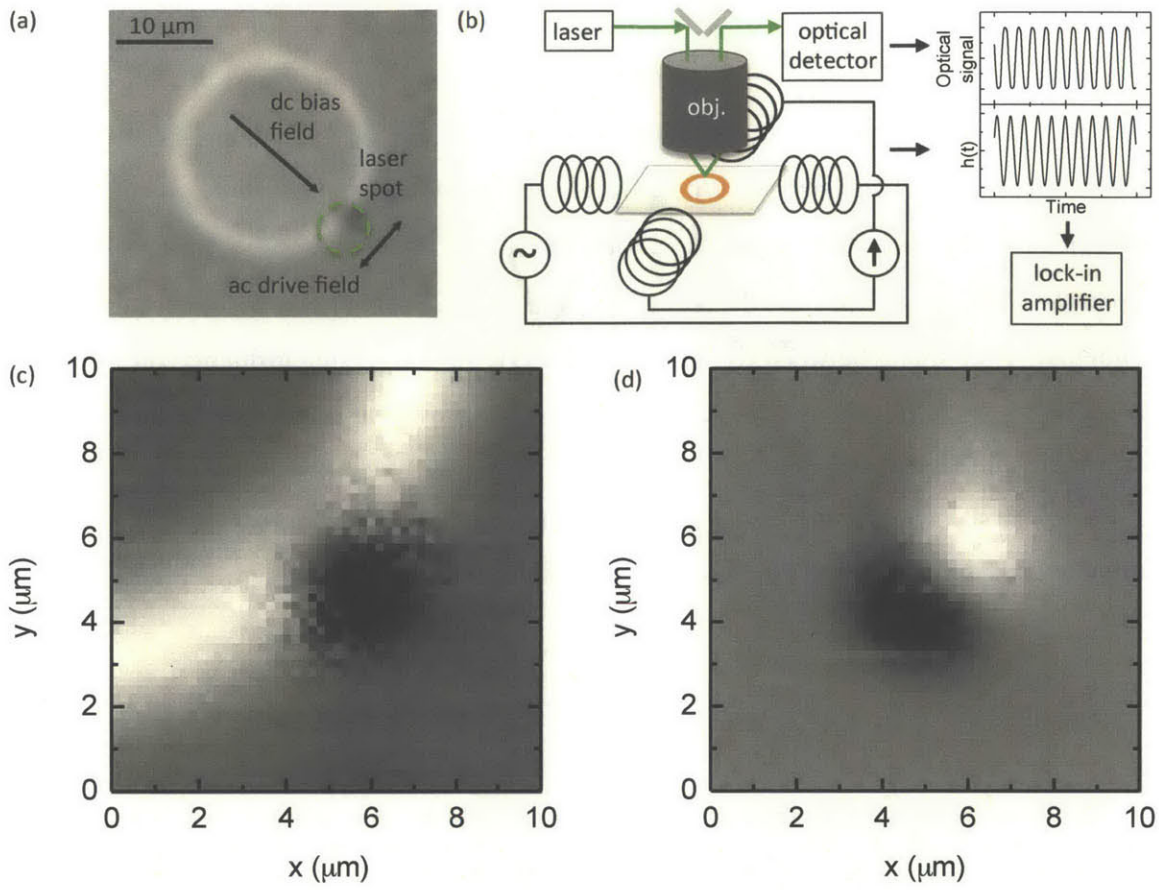

FIG. 7-3 Optical characterization of magneto-mechanical resonance

(a) Optical image showing a 1.0 μm diameter bead on a 20 μm outer diameter, 800 nm wide, 40 nm thick Permalloy ring, along with field configuration and probe laser spot location (dashed circle). (b) Schematic of experimental setup for optical detection of magneto-mechanical bead resonance. (c-d) Maps of a bead on a track as in (a) taken during bead oscillation at 20 Hz, showing (c) optical reflectivity and (d) the in-phase component of oscillation.

The experimental technique is outlined in FIG. 7-3. FIG. 7-3(a) shows the field configuration used to drive the bead into oscillation. As previously discussed in Section 5.1, the ring geometry permits a high degree of control over DW nucleation and positioning. In Chapter 5 we applied a strong rotating in-plane magnetic field to generate DWs along the field axis and circulate them about the ring with a sense and frequency consistent with that of the drive field. In order to measure the resonant characteristics of the bead-DW system, here we use the ability to precisely position DWs in another mode. The application of a large dc bias field in conjunction with a small amplitude ac field transverse to the pinning dc field [FIG. 7-3(a)] will drive a DW sinusoidally about a fixed equilibrium position. In this configuration there is significant transverse field, however our calculations showed that

application of a transverse in-plane field does not appreciably affect the interaction force between a bead and a DW[139].

Samples were prepared as described in Section 3.3.3. Then, a dc bias field H_b was applied to fix an equilibrium DW position, while an orthogonal in-plane ac field $h(t)$ was used to drive DW oscillations about that position. The dynamic response of individual trapped beads was tracked using a high-bandwidth laser microprobe integrated into the imaging microscope, as shown schematically in FIG. 7-3(b). FIG. 7-3(b) shows the ac drive field signal and corresponding optical reflectivity trace obtained for a trapped 2.8 μm bead driven at $f = 10.5$ Hz, with $H_b = 250$ Oe and $h_0 = 20$ Oe, corresponding to a quasistatic displacement amplitude of ~1 μm. The trace shows a periodic decrease (increase) in reflected intensity as the bead moved into (out of) the probe spot. At this low frequency, the bead motion is seen to closely follow $h(t)$, but at higher frequencies, a phase shift between the driving field and the bead response is expected.

The extent to which bead motion follows the drive field, both in oscillation amplitude and phase, was quantified. At a given ac field frequency, the optical reflectivity signal and the ac drive signal were fed into a lock-in amplifier, from which the in-phase and out-of-phase components of bead oscillation with respect to drive field were obtained. At a given frequency, the amplitude of these signals is dependent on laser probe position with respect to the oscillating bead. FIG. 7-3(c) and FIG. 7-3(d) show maps of optical reflectivity and in-phase signal, respectively, for a 2.8 μm bead driven into oscillation by a 20 Hz field on a 20 μm outer diameter ring. It is clear that the peak in-phase signal is not centered at the equilibrium bead position, but rather offset to either side. With the probe centered at the equilibrium position, the frequency of reflectivity signal is twice that of the drive field frequency, such that the in-phase signal is low (if we were to look at the in-phase component of the second harmonic, however, this should be at a maximum). As the probe is positioned farther from the bead equilibrium position, the in-phase signal also dies out because the range of bead oscillation is limited. Thus, in order to obtain a resonance response curve with the highest signal to noise, the laser probe should be positioned at one of the two regions of maximum intensity in the in-phase signal map. Indeed, during measurement, the laser probe spot was defocused to ~5 μm in diameter and positioned near a bead such that bead oscillation was restricted to one side of the Gaussian spot profile [FIG. 7-3(a, green circle)],

where the detected intensity varied monotonically with bead position for small oscillation amplitudes.

Magneto-mechanical resonance response curves were generated by sweeping the ac drive frequency logarithmically through three decades, while monitoring the reflected laser intensity with a lock-in amplifier phase-locked to $h(t)$. FIG. 7-4(a) shows the in-phase and out-of-phase optical signal versus frequency for representative beads from the two size populations. In each case, the data are well fitted by the overdamped resonance model described above. The smaller bead exhibits a markedly higher resonance frequency, $f_0 = \frac{\omega_0}{2\pi}$, than the larger bead, as is expected from the inverse dependence of f_0 on hydrodynamic radius.

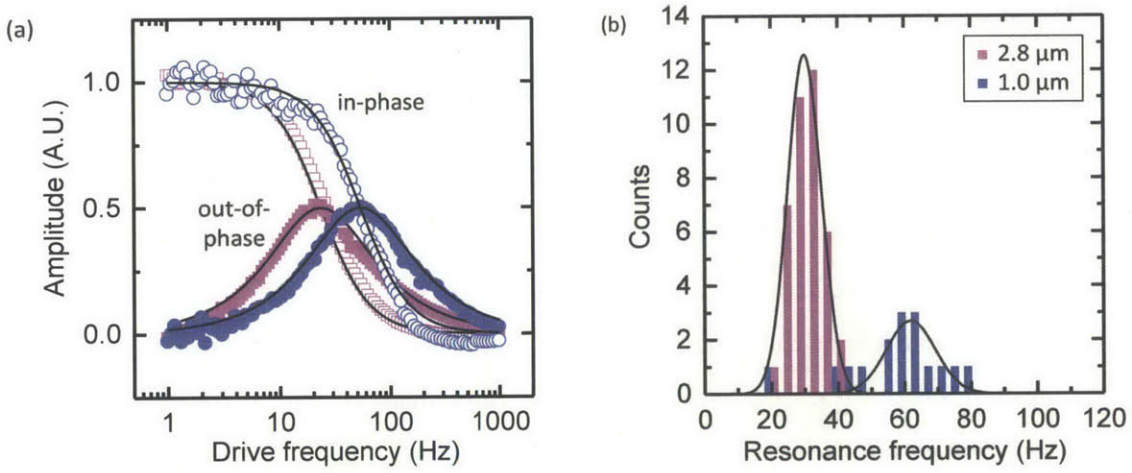

FIG. 7-4 Resonance curves and statistics for two different sized beads

(a) Resonant excitation of trapped 2.8 μm diameter (squares) and 1.0 μm diameter (circles) bead in aqueous environment by oscillating DW in circular magnetic track. Curves show in-phase (open symbols) and out-of-phase (closed symbols) optical reflectivity signal, approximately proportional to bead oscillation amplitude. (b) Histograms of measured resonance frequencies for 2.8 μm diameter and 1.0 μm diameter beads, with mean resonance frequencies of 30.3 Hz and 58.3 Hz, respectively.

Resonance measurements were repeated for 39 large beads and 16 small beads to determine the variation of f_0 within and between these bead populations. FIG. 7-4(b) shows measured distributions in f_0 for each bead size. The data are normally distributed with a mean of 30.3 Hz for the 2.8 μm beads and 58.3 Hz for the 1.0 μm beads.

These resonance frequency data are in quantitative agreement with prediction based on the resonance model described in Section 7.1. The numerically-computed potential wells for

the 2.8 and 1.0 μm beads in FIG. 7-1(a-b) yield fitted k values of 2.2×10^{-5} J m^{-2} and 1.4×10^{-5} J m^{-2}, respectively. Taking modified Stoke's drag [Eq. (22)] with a viscosity $\eta = 10^{-3}$ Pa s of water and a near surface correction factor [Eq. (21)] of ξ = 3.1 for a bead touching and moving parallel to a plane wall (as in Section 4.2), we estimate a ratio of small to large bead resonance frequency of 1.88. The ratio of mean resonance frequency for the two bead populations closely follows prediction at a value of 1.92. Furthermore, the observed mean resonance frequency for each population is within 15%.

The standard deviation in f_0 for the 2.8 μm bead population is 4.4 Hz, corresponding to a coefficient of variation (CV) of 14.5% of the mean. For the 1.0 μm beads, the CV is somewhat larger at 24.9% of the mean. The bead size distribution specified by the manufacturer is < 3% for both the MyOne and M-270 beads. Hence, the significantly wider f_0 distributions point to a corresponding distribution in bead magnetic content. Surface adhesion between the beads and the substrate likely also contributes to variability in the measured response, and nonspecific binding was found to be more prevalent for the 1.0 μm MyOne^{TM}, which may explain the relatively large CV for these beads. Nonetheless, these data show that the magneto-mechanical resonance can be used to robustly distinguish between these two bead populations.

Here we have shown that the magnetostatic binding between a DW and a trapped bead can be used to interrogate that bead dynamically, offering a new mechanism for microbead metrology with single-bead sensitivity. In the next section, with the aid of a spin-valve structure for position-sensitive tracking of the DW oscillation, we show that we can use this same mechanism to detect the resonant response of the coupled system electrically

7.3 Electrical integration for magnetoresistive sensing

To create an infrastructure capable of trapping, transporting, and sensing all on-chip, we developed a curvilinear track with a trilayer pseudo-spin-valve [FIG. 2-9(c)] structure for electrical measurement of the DW resonant response. Bead capture and transport is accomplished using a mobile DW in the top (free) layer, while the bottom (fixed) layer remains uniformly magnetized and serves as a reference. In this structure, the DW position

and its dynamic response can be detected electrically via the giant magnetoresistance effect as described in Section 2.4 and in more detail below.

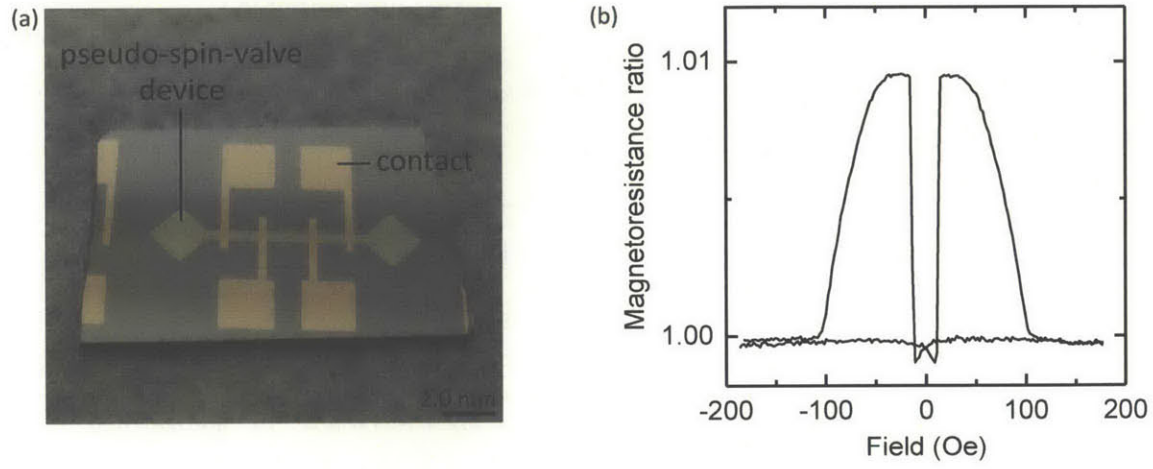

FIG. 7-5 Test pseudo-spin-valve structure

(a) Optical image of test pseudo-spin-valve structure with optimized composition of $Co_{50}Fe_{50}$ (8 nm)/ Cu (5 nm)/ $Ni_{80}Fe_{20}$ (40 nm). (b) Magnetoresistance response curve of optimized structure in (a).

Test pseudo-spin-valve stacks [FIG. 7-5(a)] with composition $Co_{50}Fe_{50}$(8 nm)/Cu(t nm)/$Ni_{80}Fe_{20}$(40 nm), and Cu spacer thickness t varying between 2.5 and 9 nm were fabricated by a combination of shadow mask lithography (Section 3.2.1) and dc sputter deposition (Section 3.2.3) in order to determine the optimum t value that minimized magnetostatic coupling between the two magnetic layers while maintaining an acceptable maximum magnetoresistance ratio (MR). The $Ni_{80}Fe_{20}$ layer thickness was fixed to be the same 40 nm as for the structures in Section 3.1. FIG. 7-5(b) shows the magnetoresistive response to a sweeping magnetic field for a test pseudo-spin-valve structure of the optimized composition ($t = 5\ nm$, MR~ 1%). We note that in optimized systems free of our material and geometrical restrictions, pseudo-spin-valve MR ratios can get as high as above 40%[92]. However, in our case, we find even this relatively small MR value to be sufficient for a proof of concept demonstration of bead detection via electrical measurement of magneto-mechanical resonance.

Real device fabrication consisted of three sequential steps of lithography (Section 3.2.2), deposition (Section 3.2.3), and liftoff (Section 3.2.4). Initial Ti(4 nm)/Au(100 nm) contact patterns were created by optical lithography, evaporation, and liftoff. $Co_{50}Fe_{50}$(8 nm)/Cu(5

nm)/$Ni_{80}Fe_{20}$(40 nm)/Pt(2 nm) pseudo-spin-valve tracks were then created by electron beam lithography, dc sputtering, and liftoff. Finally, Ti(2 nm)/Au(100 nm) contact lines between the tracks and the optically defined lines were patterned and deposited by electron beam lithography and evaporation, respectively.

The tracks are composed of linked semi-circular segments, such that DWs are initiated and repositioned by application and rotation of an in-plane magnetic field, respectively. In this geometry, beads can be translated synchronously with DWs at a well-defined speed. FIG. 7-6(a) shows optical microscopy images of a pseudo-spin-valve curvilinear track and its transport functionality. A 2.8 μm diameter bead is shuttled right and left along the track by application of counterclockwise and clockwise field rotation, respectively. We have previously demonstrated this functionality in a single-layer track (FIG. 6-1). The results in FIG. 7-6(a) demonstrate that transport can likewise be achieved in the present trilayer structure, and that the overlaid electrical contacts do not impede bead motion.

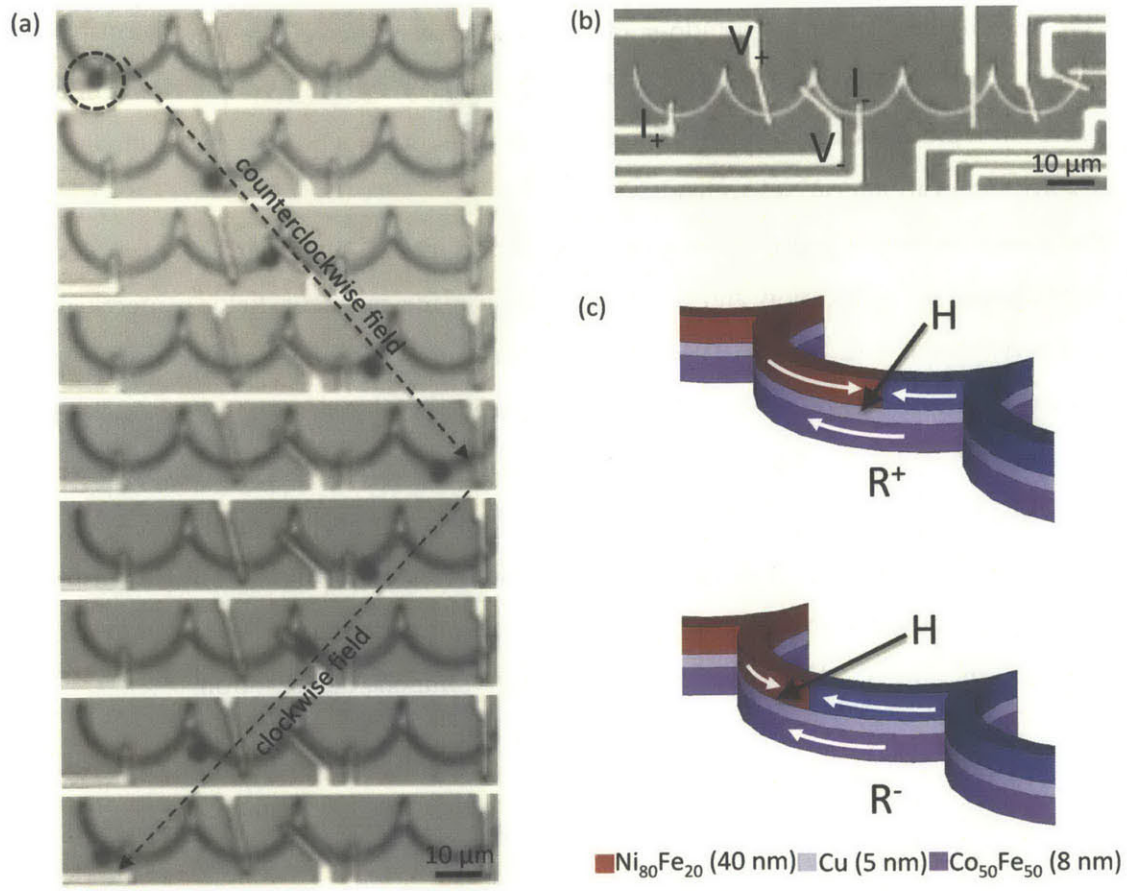

FIG. 7-6 Pseudo-spin-valve track for magnetoresistive sensing

(a) Sequential optical image snapshots during applied field rotation of trapped 2.8 μm diameter bead driven along a curvilinear $Co_{50}Fe_{50}$(8 nm)/Cu(5 nm)/$Ni_{80}Fe_{20}$(40 nm) pseudo-spin-valve track of linked 20 μm outer diameter, 800 nm wide half-ring segments. Counterclockwise and clockwise field rotation results in motion to the right and the left, respectively. (b) Curvilinear trilayer pseudo-spin-valve track, as in (a), for electrical detection of bead-DW magneto-mechanical resonance. Current and voltage leads indicated. (c) Change of pseudo-spin-valve track resistance as DW position in top magnetic layer is modulated by externally applied field. Track generated by U. Bauer.

The magnetic track and electrical contact lines are shown in more detail in FIG. 7-6(b), together with a schematic illustration describing the principle of the magnetoresistive measurement of DW position [FIG. 7-6(c)]. The pseudo-spin-valve stack structure consists of a nonmagnetic spacer layer sandwiched between a magnetically-soft top and magnetically-hard bottom layer [FIG. 7-6(c)]. In this structure, after application of a longitudinal saturation field, a DW can be introduced and manipulated in the top layer, while the bottom layer remains uniformly magnetized. In the top configuration of FIG. 7-6(c), a longer segment of the track is antiparallel aligned, resulting in a relatively higher resistance, R^+. As the DW is repositioned by the applied in-plane field [FIG. 7-6(c, bottom)], the portion of the

track that is aligned in the parallel state increases, resulting in a relatively lower resistance, R^-. Therefore, as the DW is sinusoidally driven between these two positions, the track resistance varies sinusoidally between R^+ and R^-.

FIG. 7-7 shows the experimental setup at the device scale and a schematic description of the associated electronics. The sample is placed on a stage in the plane of the custom-built magnet. Contact is made to the chip by an electrical contact adapter plate that has a center square cutout for optical access. An ac current source supplies a 100 μA, 50 kHz current to the device, and the resistance is measured by comparison of the voltage to the reference ac signal with a Stanford Research SR830 lock-in amplifier (lock-in '1').

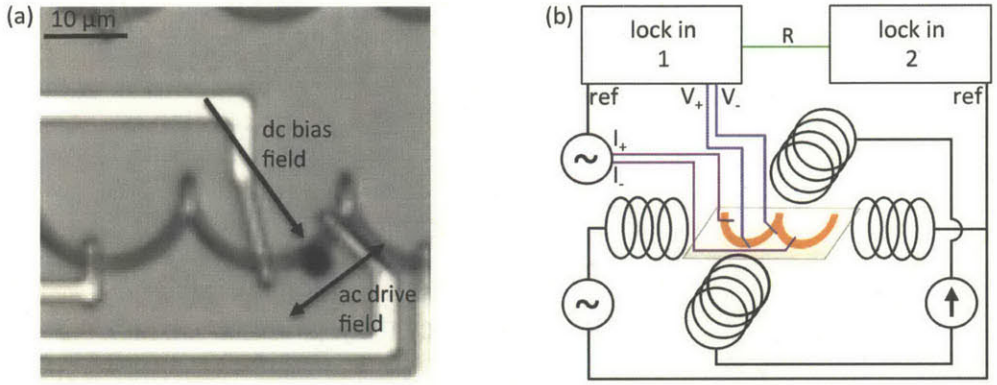

FIG. 7-7 Electrical measurement of DW magneto-mechanical resonance

(a) Optical image of a 2.8 μm diameter bead trapped by DW positioned between two voltage leads of the pseudo-spin-valve curvilinear track with geometry of applied field. (b) Schematic of electronics configuration for measurement of DW resonance.

Before measurement, a bead-DW pair is positioned in the active device area [FIG. 7-7(a)]. During measurement, the excitation field is swept logarithmically from 1 to 1000 Hz. The track resistance is fed into a second SR830 lock-in amplifier (lock-in '2') phase locked with the drive field. The high output bandwidth of lock-in '1' is such that, with a maximum drive field frequency of only 1000 Hz, accurate resistance measurements can be obtained across the field sweep range. The drive frequency is swept from low to high in 600 s with a lock-in '2' time constant of 1 s such that there is sufficient sampling across the frequency spectrum.

The resonant response of a DW under these conditions is shown in FIG. 7-8. The two curves show the in- and out-of-phase components of resistance, proportional to the DW

oscillation amplitude, for a DW bound to a 2.8 μm diameter bead. The predicted resonant behavior is clearly evident from these data, and the measured resonance frequency of 25 Hz is within the expected range for this bead and track geometry. The form of the measured resonance curve agrees qualitatively with Eq. (42), which predicts a finite DW oscillation amplitude far above resonance. At high frequencies, the bead is effectively immobile and acts like a fixed potential well that restricts the amplitude of the field-driven DW motion but does not diminish it entirely.

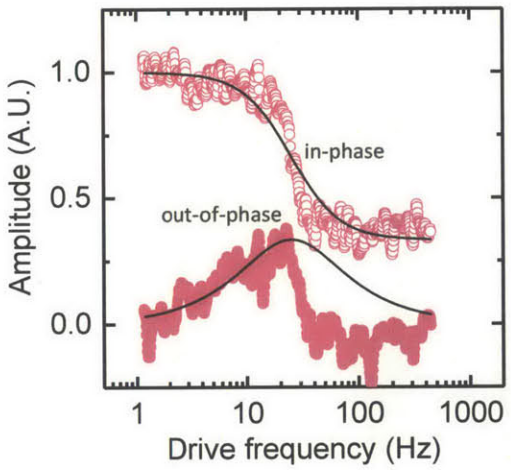

FIG. 7-8 Resonance curve from magnetoresistance measurement

In- and out-of-phase resonance response curves of a DW in the pseudo-spin-valve track bound to a 2.8 μm diameter bead suspended in water.

Unlike the optically-measured resonance curves, the curves in FIG. 7-8 are asymmetric, with both the in- and out-of-phase oscillation amplitudes falling off more rapidly with frequency than the simple harmonic oscillator model predicts. This effect is most likely due to pinning of the DW by defects (edge roughness) in the track, which becomes more important when the oscillation amplitude begins to drop as the system goes through resonance. In the optical resonance experiments, a larger bias field can be used (such that $\Gamma \sim 1$ in Eq. (41)), ensuring that the DW stiffly follows the drive field even in the presence of pinning. However, in the electrical measurement, it is necessary to reduce the bias field amplitude to keep $\Gamma < 1$, as per Eq. (42), such that the DW is more susceptible to the magnetostatic influence of the bead. At the same time, under these conditions the DW is also more susceptible to the effects of pinning by defects in the nanotrack, and the sharper

dropoff in signal past the resonant peak likely reflects more irregular DW motion as the oscillation amplitude drops. Device fabrication using a subtractive etching technique such as Ar ion milling rather than liftoff should reduce these effects by reducing edge roughness. Nonetheless, these experiments clearly demonstrate the resonant DW response due to its interaction with a trapped bead, and show that this response can be detected electrically using simple spin-valve devices.

7.4 Discussion

The results described in this chapter show that nanotrack-guided DWs can be used to capture, transport, and interrogate the physical properties of individual magnetic microbeads in a host fluid. DW-based devices therefore offer a possible means to realize a digital lab-on-a-bead platform, where biotarget capture occurs on the surface of microbeads rather than on the surface of the chip, and sensed biomaterials could be subsequently transported or sorted using mobile DW traps. Biosensor chips based on magneto-mechanical resonant sensing would not require pre-functionalization, but would be generic in their operation. Specific detection targets would be chosen by the end user at the point-of-use through selection of beads with the desired surface chemistry. Moreover, this DW-based approach offers added transport functionality that could augment or eliminate the need for, e.g., microfluidic actuation and associated hardware.

We have demonstrated that the magneto-mechanical resonance can be used to reliably discriminate between commercial microbead populations with substantial differences in their hydrodynamic radii. The ultimate goal of lab-on-a-bead sensing systems is to allow detection of analyte hybridization to functionalized beads, typically through DNA-cDNA recognition, or through an immunoassay recognition. Based on the results above, an increase in hydrodynamic radius of several hundred nm (significantly larger than the typical size of individual biomolecules) would be required to statistically separate decorated from undecorated beads in a population of 2.8 μm beads. However, there are several biorecognition strategies that would be compatible with the demonstrated sensitivity to hydrodynamic radius afforded by DW-based magneto-mechanical resonant sensing. In Strömberg et al.[65,135], Brownian relaxation biodetection was based on the formation of

clusters of magnetic beads bound by a network of DNA or antibodies using a volume-amplified approach. These clusters indicated the presence of an analyte via a change in the Brownian relaxation frequency as compared to unclustered magnetic beads. The approach described here could offer a means to detect chemically-bound magnetic clusters in a chip-based DW device through this same biochemical recognition strategy. Alternatively, bead-on-bead sandwich assays[3,4,73] have been successfully employed for e.g. protein detection[4], and offer a possible means to realize biosensing in DW-based devices. In Jans et al.[4], magnetic microbeads were used for target protein capture, and secondary Au nanoparticles hybridized with the capture microbeads were used for optical signal transduction. An analogous approach could be used for biomolecule detection in DW-based devices, whereby secondary bead hybridization to magnetic capture beads in the presence of a target analyte would lead to a detectible change in hydrodynamic radius. Finally, in cases in which the target analyte is a discrete object such as a cell or bacterium, on-the-fly detection in chip-based devices has been demonstrated by labeling the target with magnetic nanoparticles. For such applications, DW-based transport conduits could simultaneously capture, transport, and sense the presence of the analyte through its hydrodynamic characteristics.

Chapter 8

Summary and outlook

8.1 Summary

Through the work of this thesis, we have presented a thorough picture, from fundamentals to applications, of the interaction between magnetic DWs and SPM microbeads. Beginning with calculation, we predicted a strong magnetostatic binding interaction between beads and DWs that is a function of track and bead geometry and material parameters. We proposed that fast DW-mediated bead motion through a fluid was possible if the gradient stray field was used to trap beads to mobile DWs rather than drive the motion of beads towards stationary DWs. Experiment supported these predictions and DW-mediated bead transport at very high velocities was achieved and tailored by appropriate selection of track material and application of out-of-plane fields in prototype ring structures. Moreover, we found very little variation in behavior among a population of nominally identical bead-DW pairs under the same conditions.

As we continued to explore bead-DW dynamics, the richness and flexibility of the bead-DW interaction became clear. Beyond the maximum velocity for continuous bead transport, we discovered a knocking mode in which a train of continuously passing DWs can be used to translate a bead by incremental steps whose size is dependent on the amplitude and frequency of the external drive field. With this mode, bead transport along straight tracks becomes theoretically possible. For long-distance transport, we demonstrated that a curvilinear backbone consisting of links of semi-circular segments could be used. Along such structures, the same rotating field that drove synchronous bead-DW motion around rings was used to drive bead-DW motion in an overall linear fashion. With the introduction of a junction to the curvilinear backbone, we showed that a vertical field selected the direction of bead motion at the junction. Furthermore, because the ability to select bead direction at a junction relies on the nature of the bead-DW interaction, we were able to demonstrate sorting of a heterogeneous population of beads by application of the same vertical field to both types of beads entering a junction.

Finally, we showed that the bead-DW interaction is not just limited to transport, but can be used for bead detection as well. We showed that the bead-DW magnetostatic interaction leads to a distinct magneto-mechanical resonance that is quantitatively well described by an overdamped harmonic oscillator model. We then demonstrated that the magneto-mechanical resonance can be used to distinguish bead populations based on their size, and that the resonant behavior of the coupled bead-DW system can be sensed electrically using simple pseudo-spin-valve devices integrated into the transport architecture.

By harnessing the mobility and strong gradient field of DWs, using specially designed track structures, and carefully investigating bead-DW dynamics, we have successfully developed an architecture integrating single bead capture, transport, and metrology on-chip, going one step further toward successfully realizing a complete multifunctional magnetic lab-on-chip system.

8.2 Future work

The work of this thesis demonstrates foundational components necessary for the development of magnetic lab-on-chip systems. These proof-of-concept results create an opportunity for a range of future explorations. In this final section, we discuss ideas for future work that follow as natural extensions of the work already done here.

8.2.1 Integration and biological testing

A major motivation for this work was toward the development of an integrated lab-on-chip device that would be able to perform functions useful for medical testing and diagnostics. We have shown proof-of-concept functions all relying on the bead-DW interaction, and which can thus be integrated into one bead-handling system. Our demonstration of integrated operations, however, has been limited.

In future work, we would like to integrate the transport, routing, and electrical sensing demonstrated here into one autonomous bioentity-routing demonstration. We envision one scheme, for example, whereby a sandwich assay [FIG. 8-1] is used for target antigen capture and tagging. In either of two approaches, the presence of a target antigen causes the formation of a complex between SPM and NM beads or particles. In one case [FIG. 8-1(a)],

the presence of an antigen causes NM nanoparticles to decorate the surface of a magnetic bead, thereby changing its hydrodynamic radius. In a second case [FIG. 8-1(b)], SPM nanoparticles in the presence of an antigen tag a NM bead, creating an overall magnetic complex that can be manipulated by DWs.

After complex formation, the solution of bead sandwiches would be placed in an inlet well in a PDMS layer on top of the magnetic DW circuit. DWs in the circuit, which would be driven by current rather than field, thus eliminating the need for an external magnet, would capture the complexed beads and subsequently detect and rout the different sandwiches each to their own location via a branched curvilinear network.

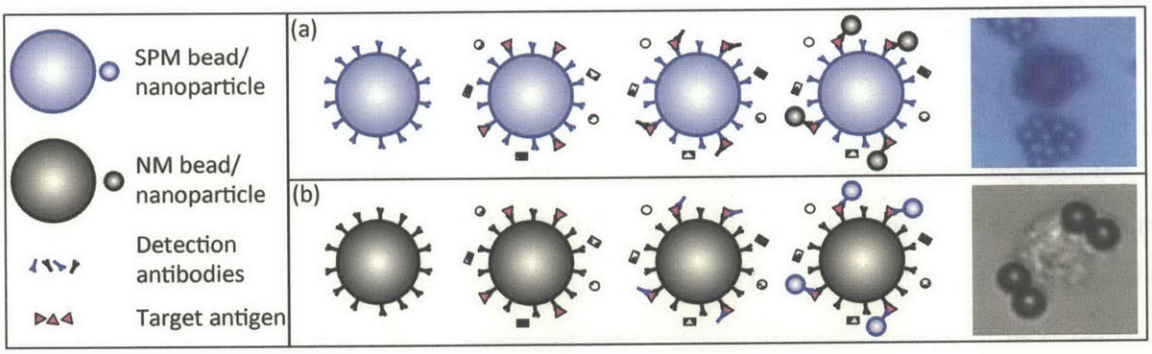

FIG. 8-1 Sandwich assay schemes for antigen capture and tagging

(a-b) Two possible sandwich assay schemes for target antigen capture and tagging. (a) Nonmagnetic nanoparticle tags decorate a superparamagnetic bead. (b) Superparamagnetic nanoparticle tags decorate a nonmagnetic bead. Photo reprinted with permission from Mauk, M. G., Ziober, B. L., Chen, Z., Thompson, J. A. & Bau, H. H. Lab-on-a-chip technologies for oral-based cancer screening and diagnostics: capabilities, issues, and prospects. *Ann. N.Y. Acad. Sci.* **1098,** 467–475 (2007), Copyright 2007, John Wiley and Sons. DOI: 10.1196/annals.1384.025.

8.2.2 Organization of matter

Bead-handling systems are not only useful in the biomedical realm. Recently, there has been substantial work done to investigate bottom-up approaches for the organization of matter. The magnetic bead-handling systems presented here, with its ability to precisely position material on the surface of a chip, could be useful in engineering magnetic and nonmagnetic complexes of arbitrary composition and size. Indeed, magnetic approaches using patterned arrays of magnetic elements or DWs have been used to organize

nonmagnetic and magnetic material. We believe the power of the bead-DW system could be useful in these endeavors.

8.2.3 Tagless transport of nonmagnetic species

Critics of bead-based devices cite the tagging of cells and molecules as cumbersome, not always possible, and a source of cytotoxicity[75] and interference of normal biological processes. Thus, it would be ideal if the advantages of magnetic manipulation could be combined with those of tagless manipulation. We propose that it is possible to use the bead transport by field-driven DW motion infrastructure for the manipulation and transport of nonmagnetic bodies such as cells. There already exist examples[75,84,136] of such "negative magnetophoresis" where nonmagnetic beads or cells immersed in a ferrofluid are manipulated by a field, but they lack the precision and control afforded to magnetic field manipulation of magnetic objects.

Initial calculations (Section 4.2) showed that it is possible to increase the bead-wall binding force by application of a vertical field of polarity matching that of the stray field in the vicinity of the DW [FIG. 4-4]. We also later saw (Section 6.4.1) that application of a vertical field of opposite polarity, however, can reduce the binding force until it is actually negative. That is, in large enough vertical field of polarity opposite that of the DW stray field, the energy contour will begin to invert, resembling a hill more than a well. Where an energy contour is a hill for a magnetic bead in a nonmagnetic medium, it is a well for a nonmagnetic bead in a magnetic medium (given the same difference in susceptibilities). Thus, the application of vertical field can result in a positive binding force between nonmagnetic species and DWs, owing to the fact that a nonmagnetic body in a magnetic medium has an effectively negative susceptibility. Thus, the precision with which magnetic beads can be manipulated should also be achievable with nonmagnetic entities, opening up the possibility for fast and controllable tagless manipulation.

In future work, we hope to demonstrate such precise manipulation of nonmagnetic beads and bioentities by DWs, thereby making null one of the major criticisms of, and simultaneously taking advantage of the power of, bead-based approaches.

Bibliography

1. Zhang, H., Xu, T., Li, C.-W. & Yang, M. A microfluidic device with microbead array for sensitive virus detection and genotyping using quantum dots as fluorescence labels. *Biosens. Bioelectron.* **25,** 2402–2407 (2010).
2. Hertz, H. M. Standing-wave acoustic trap for nonintrusive positioning of microparticles. *J. Appl. Phys.* **78,** 4895–4849 (1995).
3. Tennico, Y. H., Hutanu, D., Koesdjojo, M. T., Bartel, C. M. & Remcho, V. T. On-chip aptamer-based sandwich assay for thrombin detection employing magnetic beads and quantum dots. *Anal. Chem.* **82,** 5591–5597 (2010).
4. Jans, H. *et al.* A simple double-bead sandwich assay for protein detection in serum using UV–vis spectroscopy. *Talanta* **83,** 1580–1585 (2011).
5. Bow, H. *et al.* A microfabricated deformability-based flow cytometer with application to malaria. *Lab Chip* **11,** 1065–1073 (2011).
6. Gossett, D. R. *et al.* Label-free cell separation and sorting in microfluidic systems. *Anal. Bioanal. Chem.* **397,** 3249–3267 (2010).
7. Gascoyne, P. & Vykoukal, J. Particle separation by dielectrophoresis. *Electrophoresis* **23,** 1973–1983 (2002).
8. Pethig, R., Talary, M. S. & Lee, R. S. Enhancing traveling-wave dielectrophoresis with signal superposition. *IEEE Eng. Med. Biol.* **22,** 43–50 (2003).
9. Hilber, W. *et al.* Particle manipulation using 3D ac electro-osmotic micropumps. *J. Micromech. Microeng.* **18,** 064016 (2008).
10. Park, S., Zhang, Y., Wang, T.-H. & Yang, S. Continuous dielectrophoretic bacterial separation and concentration from physiological media of high conductivity. *Lab Chip* **11,** 2893–2900 (2011).
11. Thiel, A., Scheffold, A. & Radbruch, A. Immunomagnetic cell sorting—pushing the limits. *Immunotechnology* **4,** 89–96 (1998).
12. Safarik, I. & Safarikova, M. Use of magnetic techniques for the isolation of cells. *Journal of Chromatography B* **722,** 33–53 (1999).
13. Pankhurst, Q. A., Connolly, J., Jones, S. K. & Dobson, J. Applications of magnetic nanoparticles in biomedicine. *J. Phys. D: Appl. Phys.* **36,** R167–R181 (2003).
14. Gijs, M. A. M. Magnetic bead handling on-chip: new opportunities for analytical

applications. *Microfluid. Nanofluid.* **1,** 22–40 (2004).

15. Pamme, N. Magnetism and microfluidics. *Lab Chip* **6,** 24–38 (2006).
16. Pankhurst, Q. A., Thanh, N. K. T., Jones, S. K. & Dobson, J. Progress in applications of magnetic nanoparticles in biomedicine. *J. Phys. D: Appl. Phys.* **42,** 224001 (2009).
17. Liu, C., Stakenborg, T., Peeters, S. & Lagae, L. Cell manipulation with magnetic particles toward microfluidic cytometry. *J. Appl. Phys.* **105,** 102014 (2009).
18. Gijs, M. A. M., Lacharme, F. & Lehmann, U. Microfluidic applications of magnetic particles for biological analysis and catalysis. *Chem. Rev.* **110,** 1518–1563 (2010).
19. Lee, C. S., Lee, H. & Westervelt, R. M. Microelectromagnets for the control of magnetic nanoparticles. *Appl. Phys. Lett.* **79,** 3308–3310 (2001).
20. Lee, H., Purdon, A. M. & Westervelt, R. M. Manipulation of biological cells using a microelectromagnet matrix. *Appl. Phys. Lett.* **85,** 1063–1065 (2004).
21. Pekas, N., Granger, M., Tondra, M., Popple, A. & Porter, M. D. Magnetic particle diverter in an integrated microfluidic format. *J. Magn. Magn. Mater.* **293,** 584–588 (2005).
22. Ramadan, Q. & Yu, C. Microcoils for transport of magnetic beads. *Appl. Phys. Lett.* **88,** 032501 (2006).
23. Liu, C., Lagae, L., Wirix-Speetjens, R. & Borghs, G. On-chip separation of magnetic particles with different magnetophoretic mobilities. *J. Appl. Phys.* **101,** 024913 (2007).
24. Li, F., Giouroudi, I. & Kosel, J. A biodetection method using magnetic particles and micro traps. *J. Appl. Phys.* **111,** 07B328 (2012).
25. Deng, T., Prentiss, M. & Whitesides, G. M. Fabrication of magnetic microfiltration systems using soft lithography. *Appl. Phys. Lett.* **80,** 461–463 (2002).
26. Gunnarsson, K. *et al.* Programmable motion and separation of single magnetic particles on patterned magnetic surfaces. *Adv. Mater.* **17,** 1730–1734 (2005).
27. Halverson, D. S., Kalghatgi, S., Yellen, B. B. & Friedman, G. Manipulation of nonmagnetic nanobeads in dilute ferrofluid. *J. Appl. Phys.* **99,** 08P504 (2006).
28. Yellen, B. B. *et al.* Traveling wave magnetophoresis for high resolution chip based separations. *Lab Chip* **7,** 1681–1688 (2007).
29. Guo, S. S., Deng, Y. L., Zhao, L. B., Chan, H. L. W. & Zhao, X.-Z. Effect of patterned micro-magnets on superparamagnetic beads in microchannels. *J. Phys. D: Appl. Phys.* **41,** 105008 (2008).

30. Johansson, L. *et al.* A magnetic microchip for controlled transport of attomole levels of proteins. *Lab Chip* **10,** 654–661 (2010).
31. Henighan, T. *et al.* Manipulation of magnetically labeled and unlabeled cells with mobile magnetic traps. *Biophys. J.* **98,** 412–417 (2010).
32. Henighan, T., Giglio, D., Chen, A., Vieira, G. & Sooryakumar, R. Patterned magnetic traps for magnetophoretic assembly and actuation of microrotor pumps. *Appl. Phys. Lett.* **98,** 103505 (2011).
33. Chen, A. & Sooryakumar, R. Patterned time-orbiting potentials for the confinement and assembly of magnetic dipoles. *Sci. Rep.* **3,** 1–5 (2013).
34. Chen, A. *et al.* On-chip magnetic separation and encapsulation of cells in droplets. *Lab Chip* **13,** 1172–1181 (2013).
35. Chen, A., Byvank, T., Vieira, G. B. & Sooryakumar, R. Magnetic microstructures for control of Brownian motion and microparticle transport. *IEEE Trans. Magn.* **49,** 300–308 (2013).
36. Vieira, G. *et al.* Magnetic wire traps and programmable manipulation of biological cells. *Phys. Rev. Lett.* **103,** 128101 (2009).
37. Ruan, G. *et al.* Simultaneous Magnetic Manipulation and Fluorescent Tracking of Multiple Individual Hybrid Nanostructures. *Nano Lett.* **10,** 2220–2224 (2010).
38. Donolato, M. *et al.* On-chip manipulation of protein-coated magnetic beads via domain-wall conduits. *Adv. Mater.* **22,** 2706–2710 (2010).
39. Bryan, M. T. *et al.* Switchable Cell Trapping Using Superparamagnetic Beads. *IEEE Magn. Lett.* **1,** 1500104 (2010).
40. Donolato, M. *et al.* Magnetic domain wall conduits for single cell applications. *Lab Chip* **11,** 2976–2983 (2011).
41. Chen, A. *et al.* Regulating Brownian Fluctuations with Tunable Microscopic Magnetic Traps. *Phys. Rev. Lett.* **107,** 087206 (2011).
42. Vieira, G. *et al.* Transport of magnetic microparticles via tunable stationary magnetic traps in patterned wires. *Phys. Rev. B* **85,** 174440 (2012).
43. Torti, A. *et al.* Single particle demultiplexer based on domain wall conduits. *Appl. Phys. Lett.* **101,** 142405 (2012).
44. Rapoport, E. & Beach, G. S. D. Dynamics of superparamagnetic microbead transport along magnetic nanotracks by magnetic domain walls. *Appl. Phys. Lett.* **100,** 082401

(2012).

45. Rapoport, E. & Beach, G. S. D. Transport dynamics of superparamagnetic microbeads trapped by mobile magnetic domain walls. *Phys. Rev. B* **87,** 174426 (2013).
46. Baselt, D. R. *et al.* A biosensor based on magnetoresistance technology. *Biosens. Bioelectron.* **13,** 731–739 (1998).
47. Tondra, M., Porter, M. & Lipert, R. J. Model for detection of immobilized superparamagnetic nanosphere assay labels using giant magnetoresistive sensors. *J. Vac. Sci. Technol. A* **18,** 1125–1129 (2000).
48. Edelstein, R. *et al.* The BARC biosensor applied to the detection of biological warfare agents. *Biosens. Bioelectron.* **14,** 805–813 (2000).
49. Miller, M. M. *et al.* A DNA array sensor utilizing magnetic microbeads and magnetoelectronic detection. *J. Magn. Magn. Mater.* **225,** 138–144 (2001).
50. Lagae, L. *et al.* On-chip manipulation and magnetization assessment of magnetic bead ensembles by integrated spin-valve sensors. *J. Appl. Phys.* **91,** 7445–7447 (2002).
51. Li, G. *et al.* Detection of single micron-sized magnetic bead and magnetic nanoparticles using spin valve sensors for biological applications. *J. Appl. Phys.* **93,** 7557–7559 (2003).
52. Schotter, J. *et al.* Comparison of a prototype magnetoresistive biosensor to a standard flourescent DNA detection. *Biosens. Bioelectron.* **19,** 1149–1156 (2004).
53. Wang, S. X. *et al.* Towards a magnetic microarray for sensitive diagnostics. *J. Magn. Magn. Mater.* **293,** 731–736 (2005).
54. Li, G. *et al.* Spin valve sensors for ultrasensitive detection of superparamagnetic nanoparticles for biological applications. *Sens. Actuators, A* **126,** 98–106 (2006).
55. Ferreira, H. A., Cardoso, F. A., Ferreira, R., Cardoso, S. & Freitas, P. P. Magnetoresistive DNA chips based on ac field focusing of magnetic labels. *J. Appl. Phys.* **99,** 1–3 (2006).
56. Wang, S. X. & Li, G. Advances in giant magnetoresistance biosensors with magnetic nanoparticle tags: review and outlook. *IEEE Trans. Magn.* **44,** 1687–1702 (2008).
57. Osterfeld, S. J. *et al.* Multiplex protein assays based on real-time magnetic nanotag sensing. *Proc. Natl. Acad. Sci. USA* **105,** 20637–20640 (2008).
58. Martins, V. C. *et al.* Femtomolar limit of detection with a magnetoresistive biochip. *Biosens. Bioelectron.* **24,** 2690–2695 (2009).
59. Martins, V. C. *et al.* Challenges and trends in the development of a magnetoresistive

biochip portable platform. *J. Magn. Magn. Mater.* **322,** 1655–1663 (2010).

60. Gaster, R. S. *et al.* Quantification of protein interactions and solution transport using high-density GMR sensor arrays. *Nat. Nanotechnol.* **6,** 314–320 (2011).
61. Gaster, R. S., Hall, D. A. & Wang, S. X. nanoLAB: an ultraportable, handheld diagnostic laboratory for global health. *Lab Chip* **11,** 950 (2011).
62. Llandro, J. *et al.* Quantitative digital detection of magnetic beads using pseudo-spin-valve rings for multiplexed bioassays. *Appl. Phys. Lett.* **91,** 203904 (2007).
63. Vavassori, P. *et al.* Domain wall displacement in Py square ring for single nanometric magnetic bead detection. *Appl. Phys. Lett.* **93,** 203502 (2008).
64. Donolato, M. *et al.* Nanosized corners for trapping and detecting magnetic nanoparticles. *Nanotechnology* **20,** 385501 (2009).
65. Strömberg, M. *et al.* Multiplex detection of DNA sequences using the volume-amplified magnetic nanobead detection assay. *Anal. Chem.* **81,** 3398–3406 (2009).
66. Donolato, M. *et al.* On-chip measurement of the Brownian relaxation frequency of magnetic beads using magnetic tunneling junctions. *Appl. Phys. Lett.* **98,** 073702 (2011).
67. Dalslet, B. T. *et al.* Bead magnetorelaxometry with an on-chip magnetoresistive sensor. *Lab Chip* **11,** 296–302 (2011).
68. Rapoport, E. & Beach, G. S. D. Magneto-mechanical resonance of a single superparamagnetic microbead trapped by a magnetic domain wall. *J. Appl. Phys.* **111,** 07B310 (2012).
69. Rapoport, E., Montana, D. & Beach, G. S. D. Integrated capture, transport, and magneto-mechanical resonant sensing of superparamagnetic microbeads using magnetic domain walls. *Lab Chip* **12,** 4433–4440 (2012).
70. Nam, J. M., Thaxton, C. S. & Mirkin, C. A. Nanoparticle-based bio-bar codes for the ultrasensitive detection of proteins. *Science* **301,** 1884–1886 (2003).
71. Pamme, N. & Wilhelm, C. Continuous sorting of magnetic cells via on-chip free-flow magnetophoresis. *Lab Chip* **6,** 974–980 (2006).
72. Derks, R. J. S., Dietzel, A., Wimberger-Friedl, R. & Prins, M. W. J. Magnetic bead manipulation in a sub-microliter fluid volume applicable for biosensing. *Microfluid. Nanofluid.* **3,** 141–149 (2007).
73. Sista, R. S. *et al.* Heterogeneous immunoassays using magnetic beads on a digital microfluidic platform. *Lab Chip* **8,** 2188 (2008).

74. Adams, J. D., Kim, U. & Soh, H. T. Multitarget magnetic activated cell sorter. *Proc. Natl. Acad. Sci. USA* **105,** 18165–18170 (2008).

75. Krebs, M. D. *et al.* Formation of ordered cellular structures in suspension via label-free negative magnetophoresis. *Nano Lett.* **9,** 1812–1817 (2009).

76. Issadore, D. *et al.* Self-assembled magnetic filter for highly efficient immunomagnetic separation. *Lab Chip* **11,** 147–151 (2011).

77. Kirby, D. *et al.* Centrifugo-magnetophoretic particle separation. *Microfluid. Nanofluid.* **13,** 899–908 (2012).

78. Castro, C. M. *et al.* Miniaturized nuclear magnetic resonance platform for detection and profiling of circulating tumor cells. *Lab Chip* **14,** 14–23 (2014).

79. Frey, N. A., Peng, S., Cheng, K. & Sun, S. Magnetic nanoparticles: synthesis, functionalization, and applications in bioimaging and magnetic energy storage. *Chem. Soc. Rev.* **38,** 2532–2542 (2009).

80. Shapiro, H. M. & Leif, R. C. *Practical flow cytometry.* (John Wiley & Sons, 2003).

81. Bryan, M. T. *et al.* The effect of trapping superparamagnetic beads on domain wall motion. *Appl. Phys. Lett.* **96,** 192503 (2010).

82. Chen, C.-T. & Chen, Y.-C. Functional magnetic nanoparticle-based label free fluorescence detection of phosphorylated species. *Chem. Commun.* **46,** 5674–5676 (2010).

83. Donolato, M., Dalslet, B. T. & Hansen, M. F. Microstripes for transport and separation of magnetic particles. *Biomicrofluidics* **6,** 024110 (2012).

84. Yellen, B. B., Hovorka, O. & Friedman, G. Arranging matter by magnetic nanoparticle assemblers. *Proc. Natl. Acad. Sci. USA* **102,** 8860–8864 (2005).

85. Yellen, B. B., Erb, R. M., Halverson, D. S., Hovorka, O. & Friedman, G. Arraying Nonmagnetic Colloids by Magnetic Nanoparticle Assemblers. *IEEE Trans. Magn.* **42,** 3548–3553 (2006).

86. Baibich, M. N., Broto, J. M., Fert, A., Nguyen Van Dau, F. & Petroff, F. Giant magnetoresistance of (001)Fe/(001)Cr magnetic superlattices. *Phys. Rev. Lett.* **61,** 2472–2475 (1988).

87. Binasch, G., Grunberg, P., Saurenbach, F. & Zinn, W. Enhanced magnetoresistance in layered magnetic structures with antiferromagnetic interlayer exchange. *Phys. Rev. B* **39,** 4828–4830 (1989).

88. Barnas, J., Fuss, A., Camley, R. E., Grunberg, P. & Zinn, W. Novel magnetoresistance effect in layered magnetic structures: Theory and experiment. *Phys. Rev. B* **42,** 8110–8120 (1990).

89. Dieny, B. *et al.* Giant magnetoresistance in soft ferromagnetic multilayers. *Phys. Rev. B* **43,** 1297–1300 (1991).

90. Dieny, B. *et al.* Magnetotransport properties of magnetically soft spinvalve structures. *J. Appl. Phys.* **69,** 4774–4776 (1991).

91. Tsymbal, E. Y. & Pettifor, D. G. *Solid state physics: perspectives of giant magnetoresistance.* **56,** 113–237 (Academic Press, 2001).

92. Takahashi, Y. K. *et al.* Large magnetoresistance in current-perpendicular-to-plane pseudospin valve using a Co 2 Fe (Ge 0.5 Ga 0.5) Heusler alloy. *Appl. Phys. Lett.* **98,** 152501 (2011).

93. Mitrelias, T. *et al.* Enabling suspension-based biochemical assays with digital magnetic microtags. *J. Appl. Phys.* **107,** 09B319 (2010).

94. Freitas, P. P. *et al.* Spintronic platforms for biomedical applications. *Lab Chip* **12,** 546–557 (2012).

95. Kotitz, R., Weitschies, W., Trahms, L., Brewer, W. & Semmler, W. Determination of the binding reaction between avidin and biotin by relaxation measurements of magnetic nanoparticles. *J. Magn. Magn. Mater.* **194,** 62–68 (1999).

96. Connolly, J. & St Pierre, T. G. Proposed biosensors based on time-dependent properties of magnetic fluids. *J. Magn. Magn. Mater.* **225,** 156–160 (2001).

97. Astalan, A. P., Ahrentorp, F., Johansson, C., Larsson, K. & Krozer, A. Biomolecular reactions studied using changes in Brownian rotation dynamics of magnetic particles. *Biosens. Bioelectron.* **19,** 945–951 (2004).

98. Hong, C.-Y. *et al.* Wash-free immunomagnetic detection for serum through magnetic susceptibility reduction. *Appl. Phys. Lett.* **90,** 074105 (2007).

99. Redjdal, M., Giusti, J. H., Ruane, M. F. & Humphrey, F. B. Structure dependent stray fields from domain walls in permalloy films. *IEEE Trans. Magn.* **39,** 2684–2686 (2003).

100. Donolato, M. *et al.* Characterization of domain wall–based traps for magnetic beads separation. *J. Appl. Phys.* **111,** 07B336 (2012).

101. Ono, T. *et al.* Propagation of a magnetic domain wall in a submicrometer magnetic wire. *Science* **284,** 468–470 (1999).

102. Allwood, D. A. *et al.* Shifted hysteresis loops from magnetic nanowires. *Appl. Phys. Lett.* **81,** 4005–4007 (2002).

103. Cowburn, R. P., Allwood, D. A., Xiong, G. & Cooke, M. D. Domain wall injection and propagation in planar Permalloy nanowires. *J. Appl. Phys.* **91,** 6949–6951 (2002).

104. Atkinson, D. *et al.* Magnetic domain-wall dynamics in a submicrometre ferromagnetic structure. *Nat. Mater.* **2,** 85–87 (2003).

105. Faulkner, C. C. *et al.* Artificial domain wall nanotraps in Ni81Fe19 wires. *J. Appl. Phys.* **95,** 6717–6719 (2004).

106. Allwood, D. A. *et al.* Magnetic domain-wall logic. *Science* **309,** 1688–1692 (2005).

107. Beach, G. S. D., Nistor, C., Knutson, C., Tsoi, M. & Erskine, J. L. Dynamics of field-driven domain-wall propagation in ferromagnetic nanowires. *Nat. Mater.* **4,** 741–744 (2005).

108. Vieira, G. Patterned magnetic structures for micro-/nanoparticle and cell manipulation. 1–131 (2012).

109. O'Handley, R. C. *Modern magnetic materials: principles and applications.* (John Wiley & Sons, Inc., 2000).

110. Abo, G. S. *et al.* Definition of magnetic exchange length. *IEEE Trans. Magn.* **49,** 4937–4939 (2013).

111. Allwood, D. A. *et al.* Submicrometer Ferromagnetic NOT Gate and Shift Register. *Science* **296,** 2003–2006 (2002).

112. Parkin, S. S. P., Hayashi, M. & Thomas, L. Magnetic domain-wall racetrack memory. *Science* **320,** 190–194 (2008).

113. Beach, G. S. D., Tsoi, M. & Erskine, J. L. Current-induced domain wall motion. *J. Magn. Magn. Mater.* **320,** 1272–1281 (2008).

114. McMichael, R. D. & Donahue, M. J. Head to head domain wall structures in thin magnetic strips. *IEEE Trans. Magn.* **33,** 4167–4169 (1997).

115. Nakatani, Y., Thiaville, A. & Miltat, J. Head-to-head domain walls in soft nano-strips: a refined phase diagram. *J. Magn. Magn. Mater.* **290-291,** 750–753 (2005).

116. Negoita, M., Hayward, T. J. & Allwood, D. A. Controlling domain walls velocities in ferromagnetic ring-shaped nanowires. *Appl. Phys. Lett.* **100,** 072405 (2012).

117. Negoita, M., Hayward, T. J., Miller, J. A. & Allwood, D. A. Domain walls in ring-shaped nanowires under rotating applied fields. *J. Appl. Phys.* **114,** 013904 (2013).

118. Happel, J. & Brenner, H. *Low Reynolds number hydrodynamics: with special applications to particulate media.* (Martinus Nijhoff Publishers, 1983).

119. Jones, T. B. *Electromechanics of Particles.* (Cambridge University Press, 1995).

120. Donahue, M. J. & Porter, D. G. *OOMMF User's Guide Version 1.0.* (NIST, Gaithersburg, MD, 1999).

121. Qiu, Z. Q. & Bader, S. D. Surface magneto-optic Kerr effect. *Rev. Sci. Instrum.* **71,** 1243–1255 (2000).

122. Allwood, D. A., Xiong, G., Cooke, M. D. & Cowburn, R. P. Magneto-optical Kerr effect analysis of magnetic nanostructures. *J. Phys. D: Appl. Phys.* **36,** 2175–2182 (2003).

123. Polisetty, S. *et al.* Optimization of magneto-optical Kerr setup: analyzing experimental assemblies using Jones matrix formalism. *Rev. Sci. Instrum.* **79,** 055107 (2008).

124. Cowburn, R. P., Koltsov, D. K., Adeyeye, A. O. & Welland, M. E. Probing submicron nanomagnets by magneto-optics. *Appl. Phys. Lett.* **73,** 3947–3949 (1998).

125. Rothman, J. *et al.* Observation of a bi-domain state and nucleation free switching in mesoscopic ring magnets. *Phys. Rev. Lett.* **86,** 1098–1101 (2001).

126. Castaño, F. J. *et al.* Metastable states in magnetic nanorings. *Phys. Rev. B* **67,** 184425 (2003).

127. Park, M. H. *et al.* Vortex head-to-head domain walls and their formation in onion-state ring elements. *Phys. Rev. B* **73,** 094424 (2006).

128. Ross, C. A. *et al.* Magnetism in multilayer thin film rings. *J. Phys. D: Appl. Phys.* **41,** 113002 (2008).

129. Laufenberg, M. *et al.* Domain wall spin structures in 3d metal ferromagnetic nanostructures. *Adv. in Sold State Phys.* **46,** 281–293 (2008).

130. Jung, H. S., Doyle, W. D. & Matsunuma, S. Influence of underlayers on the soft properties of high magnetization FeCo films. *J. Appl. Phys.* **93,** 6462–6464 (2003).

131. Murthy, V. S. N., Krishnamoorthi, C., Mahendiran, R. & Adeyeye, A. O. Magnetization reversal and interlayer coupling in Co50Fe50 nanomagnets. *J. Appl. Phys.* **105,** 023916 (2009).

132. Schrefl, T., Fidler, J., Kirk, K. J. & Chapman, J. N. Domain structures and switching mechanisms in patterned magnetic elements. *J. Magn. Magn. Mater.* **175,** 193–204 (1997).

133. Kirk, K. J., Chapman, J. N. & Wilkinson, C. D. W. Switching fields and magnerostatic

interactions of thin film magnetic nanoelements. *Appl. Phys. Lett.* **71,** 539–541 (1997).

134. Kirk, K. J., Chapman, J. N. & Wilkinson, C. D. W. Lorentz microscopy of small magnetic structures. *J. Appl. Phys.* **85,** 5237–5241 (2010).
135. Strömberg, M. *et al.* Sensitive Molecular Diagnostics Using Volume-Amplified Magnetic Nanobeads. *Nano Lett.* **8,** 816–821 (2008).
136. Erb, R. M., Son, H. S., Samanta, B., Rotello, V. M. & Yellen, B. B. Magnetic assembly of colloidal superstructures with multipole symmetry. *Nature* **457,** 999–1002 (2009).
137. We gratefully acknowledge the computational resources of A. Alexander-Katz and the assistance of C. E. Sing.
138. We gratefully acknowledge the design and construction of the quadrature rotation box by D. Bono.
139. We have calculated the binding energy under application of an in-plane magnetic field transverse to the track and find no significant change, due to the predominantly out-of-plane gradient of the DW stray field.